GRAPHENE DEVICES FOR SENSING AND ELECTRICAL CONTROL OF MAGNETIC PHENOMENA

A Dissertation

Presented to the Faculty of the Graduate School

of Cornell University

in Partial Fulfillment of the Requirements for the Degree of

Doctor of Philosophy

by

Brian Thomas Schaefer

May 2021

GRAPHENE DEVICES FOR SENSING AND ELECTRICAL CONTROL OF MAGNETIC PHENOMENA

Brian Thomas Schaefer, Ph.D.

Cornell University 2021

Graphene is a material consisting of a single layer of carbon atoms, with distinctive electronic characteristics that make it an interesting platform for a variety of applications. In this dissertation, I discuss projects applying graphene towards experiments involving scanning magnetometry, a technique to image stray magnetic fields above the surface of a material or device. First, I provide an overview of scanning magnetometry techniques and detailed fabrication procedures for high-quality graphene devices. Then, I evaluate ultraclean graphene as a material for highly sensitive Hall-effect sensors. These devices are promising for the development of a scanning Hall probe microscope operational over a range of temperatures and magnetic fields not previously accessible with a single sensor. I then discuss calculations predicting an orbital magnetoelectric effect in strained bilayer graphene. This effect is electrically tunable, switchable, and arises from orbital degrees of freedom. Finally, I present progress towards experimentally realizing strained bilayer graphene devices and propose studying the effect using scanning magnetometry.

BIOGRAPHICAL SKETCH

Brian Schaefer was born in Jacksonville, Florida in 1993 and graduated from Allen D. Nease Senior High School in 2010. He attended the the University of Florida from 2010–2014 and graduated with Bachelor of Science degrees in Physics and Materials Science & Engineering. In 2014, he entered the graduate program in Physics at Cornell University and joined Katja Nowack's research group as a founding member in Spring 2015.

During his time in Ithaca, Brian maintained an active role in the Physics Graduate Society and organized the department's annual music concert. He advocated for science literacy broadly to the local community as an outreach facilitator and student ambassador for the Cornell Center for Materials Research (CCMR) and Cornell Nanoscale Facility. He also engaged with educators, leading the Physics Department's teaching assistant training program and presenting at workshops for high school science teachers.

Before the COVID-19 pandemic, Brian enjoyed spending time in Ithaca playing clarinets of many sizes with the Cornell Orchestras, meeting up with a fantastic group of friends for board games, and spending long summer days cycling around (sometimes literally *around*) the Finger Lakes.

ACKNOWLEDGEMENTS

Upon reflecting on the past seven (plus) years, a journey starting with the decision to pursue a PhD in physics, I came to realize the true volume of people that have supported me along the way. It will be impossible to list everyone here, but I'll try my best.

First and foremost, I thank Katja Nowack for her irreplaceable mentorship, often undeserved level of attention, and unwavering support. It was an honor to help build your lab, and I am excited to see what the future brings for you!

It of course didn't take just two to build the Nowack lab, and so I acknowledge the hard work of the rest of the team, including Kevin, Jihoon, David, Matt, Alex, Nicole, Justin, Rachel, and Kristen. It has been a pleasure working with all of you, and I admire your devotion towards science.

My committee members, Erich Mueller and Paul McEuen, helped motivate the toughest projects I undertook during my PhD and offered such amazing clarity that set me loose in unexpected directions. Thank you for your expertise, guidance, and for deepening my knowledge of solid-state physics.

I never anticipated how much I would interact with so many other esteemed professors that valued my scholarship, both at Cornell and UF. Professors Ramshaw, Ralph, Fuchs, Rana, Buhrman, Muller, Mak, Shan, Parpia, Jena, Xing, Biswas, and Jones: thank you for discussions that broadened my appreciation for physical science.

Guen Prawiroatmodjo inspired me to become a rigorous programmer and helped get the lab's software up and running. Lei Wang, David MacNeill, Marcos Guimarães, and Menyoung Lee were the wizards of graphene fabrication who taught me their spells. The incomparable Eric Smith made my low-temperature experiments possible. The McEuen, Fuchs, Ralph, and Parpia

groups shared stories, tips, lab equipment, and were awesome basement neighbors and cleanroom buddies.

I owe my debts to everyone who kept the gears turning (sometimes literally) and allowed me to focus my attention towards my research. To the CNF/CCMR staff (Mike, Chris, Amrita, Alan, Jeremy, Vince, John, Tom, Steve, Phil, etc.), department staff (Deb, Kacey, Danyel, Craig, Douglas, Lea, etc.), and facilities support staff (Jason, Nathan, Rob, and the LASSP machinists): thank you for helping me over all sorts of hurdles.

I will surely miss outreach with CNF and CCMR, and I have developed new admiration and respect for science educators because of these experiences. Beth, Mark, and Nev: thank you for spearheading fantastic outreach programs.

Richard MacDowell, Chris Kim, James Spinazzola, Miri Yampolsky, Sergio Ospina-Romero, and hundreds of student musicians in the Cornell Symphony Orchestra and Cornell Wind Symphony: thank you for sharing your music. Scotty, Josh, Michael, Daniel, Robbie, Matt, Sean, Ian, and Brandon: thank you for staying connected over literal decades. Yi Xue, Alex G., Rahul, Meera, Gowri, Kevin, Jihoon, William, and Albert: let me know if you ever find the ultimate twice-cooked pork (I'll settle for crispy tofy with carlic sauce). Morgan, Alex M., James, Béline, Ryan P., Paula, Alex P., Peter, Juli, Andrés, and a smattering of plant pathologists: thanks for games, friendship, and for providing an outlet for my competitiveness. Kyle, Jason, Jocienne, Ryan T., Isaiah, Nils, and Vaibhav: thanks for being awesome housemates.

To my family, this degree probably seemed like it took longer for you than it did for me, so thank you for your patience and support over the years.

And finally, I give Caitlyn all my gratitude for her unceasing love and encouragement, and for being the ultimate pandemic lockdown partner.

TABLE OF CONTENTS

LIST OF TABLES

LIST OF FIGURES

CHAPTER 1

INTRODUCTION

Throughout my PhD, I developed perspectives on condensed-matter physics from multiple viewpoints. The first viewpoint is one established before Cornell, arising from a degree in Materials Science & Engineering and undergraduate research on oxide materials. I first approached condensed-matter physics research with the desire to explore the periodic table and understand physical properties arising from interesting combinations of chemical elements.

I obtained a second viewpoint during the start of my research career at Cornell; I joined the Nowack group as a founding member in 2015 and undertook a leading role in building a cryogenic scanning magnetometry laboratory from the ground up. This caused my interests to shift from understanding a breadth of materials to understanding the depth of a single—but unique and powerful—experimental technique.

In parallel with the second, I developed a third viewpoint centered around a singular material consisting of a single atomic sheet of carbon: graphene. I began to understand that complex materials are not always necessary to realize rich electronic properties; there is beauty in graphene's simplicity. This perspective lent conflicting ideas: I often remained skeptical towards the unceasing labeling of graphene as a "wonder material," but at the same time I was excited by each new advance in graphene technology. This helped to inform the guiding questions for my experimental work on graphene. What makes graphene unique? Which unique characteristics are really important? Is it really *better* than other material systems? Do we need to fabricate the absolute best-performing graphene devices to have an impact on modern electronics?

The final viewpoint aims to connect the tools at my disposal with the leading edge of condensed-matter physics research. I took inspiration from exciting new experimental observations of unexpected physical phenomena and asked: "Given my experimental toolkit, how could I study the same phenomenon to obtain results that are complementary, more convincing, or even disprove the original report?" This helped me maintain enthusiasm for both my primary technique, scanning magnetometry, and my primary material of interest, graphene. I envisioned merging the two to study such phenomena as the fractional quantum Hall effect, hydrodynamic electron flow, and unconventional superconductivity in graphene-based devices.

Through these viewpoints, I came to understand my contributions to the scientific community. Fueled by a combination of passion, practicality, curiosity, and ambition, the work described in this dissertation is a snapshot view of my share of work towards our collective understanding of the physical world. I hope the reader finds the content interesting, useful, and enjoyable.

1.1 Outline

This dissertation mainly follows the timeline of my residence at Cornell. My first experimental undertaking was to build a cryogenic scanning superconducting quantum interference device (SQUID) microscope. Therefore in Chapter 2, I review the principles behind scanning magnetometry, with emphasis on SQUIDs as well as Hall-effect sensors. I take a deeper dive into explaining sources of noise in these sensors, fabrication procedures to enable scanning measurements with planar sensors, and considerations for interpreting the obtained

magnetic field images.

In Chapter 3, I describe at length fabrication processes for high-quality graphene devices. The success of this process hinges on a few crucial details, and I hope that the instructions in this chapter will help facilitate the development of similar techniques in the future.

Chapter 4 is an intersection of concepts introduced in Chapters 2 and 3; I describe the fabrication and characterization of ultraclean graphene Hall sensors that hold great promise for use as versatile scanning probe magnetometers. In my thorough analysis of these sensors, I develop an important perspective on fabricating practical sensors from one of the cleanest possible electronic systems at present. By performing a thorough noise characterization of the sensors over a variety of experimental conditions, I demonstrate that the high electronic quality of these devices leads to a performance meeting or exceeding that of the best reported Hall sensors made from a variety of other materials.

Chapters 5 and 6 approach a new magnetic effect in strained bilayer graphene from theoretical and experimental perspectives, respectively, and are presented out of chronological order. In Chapter 5, I develop a computational model for strained bilayer graphene, focusing on properties arising from the orbital magnetic moment of the low-energy electronic states. My model predicts that strained bilayer graphene devices can develop an electrically tunable and switchable magnetization, offering interesting insight into the valley degree of freedom in graphene. In Chapter 6, I discuss experimental progress towards realizing such devices. I approached this project with considerations towards an experimental geometry compatible with scanning probe microscopy, which can potentially be used to detect the predicted magnetization.

CHAPTER 2

MAGNETIC FIELD SENSORS FOR SCANNING PROBE MICROSCOPY

Magnetic moments and moving charges in condensed-matter systems produce magnetic fields. Imaging the stray magnetic fields above the surface of materials or devices on a local scale can be useful towards understanding the microscopic physical properties of these systems. These magnetic fields can have diverse origins, including conventional magnetic order (i.e., ferromagnetism), the magnetic response of superconductors, and electric current flow. Not only are local imaging techniques instructive, revealing the local structure of a sample, but they are also sometimes necessary, because the magnitude of the magnetic response of small-volume samples can become too small for conventional bulk measurements.

For example, scanning magnetometry can provide several insights for bulk superconductors. Imaging Meissner screening and trapped flux vortices in these materials combined with measuring the magnetic response to a locally applied magnetic field provides insight into the spatial variation of superfluid density, vortex dynamics, and quantum fluctuations in both conventional and unconventional superconductors [1–8]. Scanning magnetometry can also reveal unusual spin textures in magnetic materials, as demonstrated recently in experiments measuring magnetic order and skyrmion dynamics in thin-film magnetic systems [9–11]. Moreover, scanning magnetic probes have been used to directly probe unconventional magnetism in new material systems including magnetic topological insulators and graphene-based moiré superlattices [12, 13].

A thorough review of magnetic imaging experiments is beyond the scope of this Chapter, but in the following I will mention a few experiments that I

personally found interesting and exciting. The common thread linking these experiments is complementary measurement of magnetic fields alongside electrical transport, revealing new understanding of underlying physical phenomena. For instance, simultaneously measuring the transport resistance and the magnetic fields originating from edge currents in the quantum Hall and quantum spin Hall regimes addresses the long-standing theoretical model of quantized conductance in systems including graphene at high magnetic field and HgTe quantum wells [14, 15]. Often the magnetic images clarify prior experiments; in Ref. [16], the authors comment on twist angle disorder in a twisted bilayer graphene device, explaining the possible variance in transport properties within a device studied previously. In another study from the Nowack lab at Cornell, imaging the spatial dependence of the superconducting transition of a microstructured heavy-fermion superconductor reveals an effect related to the strain in the crystal [17]. This experiment helped explain transport experiments that by themselves suggested a new exotic form of superconductivity. Finally, recent studies of non-ohmic current distributions in graphene devices support transport measurements suggesting strong electron-electron interactions that lead to hydrodynamic behavior of the electron fluid [18, 19].

In this Chapter, I focus on scanning probes based on solid-state magnetic field sensors compatible with microscopes built in cryogen-free refrigerators, specifically scanning superconducting quantum interference device (SQUID) magnetometers and Hall-effect sensors. These sensors are at this point well-established and provide an electrically tunable response to magnetic fields that can be linearized and calibrated precisely. I will briefly mention other types of sensors useful for scanning magnetometry. Magnetoresistive sensors are less common form of solid-state sensor, but have been previously used in scan-

ning microscopy. The main limitations of magnetoresistive sensors are lack of tunability and reduced sensitivity even at moderate magnetic fields [20–22]. Optically-addressed nitrogen-vacancy centers in diamond provide an imaging technique with fine spatial resolution, high dynamic frequency range, and potential operation over a wide range of temperatures [23]. Recent development of a "scanning quantum cryogenic atom microscope" based on a Bose-Einstein condensate offers an interesting approach to image magnetic fields with high sensitivity [24].

In the remainder of this chapter, I introduce SQUIDs (Section 2.1) and Hall sensors (Section 2.2), discussing noise sources that affect the magnetic field detection limit (Section 2.3). Then, I explain specific design considerations for scanning probes and present details of fabrication processes that enable scanning (Section 2.4). Finally, I discuss the spatial dependence of different sources of magnetic field and the interpretation of magnetic images (Section 2.5).

2.1 SQUID magnetometers

Superconducting **QU**antum **I**nterference **D**evice (SQUID) magnetometers [25–27] (Figure 2.1(a)) consist of a superconducting loop interrupted by two Josephson junctions, most commonly consisting of oxide tunnel barriers or superconducting weak links. Voltage-biasing the device leads to a sinusoidal dependence between the current through the device and the magnetic flux threading the loop (Figure 2.1(b)), with a period equal to the magnetic flux quantum $\Phi_0 \equiv h/(2e) = 2 \times 10^{-15}\,\mathrm{T\,m^2}$, where h is Planck's constant and e is the electron charge.

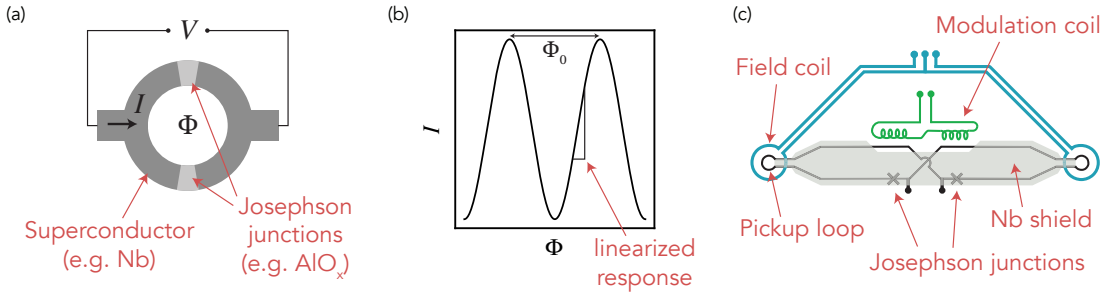

Figure 2.1: (a) Basic structure of a dc SQUID with oxide tunnel junctions. (b) Example current-flux characteristic for a SQUID, biased such that the current is close to the critical current of the junctions. (c) Gradiometric scanning SQUID design, adapted from Ref. [25].

I worked with planar scanning SQUID magnetometers based on the gradiometric design illustrated schematically in Figure 2.1(c), in which the SQUID loop consists of a pair of counterwound pickup loops, one of which can be approached to locally image a sample [25]. The gradiometric design reduces coupling of uniform background magnetic fields into the SQUID. Niobium shielding covers most of the drawn-out pickup loop to provide shielding from stray magnetic flux during scanning measurements, such that the response is due mainly to the flux through the sample-side pickup loop. A field coil concentric with the pickup loop can be used to apply a local magnetic field and measure the local magnetic susceptibility. The design also features an inductively-coupled modulation coil to flux-bias the SQUID, enabling operation in a flux-locked loop that linearizes the response.

Optical lithography limits the minimum pickup loop size in the design described above, leading to a spatial resolution on the order of hundreds of nanometers [27]. Moreover, the effective shape (described by the point spread function, see Section 2.5) of smaller pickup loops is quite distorted compared to the nearly circular shape of larger pickup loops [27, 28]. The desire to im-

age magnetic fields with a finer spatial resolution therefore suggests development of SQUIDs with nanoscale loop diameter (nanoSQUIDs) via electron-beam lithography, focused ion beam sculpting, or specialized material deposition techniques [29]. Notably, SQUID-on-tip devices fabricated via deposition of superconducting materials onto sharp quartz tips have recently demonstrated magnetometry and thermal imaging with pickup loops with effective diameter typically on the 50-100 nm scale [30, 31]. These devices typically have similar noise performance compared to planar SQUIDs, but they lack integrated modulation and field coils.

Though SQUIDs provide perhaps the highest-sensitivity calibrated technique to quantitatively measure small magnetic fields (see Section 2.3), they can only operate in a severely restricted parameter space. The superconducting material in SQUIDs (e.g. Nb) must remain in a superconducting state for the device to be sensitive to magnetic field, requiring operation at low temperature and low background magnetic field (typically up to tens of millitesla for planar SQUIDs). For example, in Nb-based SQUIDs, the superconducting critical temperature of bulk Nb is approximately 9.2 K, but the critical current of the Josephson junctions decreases approaching that temperature, suggesting operation at a fixed low temperature below $\lesssim$ 5 K. While SQUIDs fabricated from high-temperature superconductors have been demonstrated, these sensors suffer from reduced spatial and magnetic field resolution [32, 33]. Alternatively, measurement systems with the sample mounted on a thermally isolated heating stage can enable imaging experiments with the sample at elevated temperature (up to ~100-150 K) relative to the SQUID [34,35]. As I discuss in the next section, and at greater length in Chapter 4, Hall sensors do not have these limitations.

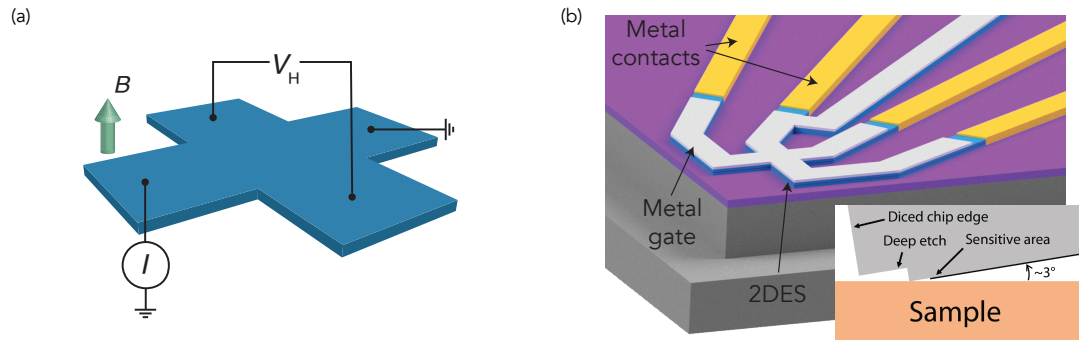

Figure 2.2: (a) Basic measurement configuration for a Hall-effect sensor, with bias current I, Hall voltage V_H, and magnetic field B. (b) Schematic of a generic scanning Hall probe device structure and scanning configuration (inset).

2.2 Hall-effect sensors

Hall-effect sensors are attractive for a variety of magnetic field sensing applications ranging from position detection in robotics [21,36] and tracking nanoparticles in biological systems [37] to fundamental studies of magnetism [38] and superconductivity [39–41]. In an ideal Hall-effect sensor, the sensitive area consists of a two-dimensional electron system (2DES) patterned into a cross shape and biased with electric current I, as in Figure 2.2(a). The deflection of this current in a uniform out-of-plane magnetic field B produces a transverse (Hall) voltage response

$$V_H = \frac{BI}{ne} = IR_H B,$$

where I is the bias current, n is the two-dimensional charge carrier density, e is the electron charge, and $R_H = 1/(ne)$ is the Hall coefficient [36, 42]. In ballistic Hall sensors, $V_H \propto \langle B \rangle$, the average magnetic field within the Hall cross area* [43]. Ballistic Hall sensors are therefore essentially sensitive the magnetic flux through the sensitive area, similar to SQUIDs.

*I continue below under the assumption $B \equiv \langle B \rangle$.

Applying a voltage to an integrated gate controls the carrier density and therefore the voltage response (see Figure 2.2(b) and Chapter 4) [44–46]. Nonlinearities, carrier density inhomogeneity, and other deviations from ideal performance suggest defining the Hall coefficient more generally as

$$R_{\mathrm{H}} = \frac{1}{I}\frac{\partial V_{\mathrm{H}}}{\partial B}.$$

For a small change in magnetic field δB, the Hall resistance $\delta V_{\mathrm{H}}/I$ changes proportionally with R_{H} as the scaling factor.

Hall sensors provide an accessible means of performing noninvasive measurements of magnetic fields. Their operating principle suggests sensitivity over a broad range of temperatures and magnetic fields, unlike SQUIDs and magnetoresistive sensors. Hall sensors with a micrometer-scale sensitive area are well-suited for probing mesoscopic magnetic and superconducting structures and devices, with the sensor interfaced directly with the structure [38,39,41] or integrated into a scanning probe microscope (Figure 2.2(b)) [27,40,46–50].

The performance of a Hall sensor is most commonly evaluated considering both the size and noise properties of the device (see Section 4.6): the device should be small to enable fine spatial resolution and should exhibit low intrinsic noise to enable fine magnetic field resolution. The spatial resolution depends on the type of magnetic field source as well as the geometry of the sensor and scan height, as I will discuss in Section 2.5. Estimating the noise floor of Hall sensors involves measuring the Hall voltage noise spectral density $S_V^{1/2}$ and converting to the magnetic field detection limit $S_B^{1/2}$ using the Hall coefficient:

$$S_B^{1/2} = \frac{S_V^{1/2}}{IR_{\mathrm{H}}}.$$

As discussed in the next section, commonly the noise in Hall sensors is smallest in devices with lower overall resistance. The desire to minimize the noise and

maximize the Hall coefficient suggests that an ideal material system for Hall sensors combines low carrier density and high carrier mobility [44,46]. Suitable platforms for Hall sensors therefore involve high-mobility two-dimensional electron systems, including graphene and III-V semiconductor-based quantum well heterostructures.

2.3 Noise sources for magnetic field sensors

In evaluating the performance of magnetic field sensors, it is important to estimate the magnetic field detection limit and the possible limiting contributions to the noise. Substantial random telegraph and flicker ($1/f$) noise contributions at low frequency motivate the operation of SQUIDs and Hall sensors at kHz frequencies, at which white Johnson and instrumentation noise set a lower bound for the magnetic field detection limit. In the following sections, I describe each of these noise sources, provide a concrete example of evaluating the combined noise in Hall sensors, and where appropriate compare the expected minimum detection limits for SQUIDs and Hall sensors.

2.3.1 White noise

In both SQUIDs and Hall sensors, the expected white noise floor arises mainly from Johnson noise with voltage noise spectral density $S_V^{1/2} = \sqrt{4k_B TR}$. Here, the impedance R in SQUIDs depends on the designed inductance and shunt resistance, which is chosen to avoid hysteretic behavior and is generally independent of pickup loop size [27]. In turn, SQUIDs with similar designs but

different sizes exhibit similar flux noise spectral density $S_\Phi^{1/2}$, but a magnetic field detection limit $S_B^{1/2} \propto d^{-2}$ that increases for smaller pickup loop diameter d. In Hall sensors, R is directly the longitudinal resistance of the conductor itself and the Johnson noise does not depend explicitly on sensor size. This implies an expected scaling of the detection limit $S_B^{1/2} \propto w^{-1}$ with Hall cross width w [39,51].

However, the white noise in Hall sensors is often dominated by the input noise of preamplifiers or other electronics used in the measurement rather than the Johnson noise. Hall sensor measurements typically involve boosting the signal strength with a low-noise preamplifier, typically imposing a white noise floor of 5-10 $\mathrm{nV\,Hz^{-1/2}}$ and motivating the application of a large bias current to increase the voltage signal (see Section 4.3.2). Modern SQUID measurement systems commonly avoid the limitation from instrumentation noise with cryogenic amplification from a SQUID array amplifier, a network of N SQUIDs connected in series that couples inductively to the input SQUID and amplifies the signal by a factor of N [25]. Implementation of a similar system for Hall sensors can potentially improve the effective noise floor of Hall sensor measurements.

The typical detection limit noise floor for SQUIDs is currently superior to that of similarly-sized Hall sensors. A typical white flux noise spectral density for planar Nb-based SQUIDs at kHz frequencies is $S_\Phi^{1/2}$ ~0.1-1 $\mu\Phi_0\,\mathrm{Hz^{-1/2}}$ independent of pickup loop diameter [25,27]. The corresponding magnetic field detection limit is $S_B^{1/2} \sim 4 - 40\,\mathrm{nT\,Hz^{-1/2}}$ for a circular sensitive area with a 0.25 µm diameter or $S_B^{1/2} \sim 0.3 - 3\,\mathrm{nT\,Hz^{-1/2}}$ for a 1 µm diameter. The best-performing 1 µm Hall sensors (see Figure 4.9) exhibit $S_B^{1/2} \sim 80\,\mathrm{nT\,Hz^{-1/2}}$. While the detection limit for SQUIDs is clearly superior to the detection limit of the Hall

sensors reported here, it is still comparable. Considering the different expected size scaling relationships for each type of sensor ($S_B^{1/2} \propto w^{-1}$ for a Hall sensor with width w; $S_B^{1/2} \propto d^{-2}$ for a SQUID with diameter d), Hall sensors may have the potential to outperform sub-micron SQUIDs at high frequencies following implementation of more sophisticated readout techniques.

2.3.2 Random telegraph noise

In micrometer-scale devices fabricated from two-dimensional conductors, the presence of activated two-level charge traps gives rise to so-called random telegraph noise (RTN). The characteristic RTN voltage noise spectrum is Lorentzian, constant at low frequency and and with a power spectral density $S_V \propto f^{-2}$ (voltage spectral density $S_V^{1/2} \propto f^{-1}$) at high frequency [52]. Whereas such noise is not as common in SQUIDs, its presence in Hall sensors introduces non-generic features in the noise spectrum that change upon tuning the devices with electrostatic gates [44, 46, 53]. These charge traps are incorporated unintentionally during fabrication, and their behavior can change over time (see Section 4.4.1).

2.3.3 Flicker noise

Flicker (commonly $1/f$) noise is pervasive in micrometer-scale devices and is the main relevant noise source in both Hall sensors and SQUIDs at sub-kilohertz frequencies [39]. Though several models have been proposed, the precise origin of flicker noise is still not well understood. Flicker noise originates most likely from random charging and discharging of an ensemble of RTN sources

with a large energy distribution, leading to a noise spectrum with characteristic frequency dependence $S \propto f^{-1}$ ($S^{1/2} \propto f^{-1/2}$) [54]. This is often evaluated using the empirical Hooge relation [55]

$$\frac{S_I}{I^2} = \frac{\alpha}{Nf},$$

where S_I is current power spectral density, I is current, α is a material- or device-dependent dimensionless Hooge parameter, N is the total number of charge carriers, and f is frequency.

In SQUIDs, flicker noise likely originates from charge-trap defect states in the Josephson junction oxide layer or pinning sites for trapped superconducting vortices in the niobium [25, 39, 56]. The relationship between the noise amplitude and the physical dimensions of the SQUID loop is not well understood [57], so the flicker noise needs to be carefully evaluated for each individual design.

In Hall sensors, charging events simultaneously modulate the carrier mobility and carrier density, causing fluctuations in the longitudinal current particularly at low carrier density [58]. These fluctuations couple into the Hall voltage in such a way that is expected to depend on the geometry of the conductor [59]. Moreover, the amplitude of $1/f$ noise varies across devices, depending on the material system and external factors including fabrication processing history, choice of substrate, dielectric environment, types of contacts, and biasing conditions [58]. While flicker noise is generally unavoidable outright, so-called "spinning current" techniques may be able to suppress $1/f$ contributions to the total noise spectrum [51, 60].

Despite the wide variety of mechanisms causing $1/f$ noise, there are some commonly observed dependencies. To first order, the Hall voltage power spectral density S_V is expected to scale proportionally with S_I and can be described

with a modified Hooge parameter α' [59]. If the total number of charge carriers contributing to the $1/f$ noise scales with carrier density n and Hall cross width w as $N \propto nw^2$, the voltage noise is

$$S_V^{1/2} = \frac{I}{w}\left(\frac{\alpha'}{nf}\right)^{1/2}.$$

For a device with longitudinal resistance R, the corresponding detection limit is

$$S_B^{1/2} = \frac{S_V^{1/2}}{IR_{\mathrm{H}}} = \frac{eR}{w}\left(\frac{\alpha' n}{f}\right)^{1/2}.$$

For a two-dimensional conductor with sheet resistance ρ, if the length L and width w scale by the same factor, $R = \frac{L}{w}\rho$ is independent of w. Therefore, the detection limit is expected to scale as $S_B^{1/2} \propto w^{-1}$ [45]. This approximate scaling of the detection limit is consistent with the detection limit estimates for graphene-based Hall sensors discussed in Section 4.6.

2.3.4 Combined noise model

Figure 2.3 provides examples of noise spectra from a graphene-based Hall sensor (see Chapter 4) exhibiting a combination of different noise sources. In this device, the type and amplitude of noise changes upon tuning the device with an electrostatic gate [44, 45]. The lowermost curves in Figure 2.3(a,e) are indicative of a spectrum dominated by flicker noise, while the upper curves demonstrate activation of a single dominant RTN source superimposed on a flicker noise background. In real-time, the voltage fluctuates between two charged states on average separated by a voltage δV (Figure 2.3(b)). The distribution of each these voltages is Gaussian (Figure 2.3(c)), and the lifetimes t_1 and t_2 each follow a Poisson distribution (Figure 2.3(d)) [61]. Fitting the lifetimes to an $\exp(-t/\tau)$ de-

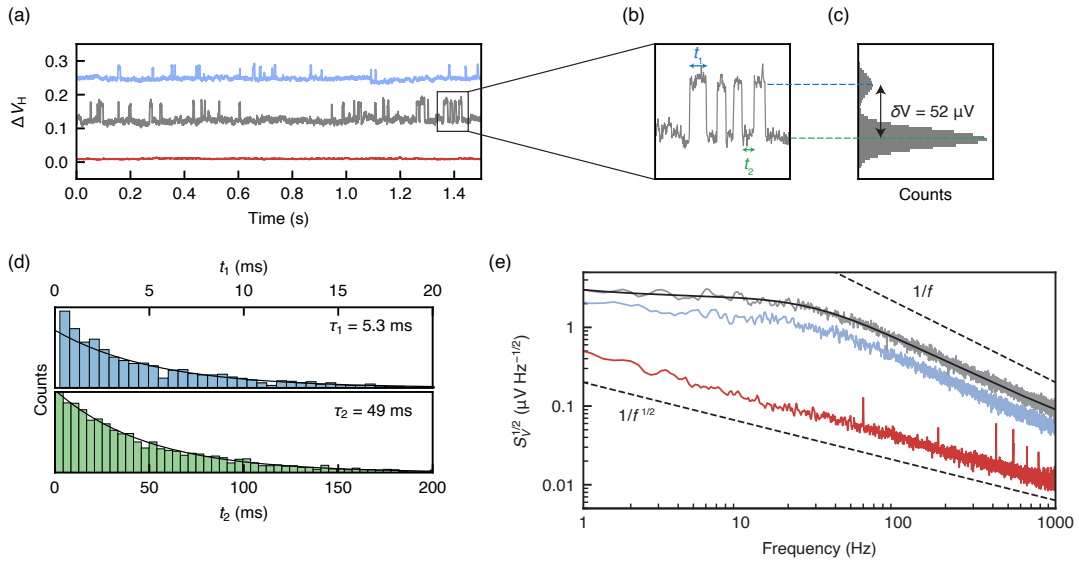

Figure 2.3: (a) Voltage time traces obtained from a graphene-based Hall sensor (see Chapter 4). (b) Zoom-in of a voltage trace fluctuating between two voltage states with lifetimes t_1 and t_2. (c) Voltage histogram from the entire 2.2-second time trace. (d) Histograms of the lifetimes of the two voltage states. (e) $S_V^{1/2}$ spectra for the time traces in (a).

pendence yields a mean lifetime of $\tau_1 = 3.9$ ms for the upper state and $\tau_2 = 49$ ms for the lower state.

Modeling the total voltage noise spectral density as a combination of RTN, $1/f$, and thermal noise [52],

$$S_V = \frac{4(\delta V)^2}{\tau_1 + \tau_2} \frac{\tau^2}{1 + (2\pi f \tau)^2} + \frac{A}{f^\alpha} + 4k_B T R. \tag{2.1}$$

Fixing $\alpha = 1$ and ignoring the final term (a valid assumption at low temperature), modeling the spectrum in Figure 2.3(e) with Equation 2.1 yields best-fit parameters $\delta V = 52.5 \pm 0.5\,\mu$V, $\tau_1 = 6.09 \pm 0.09$ ms, $\tau_2 = 49.0 \pm 0.9$ ms, and $A = 3.1 \pm 0.3 \times 10^{-12}$ V. The values of δV, τ_1, and τ_2 agree well with those found directly from the RTN analysis above. This example illustrates a possible approach to extract relevant $1/f$ and RTN contributions to the noise spectral density and track differences across devices, and for different experimental configu-

rations for each individual device. However, it is often practically more straightforward to choose a reference frequency (e.g. 1 kHz) and compare noise across devices or conditions at that particular frequency, as I consider in Section 4.4.

2.4 Considerations for scanning with planar magnetometers

Achieving a small sensor-to-sample distance is essential towards the proper implementation of a scanning probe microscopy technique. For planar SQUIDs and Hall sensors fabricated on silicon chips, this requires the sensitive area to be positioned at the edge of a terrace near the corner of the chip (Figure 2.4(a)), which can be a challenging feature to add during the fabrication process. To that end, manual mechanical polishing can be used to create an artificial chip corner surrounding the pickup loop (Figure 2.4(b)), but this is a risky and time-consuming technique. Alternatively, a deep trench surrounding the sensitive area and careful dicing of the chip can achieve a similar geometry, but this imposes a different set of fabrication challenges (see Section 2.4.1).

Both methods for positioning the sensitive area near a chip corner enable

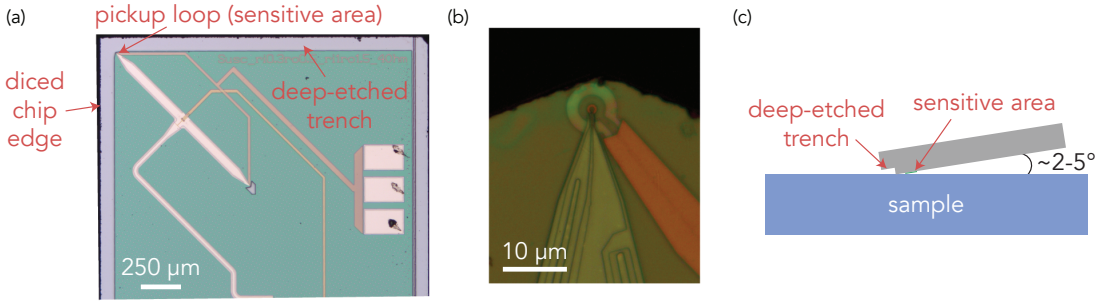

Figure 2.4: (a) Overview of scanning SQUID magnetometer chip with integrated deep etch. (b) Polished SQUID chip (polishing and picture courtesy Alexander Jarjour). (c) Probe and sample alignment geometry.

the scanning geometry illustrated in Figure 2.4(c). Here, the chip is oriented at a shallow angle to the sample in such a way that guarantees that topographically raised features or the corner of the chip touch the sample first upon engaging. This avoids potential damage to the sensitive area from physical contact to the sample. This scanning geometry motivates positioning the sensitive area as close as possible to the corner of the chip, and at the same time it suggests a need for topographically flat samples.

For more delicate samples, it is also often useful to scan out of contact. One approach to achieve this is to engage on the sample with the chip corner to find the sample surface, map out the sample surface over the desired scan area, and scan over the surface by a specified distance. This is difficult in practice because of the nonlinearity and drift of piezoelectric benders used to scan the sensor over the sample, leading to an uncertainty in scan height and minimum scan height of 0.1 µm at best [28]. Active feedback on the sensor-to-sample distance, for example using the resonance of a quartz tuning fork [49, 62], can potentially enable scanning at a constant, small scan distance.

The next two sections describe baseline deep etch fabrication procedures for planar scanning probe magnetometers fabricated on silicon substrates. I developed these processes specifically for SQUID magnetometers (with a similar design as in Ref. [27]) and graphene-based Hall sensors (discussed at length in Chapter 4). There are substantial differences between the two processes, and it may be possible to follow a hybrid approach combining steps from each process. Both processes ultimately achieve the same end goal: positioning the sensitive area of a magnetic field sensor near the corner of a plateau to enable close approach to samples of interest.

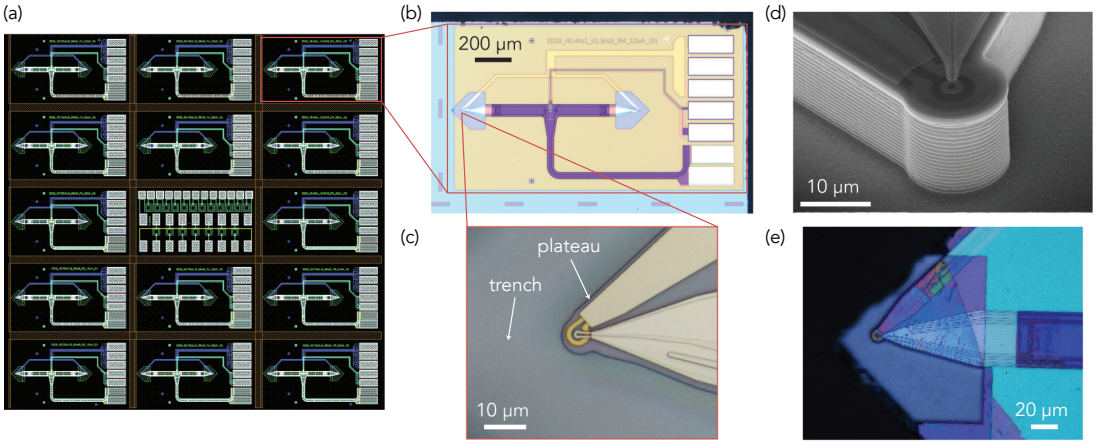

Figure 2.5: (a) Schematic of SQUID die. (b) Microscope image of individual SQUID chip. (c) Microscope image of deep-etched SQUID with pickup loop inner diameter 0.8 µm. (d) Scanning electron microscope image of deep-etched SQUID with pickup loop inner diameter 1.5 µm. (e) Microscope image of diced SQUID chip.

2.4.1 Deep etch process developed for scanning SQUIDs

The fabrication of our SQUID magnetometers is performed by HYPRES, Inc., a fab house specializing in superconducting electronics based on $Nb/AlO_x/Nb$ trilayer Josephson junctions. The final received 5 mm × 5 mm chips contain multiple SQUID die (Figure 2.5(a)). The pickup loop of each individual SQUID lies on top of and is surrounded by a region filled with ~1.1 µm of SiO_2 and SiN_x layers from previous steps in the fabrication process (pentagonal regions in Figure 2.5(b)). Deep-etching therefore requires reactive-ion etching this oxide layer, followed by a deep reactive-ion etch through the silicon substrate to a depth of ~10-20 µm.

I fully describe the deep etch process in Appendix B.5 and highlight some key features here. The prime challenge in developing this process was the potentially small thermal budget, as excessive heating during fabrication can reduce the critical current of the Josephson junctions. I therefore used efficient

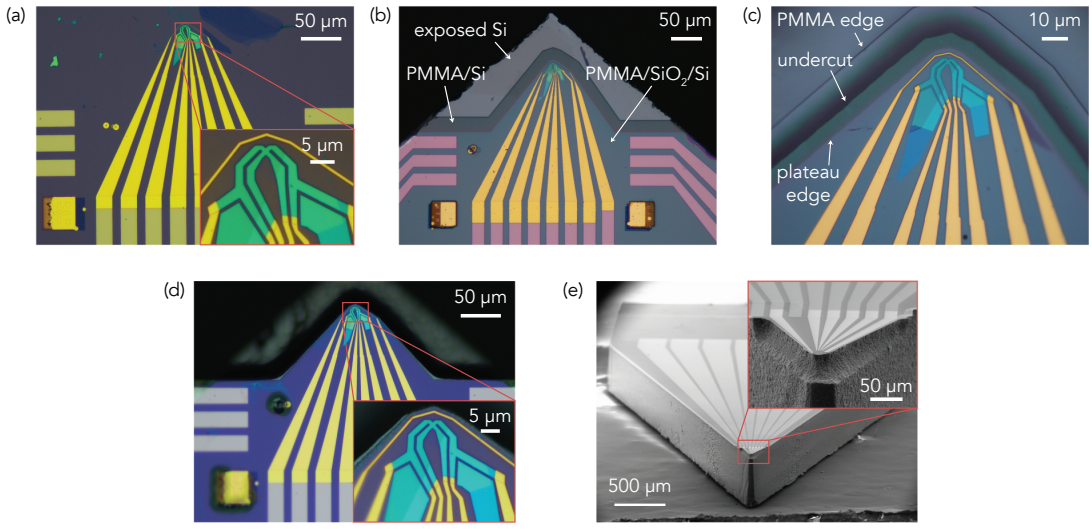

Figure 2.6: Graphene-based Hall sensor in various stages of the deep etch process: (a) prior to deep etching, (b) just prior to silicon etching, (c) partway through the silicon etch, (d) optical and (e) scanning electron microscope images post deep etching.

and selective etch processes and use a carrier wafer with helium backside cooling to mitigate substrate heating during the etch process. Figure 2.5(c-d) shows the pickup loop after a ~10 µm deep etch using a standard oxide etch and Bosch silicon etch. The ridges in the sidewall are a result of the Bosch process. After etching, I diced the 5 mm × 5 mm chips into individual SQUID die, and then again used the dicing saw to create an artificial chip corner near the pickup loop (Figure 2.5(e)). This final dicing step needs to be done for each individual SQUID, but it eliminates the need for mechanical polishing [25].

2.4.2 Deep etch process developed for Hall sensors

Graphene-based Hall sensors as described in Chapter 4 consist of exfoliated flakes of two-dimensional materials, and as a result the geometry of each device and its location relative to patterned alignment marks is somewhat unique (see

e.g. Figure 3.10). This motivates the use of electron-beam (e-beam) lithography or direct-write photolithography, in which patterning does not involve a static mask. I developed an e-beam lithography recipe for deep etching, since most of the other fabrication steps for graphene-based devices also involve e-beam lithography (see Section 3.4).

Appendix B.6 lists full process details for deep etching previously fabricated graphene-based Hall sensors (Figure 2.6(a)). Like the deep etch process for SQUIDs, the process here involves etching through an oxide layer (285 nm) followed by deep etching a trench in the underlying silicon. It is unlikely that these devices have a thermal budget for the process, as graphene devices are often annealed at high temperatures to improve device performance [63, 64]. To etch the oxide, I pattern a thick PMMA resist mask and use a standard oxide plasma etch lacking substrate cooling, performed in three stages to manually cool the substrate periodically. I then spin and expose another resist mask, but before developing dice the chip to position the device near the end of a pointed tip (Figure 2.6(b)). Maintaining an intact resist layer is necessary to protect each device from damage from the cooling water or particulates during the dicing process. Graphene-based devices are quite fragile compared to SQUIDs; poor adhesion between the layers in the graphene-based heterostructure requires special care, especially when the device is positioned near the edge of the substrate.

I use a xenon difluoride (XeF_2) chemical etch process to create a deep-etched trench in the silicon. XeF_2 is a molecular solid whose vapor reacts spontaneously with silicon providing a highly selective isotropic chemical etch. This etch is most commonly used for removing sacrificial layers in the fabrication of micromechanical devices, but it can also be used for etching hBN (see Ap-

pendix B.3). In addition to being quite selective, typically capable of etching to depths on the 10 µm scale with PMMA resist, the etch is plasmaless and therefore compatible with exposed materials (e.g. Au) that are typically not compatible with plasma processes. Because it is isotropic, the XeF_2 etch process creates as much undercut as it does depth. It is therefore necessary to design a resist mask for this etching step that anticipates the undercut, with the edges of the mask displaced by the same amount to be deep etched. I carefully monitor the undercut optically (Figure 2.6(c)) and stop the etch when the undercut has reached the intended edge of the plateau, with an accuracy of approximately 1 µm. The final device (Figure 2.6(d,e)) achieves the intended goal: a Hall sensor positioned at the edge of a plateau, surrounded by a deep-etched trench, and located at a corner of the chip.

2.5 Interpreting magnetic flux images

Both SQUIDs and (ballistic) Hall sensors involve measurements of magnetic flux through a sensitive area with finite geometry,

$$\Phi = \iint \mathrm{d}\boldsymbol{S} \cdot \boldsymbol{B}(\boldsymbol{r}), \tag{2.2}$$

which is an integral over the surface of the sensitive area, with infinitesimal surface element $\mathrm{d}\boldsymbol{S}$. The shape and size of the sensitive area can therefore lead to distorted features in the obtained flux images.

Figure 2.7(a) demonstrates this effect in a scanning SQUID microscopy image of the magnetic flux originating from Abrikosov vortices in a bulk sample of superconducting Nb. The imaged vortices clearly appear asymmetric, with extended tails that "smear" the vortices towards the bottom of the image. This is a

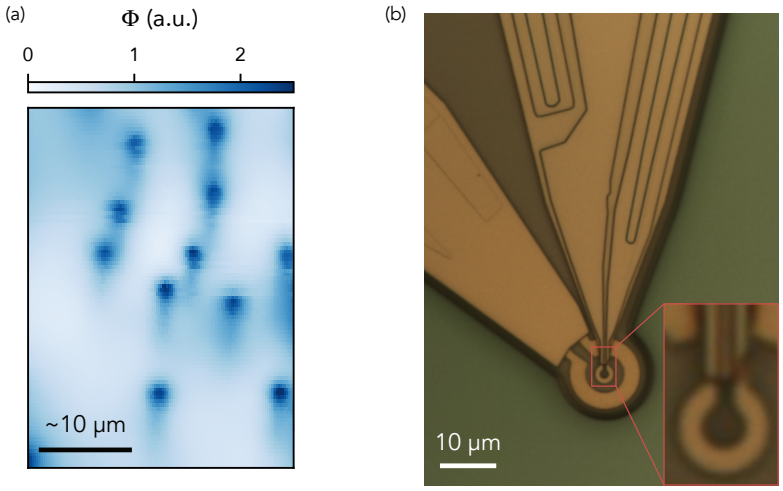

Figure 2.7: (a) Magnetic flux image of Abrikosov vortices in bulk superconducting Nb (sample courtesy Ryan Porter, Cornell). (b) Optical image of the SQUID magnetometer used for the measurement (image courtesy Alexander Jarjour, Cornell). The SQUID is oriented as shown, with the end of the pickup loop pointing towards the bottom of the image.

direct result of the "bulb thermometer" shape of the pickup loop (Figure 2.7(b)) and similar shape of the point spread function, describing the response of the sensor to a point source of magnetic field. Each vortex can be described well as a point-like source of magnetic field with a well-defined monopolar spatial dependence (see below), and therefore images of vortices provide a good calibration for the point spread function [14, 65]. Accounting for the point spread function is important for interpreting magnetic flux images. In the following section, I consider an idealized square point spread function and demonstrate how it affects the images of a few common magnetic field sources.

2.5.1 Magnetic flux from common magnetic sources

The magnetic landscape above the surface of materials can originate from a variety physical phenomena, but it is instructive to consider three primary sources of magnetic field: a magnetic monopole*, a magnetic dipole, and electric currents. These building blocks can be used in superposition to model more complex magnetic features, at least to first order. For example, a finite-size 2D magnetic domain can be modeled equivalently by either a continuous array of dipoles or a current flowing at the boundary.

The magnetic field from each source exhibits a distinctive spatial dependence and varies uniquely with scan height, as discussed in Ref. [28, 39]. We revisit this concept here to visualize concrete examples of magnetic *flux* images above each of the sources. Below, I write the out-of-plane magnetic field B_z for each of the sources as a function of the position (x, y, z) relative to the source, along with the maximum value in the x-y plane $B_z^{\max}$ as a function of scan height z [39, 66]:

- Monopole (with total integrated flux Φ_0):

$$B_z(\boldsymbol{r}) = \frac{\Phi_0}{2\pi} \frac{z}{(x^2 + y^2 + z^2)^{3/2}}$$

$$B_z^{\max} = B_z(x = y = 0) = \frac{\Phi_0}{2\pi z^2} \propto z^{-2}$$

*Pure magnetic monopole sources are of course forbidden by Maxwell's equations, but some magnetic fields can be well approximated by a monopolar field. Concretely, the magnetic field originating from an Abrikosov vortex in a type-II superconductor is well approximated by a monopole located a distance beneath the surface of the superconductor equal to the London penetration depth [28, 65].

- Dipole (for a source with magnetic moment m):

$$B_z(\boldsymbol{r}) = \frac{\mu_0 m}{4\pi} \frac{2z^2 - x^2 - y^2}{(x^2 + y^2 + z^2)^{5/2}}$$

$$B_z^{\max} = B_z(x = y = 0) = \frac{\mu_0 m}{2\pi z^3} \propto z^{-3}$$

- Line of current I (flowing in the $+y$ direction through an infinitesimal wire):

$$B_z(\boldsymbol{r}) = \frac{\mu_0 I}{2\pi} \frac{x}{x^2 + z^2}$$

$$B_z^{\max} = B_z(x = z) = \frac{\mu_0 I}{4\pi z} \propto z^{-1}$$

Figure 2.8 shows normalized magnetic flux images for a series of scan heights z_0 computed using a $a = 0.3\,\mu\text{m}$ square sensitive area (see Appendix A for full expressions). These images illustrate visually the relationship between scan height and spatial resolution and can be generalized to different sensitive area sizes by scaling the z_0 and a proportionally*. The approximate spatial resolution for each image is $\min(z_0, a)$; when $z_0 < a$ the shape of the sensitive area is visible in the images, and when $z_0 > a$ the blurred features approximately have a size equal to the scan height.

Figure 2.9 clarifies the scan height dependence of the characteristic flux from each source, alongside the apparent width of the features (as defined in Figure 2.9(a)). To understand how the apparent size of the features can affect magnetic flux images, I consider in Figure 2.9(d) a series of expected images above two monopole sources for three different scan heights. For a scan height much smaller than the distance between monopoles, the monopoles are clearly distinguishable, but when the scan height approaches this separation, they become

*e.g., the central row of images is valid for the condition $z_0/a = 1$

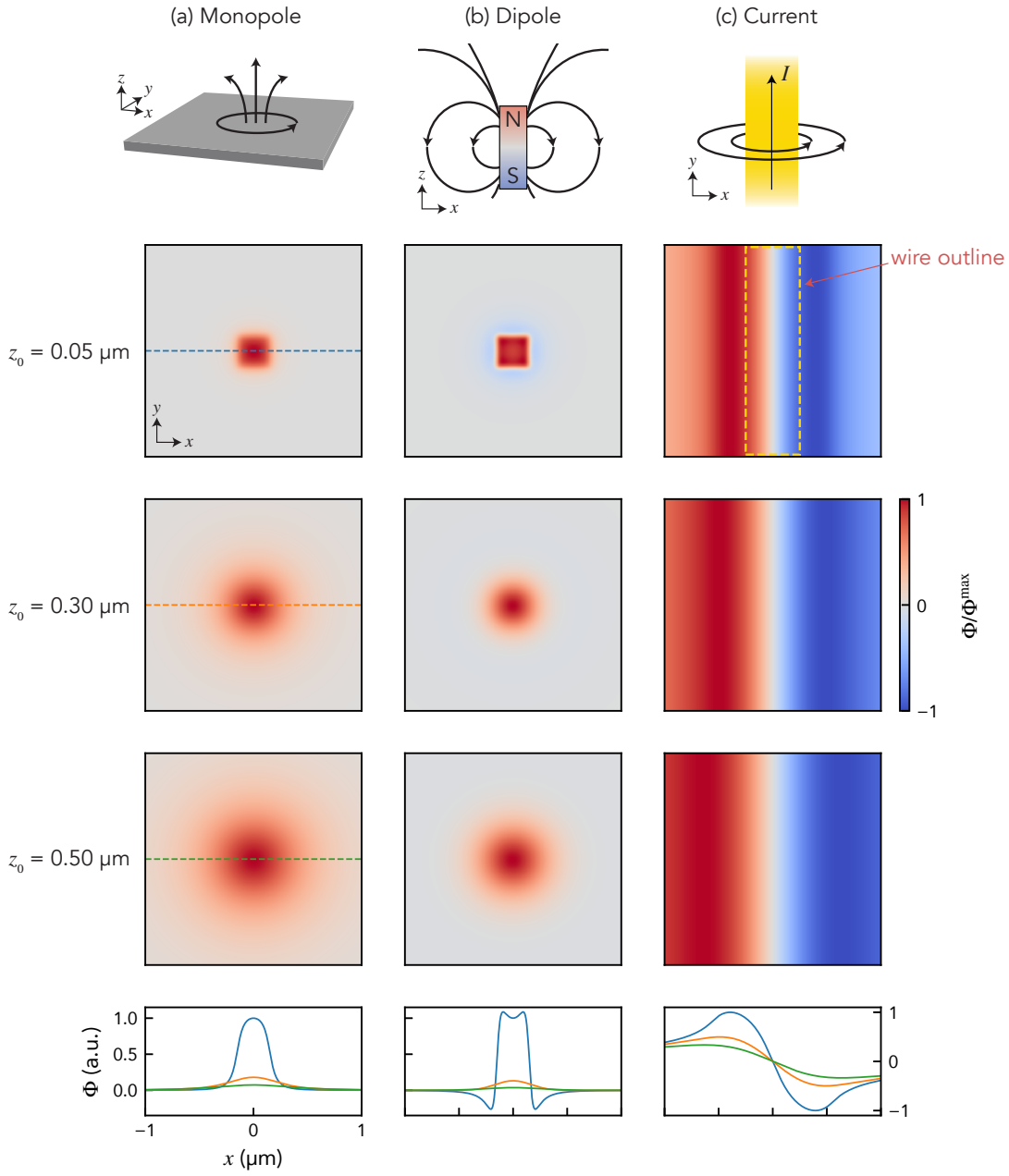

Figure 2.8: Calculated images of of magnetic flux Φ at the indicated scan height z_0 for (a) monopole (Abrikosov vortex), (b) dipole (bar magnet), and (c) current (infinite wire) sources. The flux is calculated using a $a = 0.3\,\mu$m square sensitive area. The bottom row of panels are cross sections along the central horizontal line in each image (dashed lines in the x direction). Each image is normalized by the maximum flux with the same image, and each line profile is normalized by the maximum flux at $z_0 = 0.05\,\mu$m.

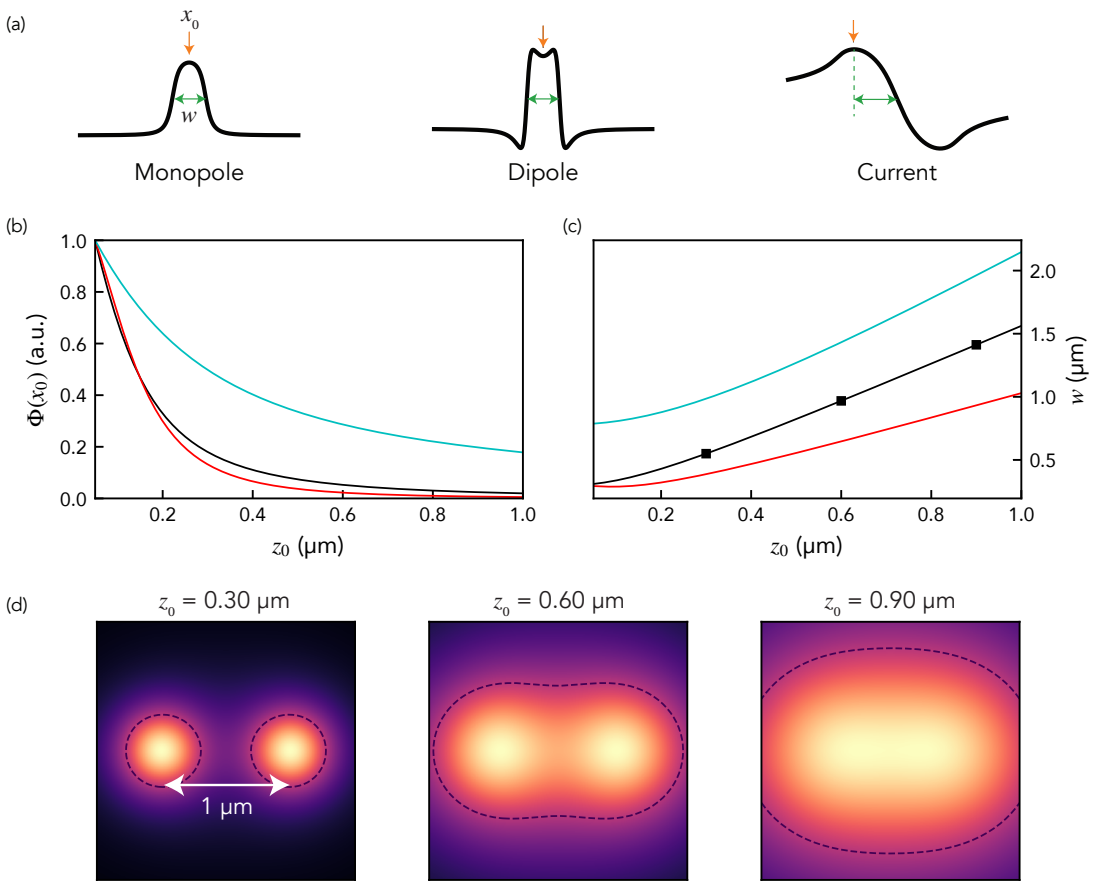

Figure 2.9: (a) Schematic line profiles of the magnetic flux from monopole, dipole, and current sources. The flux is calculated using a $a = 0.3\,\mu\text{m}$ square sensitive area. The central panels show the dependence on scan height z_0 of (b) characteristic flux $\Phi(x_0, z_0)$ and (c) feature size w, with x_0 and w as indicated in (a). In (b), the flux is normalized to a maximum of 1 at $z_0 = 0.05\,\mu\text{m}$. (d) Height series of normalized flux images above two monopoles spaced 1 μm apart. The dashed contours mark $\Phi(x, y)/\Phi^{\max} = 1/2$.

indistinguishable. This observation motivates attention towards designing sensors enabling a small scan distance (see Section 2.4).

2.6 Conclusion

The overview of scanning magnetometry in this Chapter mainly provides context for the Hall sensors discussed in Chapter 4 (and the technique is briefly mentioned in Chapters 5 and 6). The details here are merely a cross-section of some of the important considerations in realizing such an experimental tool, and I direct the reader to Refs. [26,34,39,67,68] for further information. Scanning magnetometry is an exciting technique undergoing constant improvement, and I look forward to future developments that will lead to new studies of magnetic phenomena.

CHAPTER 3

FABRICATION OF HIGH-QUALITY GRAPHENE DEVICES

In this Chapter, I describe in detail fabrication procedures for high-quality graphene devices consisting of monolayer graphene (MLG) or bilayer graphene (BLG) encapsulated with hexagonal boron nitride (hBN) and sometimes few-layer graphite (FLG). According to the literature, this sandwich-like structure enables the creation of two-dimensional electronic systems with high electronic quality [69, 70] only potentially rivaled by cobaltates [71] or doped semiconductor structures [72], material systems requiring specialized processing techniques. After adopting this process, I was able to create devices just as clean as the best reported in the literature. I benefited greatly from the mentorship of Lei Wang and Marcos Guimarães, two postdoctoral researchers at the Kavli Institute at Cornell who both worked at the forefront of high-quality graphene devices during their PhDs.

This Chapter begins with a brief review of van der Waals heterostructures. I then describe my approach towards creating graphene- and hBN-based heterostructures, involving mechanical exfoliation of flakes from bulk crystals, sequential stacking of flakes, and transfer of the final stack to a substrate. Next, I explain microfabrication procedures for etching devices into the desired shape, depositing metal contact electrodes, and adding a metal top gate to the device structure. Finally, I describe best practices that I followed to prepare the samples for electrical measurements.

3.1 Principles of van der Waals heterostructure fabrication

In this section, I review van der Waals heterostructures consisting of multiple stacked layers of two-dimensional (2D) layered materials (see for example [73–76]). These materials possess strong covalent bonds between atoms within each layer, but weak van der Waals interactions between atoms in different layers. Nearly all condensed matter systems are represented within this family of 2D materials, including metals, semiconductors, insulators, superconductors, and magnets. The weak interactions between layers enables stacking different materials on top of each other in succession to create a structure consisting of, in principle, arbitrary permutations of material layers. Moreover, the lack of dangling bonds at the surfaces of each layer helps promote the formation of clean, precise, and atomically smooth interfaces between the layers, leading to the design of material systems with extraordinary electronic properties.

Material systems involving graphene, a single sheet of carbon atoms in a hexagonal lattice, and hexagonal boron nitride (hBN), a material with similar structure to graphene but with alternating boron and nitrogen atoms, comprise perhaps the most famous and impactful devices so far from van der Waals heterostructures. Such devices often involve a sheet of either monolayer or bilayer graphene (MLG or BLG) as the active layer of the device, surrounded by insulating hBN, which in turn is in some cases surrounded by few-layer graphite (FLG), consisting of a few tens of layers of graphene. This structure creates an electronic system with extremely low charge inhomogeneity in the active graphene layer (see Section 4.3), leading to for example the observation of rare fractional quantum Hall states at high magnetic fields [64, 69, 70].

Van der Waals heterostructures also enable unprecedented control over a new degree of freedom: the relative twist angle between layers. The near-alignment of MLG on hBN, for example, creates a moiré superlattice leading to a distinct sequence of fractional quantum Hall states at high magnetic field [64]. The exploration of so-called "twistronic" van der Waals devices especially became a popular research thrust after the simultaneous discovery of correlated insulating and superconducting phases in twisted bilayer graphene [77].

The van der Waals stacking technique is relatively straightforward, inexpensive, and useful for prototyping novel device structures. Nearly all the materials and tools needed for the assembly of van der Waals heterostructures are readily available from standard laboratory suppliers and require little maintenance. Moreover, the dry-transfer procedure (see Section 3.3) offers the capability to interface completed heterostructures with a variety of substrates, including strainable polyimide (see Section 6.2). However, van der Waals fabrication is currently not scalable, motivating the development of growth techniques for wafer-scale heterostructures, like those used in the production of high-quality semiconductor- and oxide-based material systems.

3.2 Mechanical exfoliation

The highest-quality van der Waals devices are typically fabricated from layers obtained by mechanical exfoliation of bulk crystals, a process that involves cleaving the bulk crystals to deposit smaller, thinner flakes onto a silicon substrate. The size and thickness of flakes obtained using this technique depends on the material, substrate, and details of the technique. In the following sec-

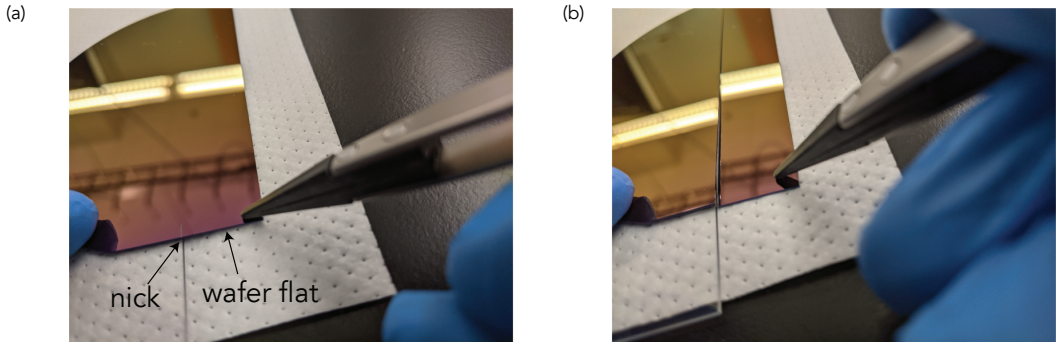

Figure 3.1: Bare silicon wafer (a) just prior to cleaving, (b) just after cleaving.

tions, I describe my approach towards obtaining exfoliated MLG, BLG, FLG (up to ~5 nm thick), and hBN (typically 10-40 nm thick).

3.2.1 Substrates

As substrates for the exfoliated flakes, I use silicon wafers (NOVA Electronic Materials) with 285 nm of wet thermal oxide. The specific oxide thickness is a standard choice, enhancing the contrast of graphene when viewed under an optical microscope [78]. To cleave the wafers, I first use a diamond scribe to nick the edge of the wafer in a direction perpendicular to the wafer flat (Figure 3.1(a)). Then, I support the wafer underneath with a glass slide, align the nick to the edge of the slide, and press down on the free end with tweezers to cleave the wafer cleanly along a high-symmetry crystal axis (Figure 3.1(b)). I continue cleaving along the perpendicular direction to create ~1 cm $\times$ 3 cm pieces convenient for exfoliation and blow off residual particles using compressed nitrogen. These wafers as received from the manufacturer are of suitable cleanliness for exfoliation. Treating the wafers with standard cleaning solutions (e.g., acetone, isopropanol, Nanostrip, piranha etch) may pose the unnec-

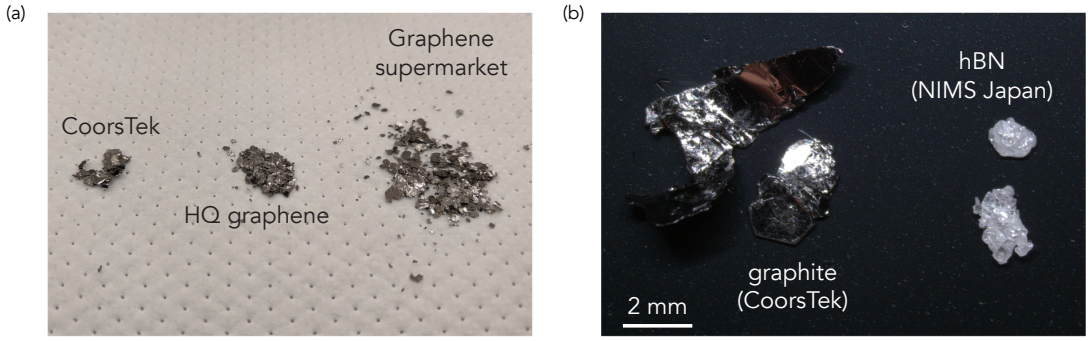

Figure 3.2: (a) Various bulk graphite crystals. (b) Best-performing bulk graphite and hBN crystals from CoorsTek and the National Institute for Materials Science in Japan.

essary risk of leaving unwanted chemical residues on the wafer surface. I had reasonable success using a gentle 5-minute oxygen plasma to promote adhesion of graphene to silicon [79], but this often made later manipulation of the flakes more difficult.

3.2.2 Material sources

The crystal quality of exfoliated flakes is directly related to the quality of the source crystals. Graphite and hBN crystals are available commercially from a number of sources marketing towards graphene researchers, but the shape, size, and quality of flakes varies drastically between brands (Figure 3.2(a))*. Following recommendations from members of Cory Dean's research group at Columbia University, I was ultimately most successful using Kish graphite (CoorsTek, 62K1002) and hBN crystals grown using a high-pressure tech-

*Notably, I obtained a one-pound (!) free sample of Momentum PolarTherm PT110 hBN from the manufacturer. I could not turn down a free lifetime supply of hBN, but did not end up using this source due to the relatively poor crystal quality.

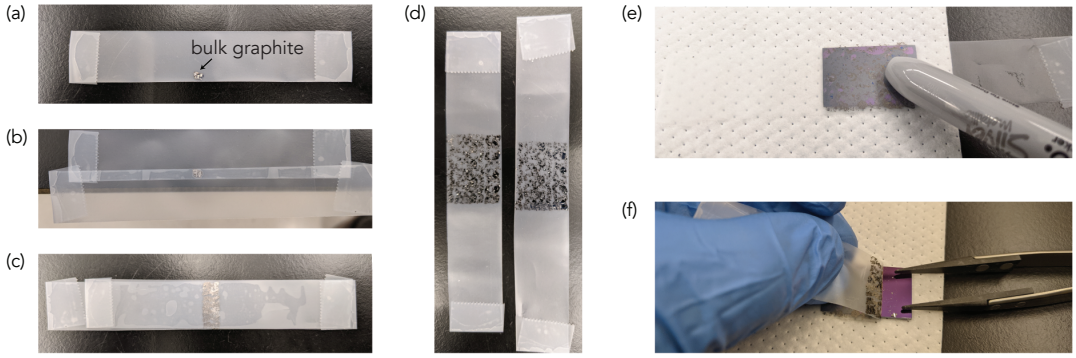

Figure 3.3: (a) Source graphite flake at the edge of a strip of Scotch tape. (b) Second strip of Scotch tape overlapping original flake. (c) Tape strips after repeated copying of original flake. (d) Final strips of tape coated with flakes. (e) Adhering tape to substrate and rubbing gently with plastic marker. (f) Removing the tape from the substrate.

nique, the latter graciously provided by collaborators Takashi Taniguchi and Kenji Watanabe from the National Institute for Materials Science in Japan (Figure 3.2(b)) [80]. Not only do these crystals yield a larger number of usable large-area flakes, but devices fabricated from these flakes also tend to perform better than devices using flakes obtained from other sources.

3.2.3 Exfoliation using adhesive tape

The next step in the exfoliation process is to repeatedly cleave the bulk crystals using adhesive tape. Famously, 3/4-inch Scotch® Magic™ tape is the "classic" choice for graphene exfoliation, and it is indeed the product I recommend. While low-tack wafer dicing tape can be easier to work with, I have found that the adhesive often leaves behind a residue on the surface of the exfoliated flakes rendering them unusable. Exfoliation is most effective when done in a consistent manner, and I followed the procedure described below (various steps illustrated in Figure 3.3):

- Obtain four 10-15 cm strips of tape from the roll; fold over the ends to create non-sticky tabs to facilitate handling.
- Choose a few bulk flakes from the source and arrange compactly near the edge of one strip of tape, covering a ~$2 \times 2\,\mathrm{mm}^2$ area (Figure 3.3(a)).
- Position a second strip of tape over the flakes, overlapping minimally with the first strip (Figure 3.3(b)). Press lightly on the back side of the top strip above the flakes to encourage adhesion.
- Carefully separate the pieces of tape, creating a "copy" of the flake arrangement on the second strip.
- Position the second strip over the first strip such that the collections of flakes on each strip are bordering each other but not overlapping. Again, press lightly to encourage adhesion.
- Repeat this process until the flakes cover the entire width of both strips of tape (Figure 3.3(c)). Then, repeat the process shifting the strip horizontally until 3-4 cm of the tape is coated with flakes and is a slightly lustrous, fairly uniform grey color, a result of cleaving ~7-8 times in total (Figure 3.3(d)).
- Position each remaining unused strip of tape directly over each flake-coated strip, press together, carefully pull apart, and discard the original strips of tape. This final cleaving step makes the top surfaces of the flakes more likely free from adhesive residues.
- Carefully adhere the flake-coated strip of tape to the prepared substrate, avoiding the formation of air bubbles between the tape and substrate (Figure 3.3(e)).
- Use the rounded back end of a plastic marker to gently apply pressure to the back side of the tape.

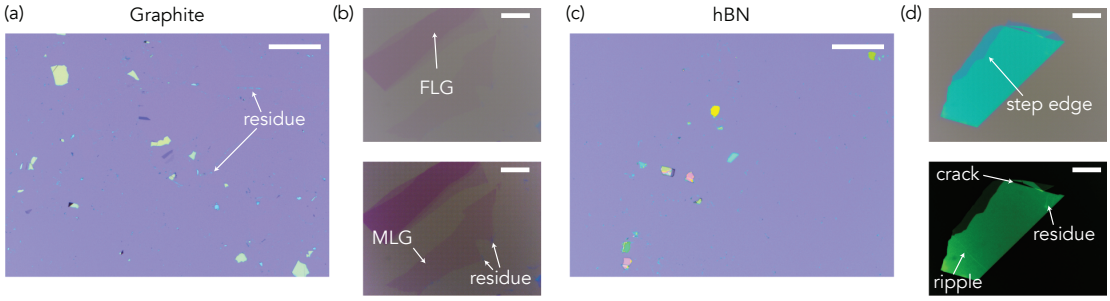

Figure 3.4: Optical microscope images of (a,b) graphite and (c,d) hBN flakes exfoliated onto silicon substrates with 285 nm SiO_2. In (b) and (d), the top image is an original microscope image and the bottom image is the same image with color contrast digitally enhanced. This reveals imperfections including ripples, cracks, residues, and step edges as indicated. Scale bars: (a,c) 400 µm (b,d) 20 µm.

- Heat the tape/substrate assembly on a hot plate at 100 °C for 5 min.
- Remove the tape/substrate assembly and rest on lab bench for up to 30 s until cool to the touch.
- Carefully peel the tape away from one edge of the substrate, press down on the exposed edge with tweezers, and continue to peel the tape at a moderate rate until it is completely detached (Figure 3.3(f)).

3.2.4 Flake selection and heterostructure planning

At this point, the surface of the substrate is coated with a variety of exfoliated flakes (Figure 3.4(a,c)). Selecting suitable flakes to incorporate into heterostructures is now a matter of finding "needles in a haystack," sifting through the flakes on the substrate to find flakes of appropriate size, shape, and thickness. The areal density of flake coverage often varies between runs, possibly a result of multiple factors including but not limited to: the quality of original flakes, ambient temperature/humidity, substrate surface chemistry, manual pressure

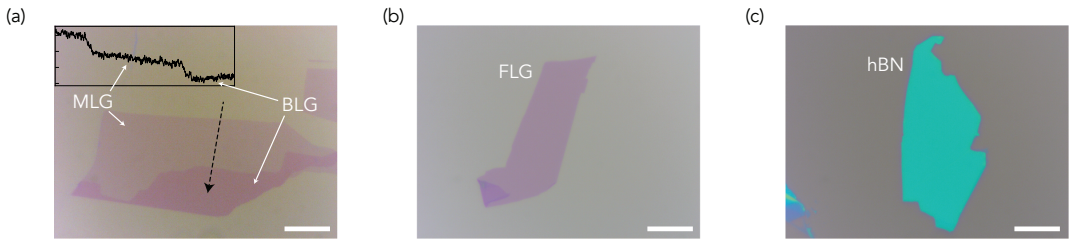

Figure 3.5: Examples of ideal flakes for heterostructures (scale bars: 20 µm). (a) Contrast-enhanced optical image of monolayer and bilayer graphene present within the same flake. Inset: Profile of the greyscale pixel intensity along the dashed arrow. (b) ~3 nm few-layer graphite (FLG) flake. (c) ~42 nm hexagonal boron nitride (hBN) flake. The thicknesses of FLG and hBN flakes are determined using atomic-force microscopy.

during cleaving steps, and the rate of peeling tape from the substrate. Given that the exfoliation process is relatively quick and straightforward, it is often easiest to simply repeat the process a few times until the flake coverage is adequate.

Tape residues on the substrate, unless excessive, are not necessarily problematic. In fact, most exfoliated flakes possess clean surfaces despite the presence of these residues. Most likely, the final cleaving steps create pristine top and bottom surfaces for each flake never in direct contact with the tape. However, flakes with surface residues can lead to heterostructures with undesirable trapped contaminants between the layers [81]. As an initial filtering step for selecting high-quality flakes, I take high-magnification microscope images and enhance the color contrast to highlight possible surface residues and other imperfections (Figure 3.4(b,d)).

There is an art to efficiently identifying flakes that are suitable for 2D heterostructures, requiring both training and intuition to select the best candidate flakes. I systematically scan over the entire surface area of each exfoliation substrate using an optical microscope at high magnification (5× or 10×, with

a ~1 mm field of view as in Figure 3.4(a,c)), pausing to inspect flakes with lateral dimensions $\gtrsim$10 µm. The color of each flake is an indication of its thickness, and developing an intuition for this relationship is essential towards efficiently identifying flakes. While searching for monolayer graphene (MLG) and bilayer graphene (BLG), it is often useful to use a red optical bandpass filter (Thorlabs, GB600-40) to slightly enhance the contrast. MLG flakes can usually be identified by eye as the flakes exhibiting the least contrast compared to the substrate, and BLG flakes are just slightly darker. I recommend finding a flake containing both MLG and BLG regions, as in Figure 3.5(a). A line profile of the greyscale pixel intensity (Figure 3.5(b)) exhibits two distinct jumps of equal size, and the three sharp steps in the profile correspond to the substrate (brightest), MLG, and BLG (darkest). Unless there are other flakes of intermediate brightness present elsewhere on the substrate, it is very likely that the flake identification is correct. If still in doubt, Raman spectroscopy can directly distinguish between MLG and BLG [82].

FLG and hBN flakes often have less precise thickness requirements, but the thickness of each flake can be estimated using atomic-force microscopy (AFM). After repeatedly finding and measuring the thickness of flakes, I learned to identify ~5 nm FLG and ~20-40 nm hBN flakes by color without necessarily requiring AFM. Figure 3.5(b-c) shows examples of typical "dull purple" FLG and "pastel green" hBN flakes.

After selecting suitable flakes for the intended heterostructure, I create approximate polygon outlines for each flake using vector graphics editing software* and plan the layout of each heterostructure before assembly. To illustrate, Figure 3.6 shows such a planned layout, compared with an image of the final

*e.g., Microsoft PowerPoint, Adobe Illustrator

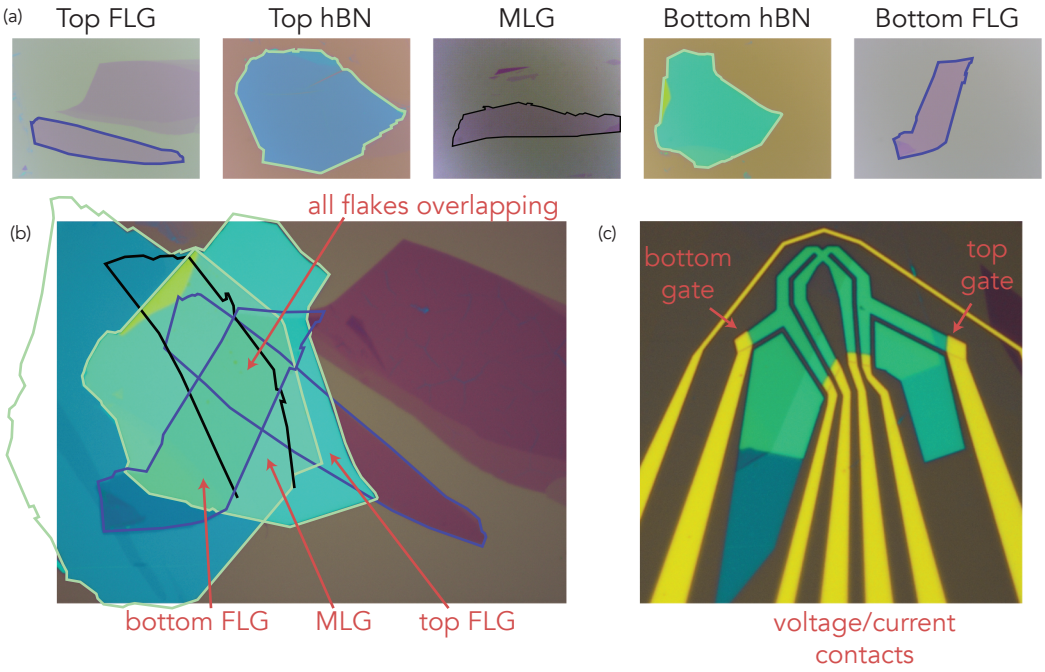

Figure 3.6: (a) Optical images of flakes used in a stack with layer structure FLG/hBN/MLG/hBN/FLG. (b) Planned layout of polygon outlines for each flake superimposed on a microscope image of the final heterostructure. Layout adjusted slightly to match the actual heterostructure as assembled. (c) Final device after plasma etching and contact deposition.

heterostructure. Here, the layers are arranged to enable independent electrical contacts to each MLG or FLG layer, via the edge contact process described in Section 3.4. The large size of the hBN flakes compared to the MLG and FLG flakes helps prevent undesirable contact between the MLG and FLG layers. If these layers happen to overlap in the final assembled heterostructure, the overlapping portions can be etched away to remove electrical shorts. Having a clear plan for the layout is essential towards understanding the final structure of the stacks, planning future fabrication steps, and troubleshooting device performance.

3.3 Dry-transfer procedure for heterostructure assembly

The dry-transfer process for fabricating heterostructures with in principle an arbitrary layer structure is well-established in Refs. [63, 83]. Using this process, I assembled heterostructures (informally, "stacks") layer-by-layer via repeatedly picking up each flake in the structure in sequence using a "transfer slide" (see below). I then released the completed heterostructure onto a final SiO_2/Si substrate for further fabrication steps (Section 3.4). While Refs. [63, 83] already provide sufficient detail describing the basic technique, here I explain my specific approach, incorporating ideas from recently reported modifications to the standard technique that facilitate assembly and improve heterostructure quality.

3.3.1 Transfer slide

The transfer slide is an assembly consisting of a polymer film supported by a viscoelastic polydimethylsiloxane (PDMS) stamp (Gel-Pak PF Gel-Film, X4, 17.0 mil) on a glass microscope slide (Fisherfinest premium plain glass microscope slides, Fisher Scientific). There are several polymers commonly used in the process, but I prefer poly(bisphenol A carbonate) (PC, Sigma Aldrich 43519). Using PC enables using high temperatures during the repeated process of engaging and retracting the stamp, allowing for reliable pickup of flakes. To create the PC film, I followed the technique described below (adapted from Ref. [83]):

- Dissolve PC in chloroform to create a 6% solution (solution can be made well in advance and stored for years)
- Place a drop of the solution on a clean glass slide and spread it out with a

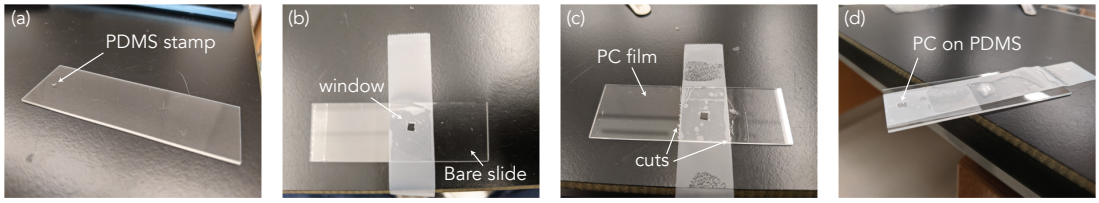

Figure 3.7: (a) PDMS stamp positioned near one end of a glass slide. (b) Strip of Scotch tape on a different slide with a window cut out. (c) The same strip of tape on a slide with PC film, cut at the edges of the tape. (d) Suspended PC film overlaid on the PDMS stamp.

second glass slide. This approach is necessary because chloroform evaporates quickly in air, making spin coating difficult.

- Slide the two slides apart and let dry in air for about a minute
- The resulting slides host reasonably uniform PC films (only a ~2×2 mm^2 uniform region is needed for each transfer slide)

Then, I assembled each transfer slide using the following procedure:

- Cut a ~3×3 mm^2 stamp from the PDMS sheet and place it gently near one end of a glass slide (Figure 3.7(a))
- Slice the stamp with a razor blade down to ~1×1 mm^2, careful to avoid detaching the stamp from the slide*
- Overlay a piece of Scotch tape on another glass slide and cut a ~2×2 mm^2 window from the center using a razor blade (Figure 3.7(b))
- Carefully lift the tape off the slide, avoiding tearing at the corners of the window

*After this step, I occasionally placed a small droplet of commercial PDMS mixed from a two-component kit (Dow SYLGARD 184) on top of the stamp and cured the PDMS at room temperature for 48 hours before proceeding. The curved surface resulting from this procedure helps to improve the accuracy of aligning the flakes in the heterostructure [84].

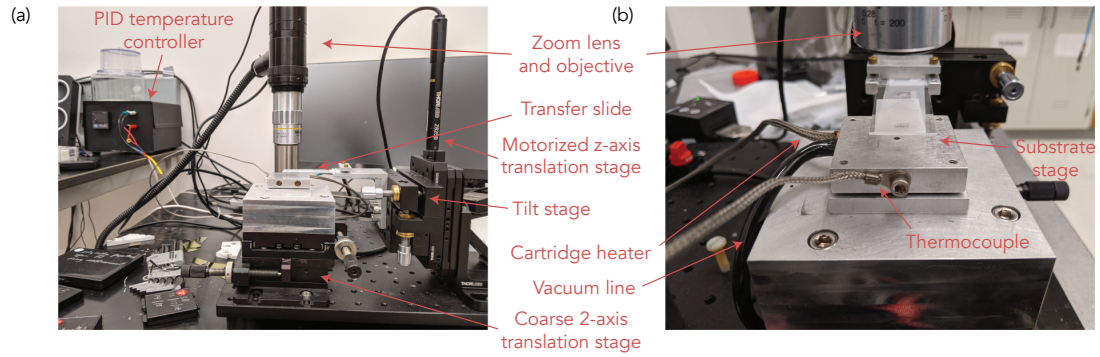

Figure 3.8: (a) Front and (b) side views of the flake transfer setup, with key components labeled.

- Overlay the tape window over a uniform region of the PC film (Figure 3.7(c)). Gently press on the back of the tape to promote adhesion.
- Make cuts in the PC film at the edges of the tape with a razor blade, and gently lift the tape/PC assembly off the glass slide. The PC film is now suspended within the tape window.
- Overlay the suspended PC film on top of the PDMS stamp and secure the free ends of the tape to the transfer slide (Figure 3.7(d)). The film should be relatively taut, but not overly stressed.
- If the tape overlaps the back side of the slide underneath the PDMS stamp, cut a window in the tape to enable optical access.

3.3.2 Heterostructure assembly

The "flake transfer setup" in Figure 3.8 facilitates the manipulation of the transfer slide to sequentially pick up flakes involved in the heterostructure. I describe some features of this setup below:

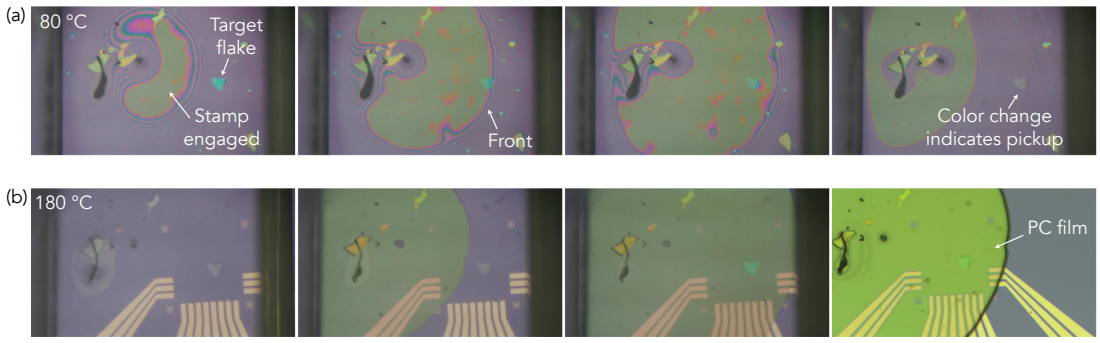

Figure 3.9: Series of microscope images demonstrating (a) pickup and (b) release of a single hBN flake.

- Heated substrate stage with a vacuum port (similar to the design described in Ref. [85]). An insulating (glass or Macor) spacer provides weak thermal isolation between the substrate stage and the underlying two-axis coarse translation stage.
- Micromanipulator for the transfer slide with motorized z-axis translation and two-axis tilt
- Zoom lens with 10× objective lens and HDMI camera for monitoring substrate/transfer slide alignment from above
- Entire assembly sits on threaded optical breadboard with vibration-isolating feet, on top of a sturdy vibration-isolated table

The general procedure for picking up the top flake of the heterostructure* is described below and illustrated for a single hBN flake in Figure 3.9(a).

- Set the substrate chuck temperature to 80 °C (for hBN pickup) or 25 °C (for MLG or FLG pickup).

*Generally, hBN is easier than FLG to pick up as the top flake. However, I was decently successful at picking up FLG directly with the PC at a stage temperature of 130 °C.

- Place the substrate with the target flake onto the substrate chuck and open the vacuum line.
- Clamp the transfer slide in the slide holder, PC film down.
- With the transfer slide far from the substrate, move the zoom lens and two translation stages to coarsely align the PC/PDMS stamp and the target flake.
- Approach the transfer slide to the substrate, checking by eye that the two do not come into contact prematurely.
- Refocus the microscope alternately on the PC film and target flake to ensure the alignment of the flake with a uniform, particle-free region of the PC film.
- Slowly engage the PC film onto the substrate, ensuring that the PC film first engages nearby, rather than directly on top of, the target flake. The interference fringes are useful for judging the proximity of the substrate and the stamp.
- Once the PC film is partially engaged, program the motorized z-axis to engage the film slowly until the PC film completely overlaps the target flake.
- Program the motorized z-axis to disengage the film slowly, until the target flake and PC film lift off of the substrate, marked by a color change of the target flake. Continue to lift the transfer slide at a quicker rate after it disengages from the substrate.

For subsequent flakes, the steps are identical, except that one must take care to align each new flake with the existing stack on the transfer slide before engaging.

Optional: rotation stage

I also built a second substrate stage on top of a motorized rotation stage that enables the precise angular alignment of flakes in the stack. This stage is intended for use at room temperature (high temperatures can damage the internal components of the stage). The angular precision is approximately $< 0.1°$, useful for the fabrication of twisted bilayer graphene devices with high angular precision. My focus was not on such devices, so I used this stage to *avoid* the formation of a Moiré superlattice between the layers in my devices [64]. I aligned the straight edges of graphene and hBN flakes manually, used the rotation stage to fine-tune the alignment, and then rotated the stage by 15° to intentionally misalign the major crystallographic axes of the flakes.

3.3.3 Heterostructure release and post-processing

With a complete heterostructure assembled on the PC/PDMS stamp, I use the following procedure to release the stack onto a final SiO_2/Si substrate. My final substrates for the completed heterostructures consist of 1×1 cm^2 chips from a low-resistivity (P/Bo, .001-.005 ohm-cm) Si wafer with 285 nm thermal oxide (Nova Electronic Materials). These substrates have pre-patterned metal contacts and alignment marks to aid with future fabrication steps (Section 3.4) and were fabricated using the process described in Appendix B.1. After the final oxygen plasma descum, I did not perform any additional cleaning steps to the substrates before transferring heterostructures. The release process is as follows and is illustrated in Figure 3.9(b).

- Place the target substrate on the chuck and heat to 180 °C.
- Slowly engage the stack as before, even more carefully than before. Upon touching the substrate, the PC film cannot be removed or repositioned without risk of damaging the heterostructure.
- When engaging the stack, ensure that bubbles trapped between the flakes are pushed towards the edges of the stack [81, 86]. A slow, controlled engagement is key to squeezing out the bubbles.
- Once the PC film is fully engaged, slowly retract the transfer slide, ensuring that the PC film remains adhered to the substrate but that the PDMS stamp and glass slide separate (be sure to have the sample vacuum on). If the PDMS stamp remains on the substrate, carefully remove it with tweezers (this will most likely not lift off the PC film).
- Gently submerge the substrate in chloroform for a minimum of 5 minutes to dissolve the PC film (4 hours to further remove residues). Rinse with a constant stream of isopropyl alcohol while removing from the solution and blow dry with nitrogen. During this step, it is possible that the heterostructure will come free of the substrate. To mitigate this, aim the stream of the isopropyl alcohol away from the location of the stack on the substrate and be gentle when submerging the stack.
- (Optional) An anneal in high vacuum ($< 10^{-6}$ Torr) for 3 h at 300 °C can effectively remove any remaining polymer residues. This process may also reorganize any bubbles trapped within the stack.

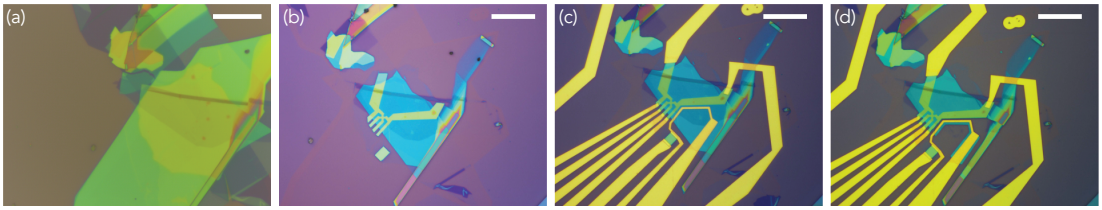

Figure 3.10: (a) Heterostructure before cleanroom fabrication. (b) Device after plasma etching. (c) Device after contact deposition. (d) Device after additional plasma etching step to remove unwanted electrical connections. Scale bars: 20 µm.

3.4 Fabrication steps for graphene devices

After assembling and releasing each heterostructure, I follow the recipe detailed in Appendix B.2 to (optionally) add a metal top gate, etch to define the device shape, and deposit metal contacts to create electrical connections between the MLG or FLG layers and the pre-patterned contacts on the substrate. These steps are based on conventional fabrication techniques involving electron-beam lithography, plasma etching, and metal evaporation. Figure 3.10 highlights several steps of the process for a FLG-gated hBN-encapsulated graphene Hall sensor. In the below sections, I describe each of the fabrication techniques involved in the process, with specific attention towards explaining process conditions leading to consistent performance of the device contacts.

3.4.1 Electron-beam lithography

To perform electron-beam (e-beam) lithography, I use a Nanometer Pattern Generation System (NPGS, JC Nabity) attached to a scanning electron microscope (SEM, Zeiss Supra 55 VP). The NPGS controls the scan coils of the SEM to raster the electron beam and expose e-beam resist in a defined pattern. This system op-

erates at lower accelerating voltage (20 kV) and exhibits a larger minimum spatial resolution (~100 nm*) compared to commercial e-beam lithography systems, but it is appropriate for the irregular geometry of the devices here and typical designed features on a length scale > 100 nm. The largest possible write field (at minimum SEM magnification) is approximately 2 mm × 2 mm, and a write field of ~400 µm × 400 µm is appropriate for most features down to ~500 nm. Manual alignment to pre-fabricated structures located near the corners of the write field enables writing patterns with ~100 nm alignment precision.

An e-beam resist mask appropriate for graphene fabrication typically consists of a spin-coated ~200 nm layer of low molecular weight poly(methyl methacrylate) (PMMA, MicroChem 495k 4 % in anisole) followed by a ~100 nm layer of high molecular weight PMMA (MicroChem 950k 2 % in MIBK). I bake the first layer for 2 min at 170 °C and the second layer for 6 min at 170 °C. This resist stack exhibits a slight undercut upon development, which promotes metal liftoff. With a 20 kV accelerating voltage, the typical dose is 300 µC cm^{-2}. Larger features benefit from larger doses (up to 500 µC cm^{-2}), which increases the resist undercut. For etch processes, I typically skip the upper PMMA layer, baking the first layer for 6 min.

It is important to adjust the beam current using the SEM aperture, according to the size and function of the features. Small features often need to be written precisely and therefore benefit from a smaller beam current (typically 200-300 pA). Larger features often simply need to connect to smaller features and the geometry is not as important, so these can be written at large beam current (typically ~1 nA). A general rule of thumb is to choose a beam current resulting

*set by the e-beam spot size; somewhat larger than the spatial resolution of imaging using the SEM

in a write time on the order of a few minutes. Writing the pattern too slowly risks drift of the sample and/or electron beam and as a consequence misplacement of features in the pattern. Moreover, the NPGS system does not have any automatic proximity effect correction, so it is important to expose features in a spiral pattern outwards from the center to mitigate proximity dosing.

Charging is not typically problematic for samples with doped silicon substrates; however, patterns written on insulating substrates require a discharging layer on top of the resist stack. DisCharge (DisChem, Inc.) works effectively for samples with polyimide substrates (see Section 6.2), not requiring any alterations to the dose or other process details.

I develop the exposed PMMA for 1 min in a 3:1 DI water:IPA mixture stored in a refrigerator, followed by rinsing in IPA and drying with nitrogen. This developer is an alternative to conventional MIBK-based PMMA developers and mitigates swelling and cracking of the resist [87]. I found that using this developer decreases the likelihood of failure of the resist mask at sharp corners, especially for structures on hBN.

3.4.2 Plasma etching

My recipe for etching in a Trion Minilock III ICP Etcher uses a $CHF_3/O_2/Ar$ inductively coupled plasma (20/10/10 sccm, 10 mTorr, 30 W ICP, 10 W RF) for selective hBN etching. Cleaning the chamber with a 10 min oxygen plasma and seasoning the chamber for 10 min with the hBN etching recipe helps to improve process repeatability; however, the etch rate still tends to vary between runs. The etch process demonstrates a selectivity of approximately 30:1

hBN:graphene and 10:1 hBN:SiO_2, with a total etch time of 1-2 min for a typical stack of thickness < 100 nm. Etching serves a dual purpose: it both shapes the device into the intended geometry and exposes a one-dimensional graphene edge that can be contacted with deposited metal [63]. Previous work suggests that selective etching reduces the contact resistance by increasing the metal-graphene contact area along the edges of the etched stack [88]. In my experience, switching to this recipe from an unoptimized CHF_3/O_2 plasma process was essential towards achieving consistent device contact quality.

I also recommend exposing the device to a gentle 1-min oxygen descum both prior to and after etching (YES CV200RFS Oxygen Plasma Asher at 200 W and 80 °C). The descum prior to etching removes PMMA residues remaining from developing the resist, and the descum afterwards removes a layer of PMMA damaged by the plasma that is difficult to remove chemically. Without the descum, this can leave behind a film-like residue on the substrate surface following resist removal.

3.4.3 Metal evaporation

I use electron-beam metal evaporation (Sharon Vacuum or Angstrom Engineering EvoVac Multi-Process thin film deposition system) to deposit edge contacts to the graphene layer or a top gate. To achieve consistently working contacts, it is often necessary to perform an oxygen descum (200 W, 80 °C, 1 min, YES Asher) after resist development and evaporate under low pressure (~10^{-7} Torr) with the sample rotating during deposition. A different evaporator I tried with typical pressure ~10^{-6} Torr and requiring pumpdown times of a few hours

could not produce reliable contacts, even with a rotating chuck.

Typically, top gates consist of 5 nm Ti/30 nm Au/10 nm Pt and edge contacts consist of either 3 nm Cr/40 nm Pd/40 nm Au or 3 nm Cr/80 nm Au. Edge contacts perform most reliably when the total metal thickness exceeds the thickness of the stack. Prior to depositing the Cr or Ti adhesion layer, I evaporate 20-30 nm Cr or Ti into the chamber with the shutter closed both to reduce the base pressure and to evaporate away naturally-formed oxides in the source crucibles.

After evaporation, I soak the samples in acetone for a few hours, until the metal and resist mask begin to lift off. Rinsing gently with a stream of acetone from a squirt bottle can help remove the metal film. I often inspect the sample optically while still submerged in acetone to ensure that liftoff is successful and continue to soak if the metal layer has not lifted off completely. I do not attempt to complete the liftoff process in an ultrasonic bath, as this may cause the stack to come free from the substrate. Finally, I rinse the samples in IPA and blow dry with nitrogen.

3.5 Sample preparation

Following fabrication, it is important to perform a cursory check of the electrical connections to the device to ensure low-resistance electrical contacts to the graphene layer and electrical isolation of the gates. This measurement can be done in an electrical probe station, but I prefer instead to mount the device directly to a chip carrier to facilitate later integration with a transport measurement setup.

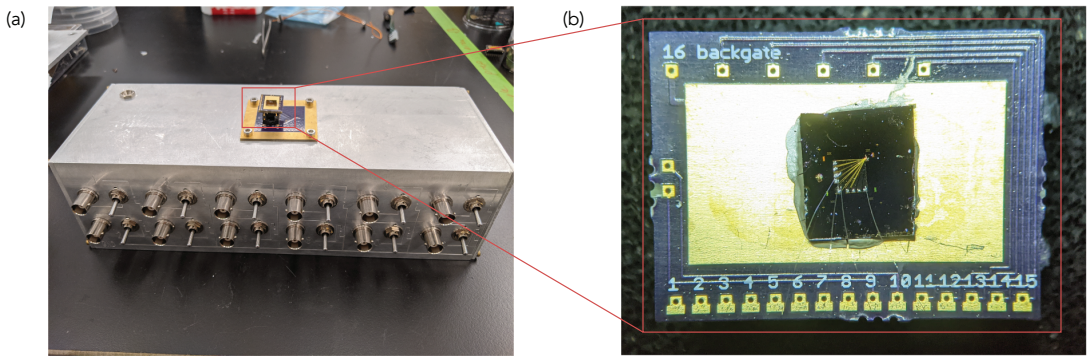

Figure 3.11: (a) Chip carrier breakout box for testing electrical connections. (b) Graphene device mounted and bonded to a chip carrier.

Figure 3.11(b) shows a finished device mounted to a custom printed circuit board (PCB) based chip carrier that connects to standard 16-pin dual-inline pin (DIP) headers on the bottom side. I use silver paste (SPI Supplies) to affix chips to the continuous metal plane on the surface of the chip carrier, ensuring that silver paste comes into contact with the edges of the sample to make an electrical connection between the sample back gate and pin 16 on the chip carrier. Nearby metal pads on the PCB connect to pins 1-15 on the DIP header and allow for wire bond connections to the sample. I attach wire bonds using a standard wedge wire bonder (WestBond 747630E) and set the power just high enough so that the wire bonds barely stick to the bond pads on the sample. Wire bonding with excessive power risks creating electrical shorts between the device contacts and back gate via breakdown of the thermal oxide on the substrate. I recommend using a custom chip carrier socket that shorts all chip carrier pins to ground and wearing a grounded wrist strap to avoid damage to the samples via electrostatic discharge.

After wire bonding, I transport the chip carrier in a conductive plastic box with conductive foam over to a transport measurement setup or custom-built breakout box (Figure 3.11(a)). When inserting the chip carrier in to the system, I

ensure that all connections are grounded and wear a grounding strap to prevent electrostatic discharge. To check electrical connections, I use a Keithley 2400 SourceMeter to source a small (~mV) voltage and monitor the current between each device pin and a common ground to estimate an Ohmic device resistance. Typical working contacts exhibit a resistance, measured in this way, of at most a few kΩ. To test gates, I apply a small voltage (~10-100 mV) using a second voltage source and monitor the leakage current between the gates and device contacts (never to exceed ~10 nA). Following these initial checks, all further characterization should be performed in high vacuum (< 1 Torr) to avoid the accumulation of stray charge impurities from the environment on the sample.

It is in principle possible to perform further fabrication steps on the devices afterwards. These steps may be necessary to remove unwanted electrical connections, make new electrical connections, or some combination of the two. There are a few caveats to keep in mind when planning additional fabrication steps:

- Remove wire bonds using metal-tipped tweezers while the sample pins are all grounded (in the same setup as before).
- Carefully pry samples off the chip carrier using a razor blade underneath
- Dissolve remaining silver paste residue in acetone, followed by an IPA rinse and nitrogen blow drying. Be careful not to agitate the acetone bath to avoid transferring silver particles to the sample surface.
- Wire bond "feet" remaining on the bond pads may interfere with e-beam resist spinning and patterning.

3.6 Conclusion

I describe the above procedures in great detail not only for the sake of completeness, but also in an effort to compile documentation that I would have found helpful when developing the techniques. Heterostructure fabrication is as much an art as it is a skill, and the possible variation between cleanroom fabrication equipment at different facilities demands careful attention towards developing procedures that produce reliable low-resistance contacts. It is my hope that the process parameters described here, especially for the etching and metal evaporation steps, will help facilitate development of processes at new facilities in the future.

CHAPTER 4

MAGNETIC FIELD DETECTION LIMITS FOR ULTRACLEAN GRAPHENE HALL SENSORS

In this Chapter, based on work published in *Nature Communications* [44], I describe in detail the application of the process described in Chapter 3 towards the fabrication of Hall-effect sensors. This work was performed in collaboration with Alexander Jarjour, Lei Wang, Paul McEuen, and Katja Nowack (Cornell), and Takashi Taniguchi and Kenji Watanabe (National Institute for Materials Science, Japan). I also acknowledge Menyoung Lee for useful discussions, Jeevak Parpia for contributing equipment for the low-temperature measurements, and the technical support of Greg Stiehl, Ruofan Li, Boyan Penkov, Vincent Genova, Jeremy Clark, and Eric Smith.

Here I establish ultraclean graphene as an excellent material platform for micrometer-scale Hall sensors and demonstrate device performance matching or exceeding the performance of all other Hall sensors reported in the literature. Specifically, electrically tuning the devices controls the magnetic field detection limit, describing the smallest detectable change in magnetic field for a chosen measurement bandwidth. Control over the experimental knobs of bias current and gate voltage enables optimization of this detection limit under different experimental conditions, including low temperature, room temperature, and at high background magnetic field at which the sensors exhibit the quantum Hall effect. The results discussed here motivate the use of ultraclean graphene Hall sensors both as on-chip sensors directly incorporated with a material of interest as well as scanning probes (see Section 2.4.2).

4.1 Introduction

The main figure of merit for any magnetic field sensor is the magnetic field detection limit $S_B^{1/2}$. This quantity, multiplied by the square root of the measurement bandwidth, gives the smallest detectable change in magnetic field. Recalling from Section 2.2, the magnetic field detection limit for a Hall sensor is $S_B^{1/2} = S_V^{1/2}/(IR_{\mathrm{H}})$, where $S_V^{1/2}$ is the Hall voltage noise, I is the bias current, and $R_{\mathrm{H}} = I^{-1}(\partial V_{\mathrm{H}}/\partial B)$ is the Hall coefficient, describing the change in current-normalized Hall voltage per unit change in magnetic field. The desire to minimize the detection limit motivates an ideal material system combining low carrier density for a large Hall coefficient and high carrier mobility for low device resistance, aiming to minimize the contributions from possible voltage noise sources (see Section 2.3) [46]. Whereas carrier mobility decreases at low carrier density in most semiconductor-based two-dimensional electron systems [72], in graphene the mobility is enhanced at low carrier density in the absence of long-range impurity scattering [89]. Encapsulation in hexagonal boron nitride (hBN) [63] and more recently few-layer graphite (FLG) [64,69,70] enables access of this low-density, high-mobility regime. Indeed, hBN-encapsulated graphene is a promising material platform for Hall sensors with low $1/f$ noise in micrometer-scale devices [90] leading to low magnetic field detection limits [45] at room temperature.

Here, I discuss Hall sensors fabricated from hBN-encapsulated monolayer graphene (MLG) with either Ti/Au metal or FLG gate electrodes. Tuning the carrier density via electrostatic gating enables optimization of the magnetic field detection limit under different operating conditions. I thereby demonstrate that ultraclean graphene is a promising material system for high-performing Hall

sensors, obtaining performance matching or exceeding that of every other reported Hall sensor material system in the literature.

4.2 Device overview

My Hall sensors consist of hBN-encapsulated monolayer graphene (MLG) with either Ti/Au metal or FLG gate electrodes. Figure 4.1(a) shows the structure and optical image of a typical graphite-gated device (see Section 4.4.4 for discussion of additional devices). I fabricated each device from a heterostructure with typical layer structure hBN/FLG/hBN/MLG/hBN/FLG/SiO_2/Si using the techniques described in Chapter 3. The combination of low charged defect density in hBN and the ability of FLG to screen charged impurity disorder in the silicon substrate improves carrier mobility [63, 91], reduces the charge inhomogeneity [69, 70], and can reduce charge noise in graphene devices [90]. The top gate tunes the carrier density in the active region of the device, while the grounded bottom gate screens the electric field from the silicon back gate. The silicon back gate, set to 40 V, induces a high electron density in the graphene-based portion of the leads. This lowers the resistance of the leads and edge contacts [64], consequently lowering the voltage noise (see Section 4.4.4).

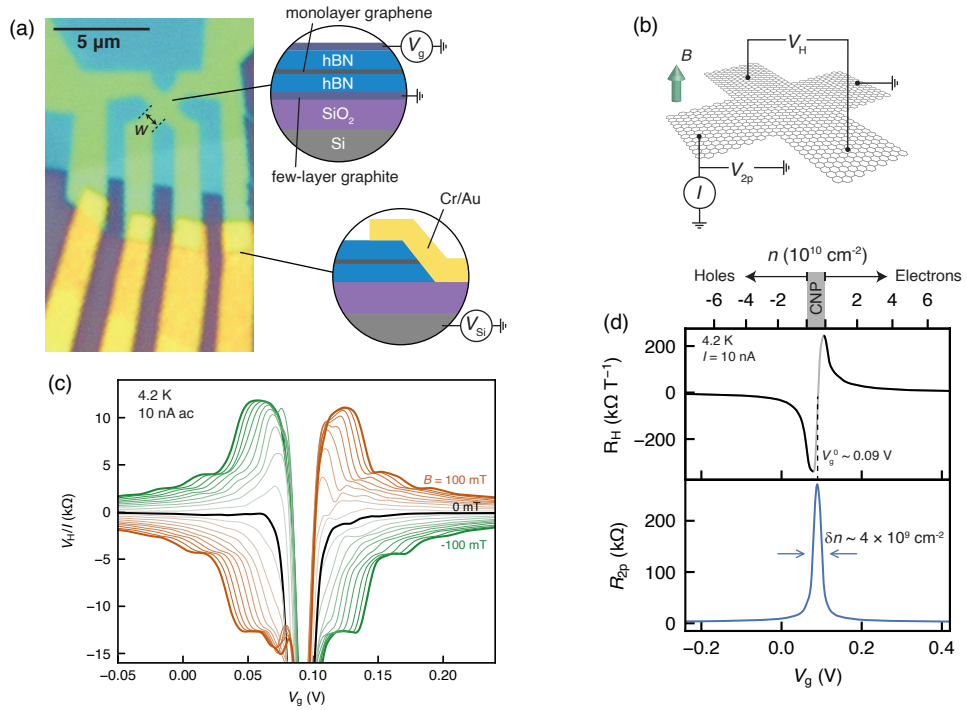

Figure 4.1: (a) Optical microscope image of device G1 (w = 1 μm). Top cross-section: Hall cross layer structure. Bottom cross-section: edge contacts. (b) Schematic of the measurement configuration, with Hall voltage V_{H}, two-point voltage $V_{2\mathrm{p}}$, bias current I, and out-of-plane magnetic field B. (c) Top gate voltage (V_{g}) dependence of the Hall resistance V_{H}/I at a series of magnetic fields (step size: 10 mT). (d) Top panel: Hall coefficient R_{H} calculated from (c). The upper axis indicates the corresponding electron and hole densities. Bottom panel: Two-point resistance $R_{2\mathrm{p}}$ obtained simultaneously.

4.3 Voltage response

Using the measurement configuration shown schematically in Figure 4.1(a,b), I measured the Hall voltage V_{H} and two-point voltage $V_{2\mathrm{p}}$ under various conditions of bias current I, top gate voltage V_{g}, and magnetic field B. The following sections describe measurements under ac and dc bias performed at 4.2 K in a liquid-helium cryostat with a low background magnetic field not exceeding 100 mT.

4.3.1 Small ac bias

I first applied small ac bias and used a lock-in amplifier (Zurich Instruments MFLI or HF2LI) at 17.777 Hz to evaluate the electronic quality of each device. I connected the lock-in voltage output to the device with a large series bias resistor (~1 MΩ) to generate a bias current that is approximately constant when the two-point device resistance is small compared to the bias resistance. I monitored the drain current using the same lock-in and measured the two-point and Hall voltages simultaneously using a separate synchronized two-channel lock-in.

Sweeping V_g tunes the carrier density n, changing the Hall voltage approximately as $V_H = IB/(ne)$ at fixed magnetic field. A series of gate sweeps at fixed magnetic field up to 100 mT (Figure 4.1(c)) reveals quantum Hall resistance plateaus developing at magnetic fields as low as ~40 mT. The appearance of well-defined quantum Hall resistance plateaus at low magnetic fields is a clear signature of small charge inhomogeneity in these high-quality graphene devices [83]. For each V_g, I performed a linear fit to V_H vs. B to obtain the Hall coefficient $R_H = I^{-1}(\partial V_H/\partial B)_{B=0}$ and corresponding carrier density $n = 1/(eR_H)$ (Figure 4.1(d), upper panel) as a function of V_g. At gate voltages near the charge neutrality point (CNP, grey portion of the curve), the coexistence of electrons and holes makes V_H nonlinear in B [92]. Elsewhere, the Hall voltage is linear in B at least up to 100 mT, and $R_H \propto n^{-1} \propto V_g^{-1}$ assuming a simple capacitive coupling of the gate to the mobile carrier density [89].

The maximum (minimum) value of R_H for electron (hole) doping $240\,\mathrm{k\Omega\,T^{-1}}$ ($-340\,\mathrm{k\Omega\,T^{-1}}$) implies a smallest mobile carrier density $\delta n \sim 2.6\times10^{9}\,\mathrm{cm^{-2}}$ ($-1.8\times10^{9}\,\mathrm{cm^{-2}}$) limited by intrinsic charge inhomogeneity. Also, the width of the sharp peak in the two-point resistance $R_{2p} = V_{2p}/I$ (Figure 4.1(d), lower

panel) implies a charge inhomogeneity $\sim 4 \times 10^9\,\mathrm{cm}^{-2}$ considering both electrons and holes. This low charge inhomogeneity is consistent with that reported in other devices with atomically smooth single-crystal graphite gate electrodes [69,70]. The magnitude of R_{2p} exceeds 200 kΩ at the CNP, decreasing to a few kΩ for moderate doping, with major contributions from the resistance of the graphene channel (~1 kΩ) and edge contacts (~1-2 kΩ).

Applying the relationship $n = 1/(eR_H)$ independently for electron and hole doping and extrapolating n to zero reveals that electrons and holes appear to reach charge neutrality at different V_g (see Figure 4.1(d), upper axis). This is consistent with non-constant contributions to the charging behavior of the graphene sheet from the quantum capacitance and/or charge traps, which become significant because of the large gate capacitance and small charge inhomogeneity [89,93,94]. I discuss these contributions in Appendix C.1.

4.3.2 Large dc bias

Next, I characterized the Hall voltage as a function of applied dc current bias up to 50 μA. Instead of a lock-in amplifier, I used a dc voltage source (Keithley 2400 SourceMeter) again with a ~1 MΩ bias resistor. I set the current limit on the voltage source to the desired bias current and increased the voltage until the current saturated. I used a low-noise preamplifier (Signal Recovery 5113) in dc coupling mode to amplify and filter the Hall voltage signal, and I sampled the signal using the input terminal of a lock-in amplifier (Zurich Instruments MFLI).

The Hall voltage response to a small change in magnetic field δB is

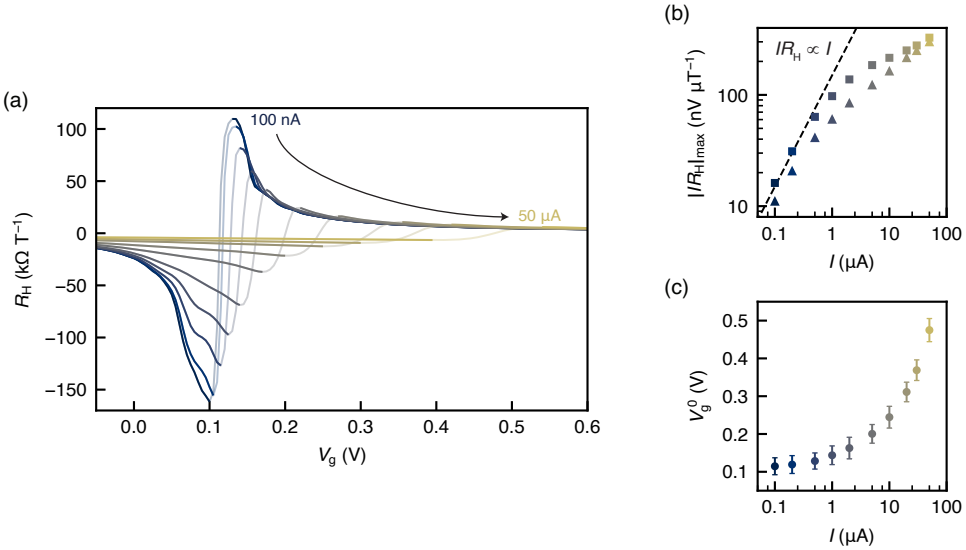

Figure 4.2: (a) Hall coefficient R_H for device G1 under varying dc current bias at 4.2 K. (b) Bias current dependence of the peak value of IR_H. (c) Bias current dependence of the charge neutrality point voltage V_g^0. Error bars represent the uncertainty in determining the point at which R_H crosses zero.

$\delta V_H = IR_H \delta B$, suggesting that applying a larger bias current in principle proportionally increases the voltage signal. In practice, a large dc bias causes two changes in the transport characteristics of the devices (Figure 4.2): a decrease of the peak R_H and a shift of the CNP voltage offset V_g^0. The direction in which V_g^0 shifts depends on the polarity of the applied current. The changes in the Hall voltage curve under large dc bias are consistent with a potential gradient and resulting carrier density gradient across the device [93]. This modifies the average R_H within the Hall cross and limits its peak value. Appendix C.2 explores this phenomenon further. Despite the reduction in peak R_H, applying larger bias current still increases the absolute voltage sensitivity $IR_H = (\partial V_H/\partial B)_{B=0}$ (Fig. 3b), giving a larger change in Hall voltage per unit change in magnetic field.

4.4 Voltage noise and magnetic field detection limit

Having established a conversion between magnetic field and voltage via the Hall coefficient, I then measured the Hall voltage noise spectral density $S_V^{1/2}$ to estimate an equivalent magnetic field detection limit $S_B^{1/2} = S_V^{1/2}/(IR_{\mathrm{H}})$. This quantity represents the smallest detectable change in magnetic field strength divided by the square root of the measurement bandwidth.

I again used a dc voltage source (Keithley 2400 SourceMeter) in series with a ~1 MΩ resistor to apply bias current and measure the noise using a low-noise preamplifier (Signal Recovery 5113) connected to the input terminal of a lock-in amplifier (Zurich Instruments MFLI). The preamplifier has an input noise of ~7 nV Hz$^{-1/2}$ and is set to ac coupling mode with a 10 kHz lowpass filter and typical gain of 500 for noise measurements. For each bias current and gate voltage, I recorded 30 time traces sampled at 3.66 kHz for ~4.5 s each, giving 2^{14} sampled voltage values per time trace (Figure 4.3(a)). I then computed the Fourier transform of each time trace via Welch's method with a Hann window, using frequency bins with 50% overlap consisting of 27 points to reduce variance [95]. The resulting power spectral density S_V is valid in a frequency band spanning ~1 Hz to ~3.66 kHz. The square root of the power spectral density, $S_V^{1/2}$ is the Hall voltage noise spectral density (Figure 4.3(b)). To compare spectra across different experimental conditions (gate voltage, current bias, etc.), I summarize the noise by taking the root-mean-square average and standard deviation of points within a 200 Hz band centered at 1 kHz.

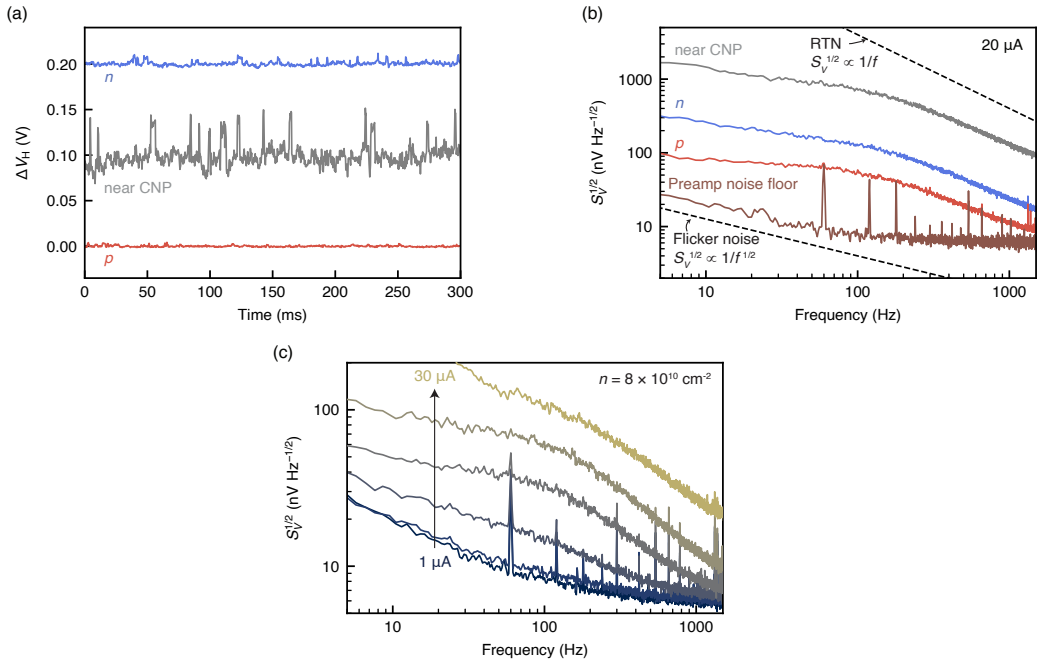

Figure 4.3: (a) Time traces of the Hall voltage (offset for clarity) and (b) Hall voltage noise spectral density $S_V^{1/2}$ for device G1 at 4.2 K. (c) Comparison of $S_V^{1/2}$ spectra at different bias currents. For each bias current, V_g is tuned such that $R_H \approx 7.8\,\mathrm{k\Omega\,T^{-1}}$, corresponding to $n \approx 8 \times 10^{10}\,\mathrm{cm^{-2}}$.

4.4.1 Flicker and random telegraph noise

Figure 4.3(c) shows how the noise spectrum changes with bias current. At low bias, 60 Hz and preamplifier input noise dominate the $S_V^{1/2}$ spectrum. With increasing bias current, the shape of the noise spectrum suggests the presence of both flicker ($1/f$) noise and random telegraph noise (RTN) (see Section 2.3). These two noise contributions are common to both micrometer-scale Hall sensors [45, 46, 48] and graphene-based devices [58, 90, 96], and they clearly dominate the noise spectrum, overshadowing possible white Johnson noise*. While $1/f$ noise originates most likely from random charging and discharging events

*The Johnson noise floor is at most ~10 $\mathrm{nV\,Hz^{-1/2}}$ for a maximum R_{2p} of ~250 kΩ at 4.2 K and ~18 $\mathrm{nV\,Hz^{-1/2}}$ for a maximum R_{2p} of ~20 kΩ at room temperature (see Section 4.4.3).

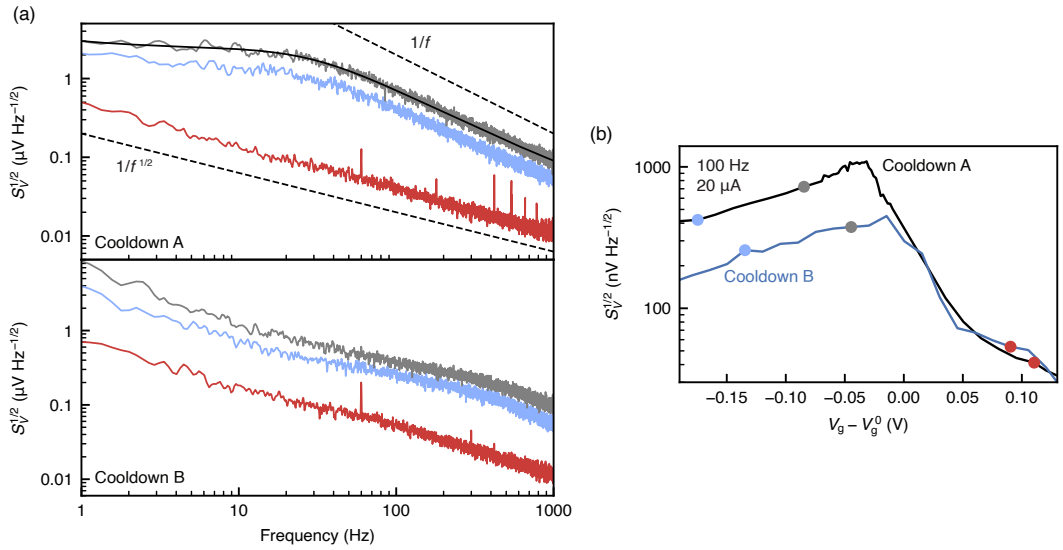

Figure 4.4: (a) $S_V^{1/2}$ spectra for device G1 measured during separate cooldowns. The black curve is a fit to the combined noise model discussed in Section 2.3.4 assuming small Johnson noise, with fixed $\alpha = 1$ and best-fit parameters $\delta V = 52.5 \pm 0.5\,\mu\text{V}$, $\tau_1 = 6.09 \pm 0.09\,\text{ms}$, $\tau_2 = 49.0 \pm 0.9\,\text{ms}$, and $A = 3.1 \pm 0.3\,\text{pV}$. (b) Comparison of average $S_V^{1/2}$ at 100 Hz for the two cooldowns, with circles marking the gate voltages for the spectra in (a).

of an ensemble of charge traps, RTN is characteristic of a single charge trap more strongly coupled to the device. These charging events can induce fluctuations in both the carrier mobility and carrier density which are prominent in graphene-based devices at low carrier density [46, 48, 58, 96]. Charge fluctuations that modulate the contact resistance and defect states in the substrate or etched edges of the device can couple strongly into the voltage noise, especially near charge neutrality where charge fluctuations are poorly screened [58, 96].

The RTN behavior tends to change between successive cooldowns and under different conditions of current bias and gate voltage. For example, in one cooldown (Figure 4.4(a), lower panel) $S_V^{1/2}$ is clearly dominated by a linear $1/f$-like noise spectrum, while in a separate cooldown (upper panel), $S_V^{1/2}$ flattens at low frequency and falls off as f^{-1} at high frequency, characteristic of a

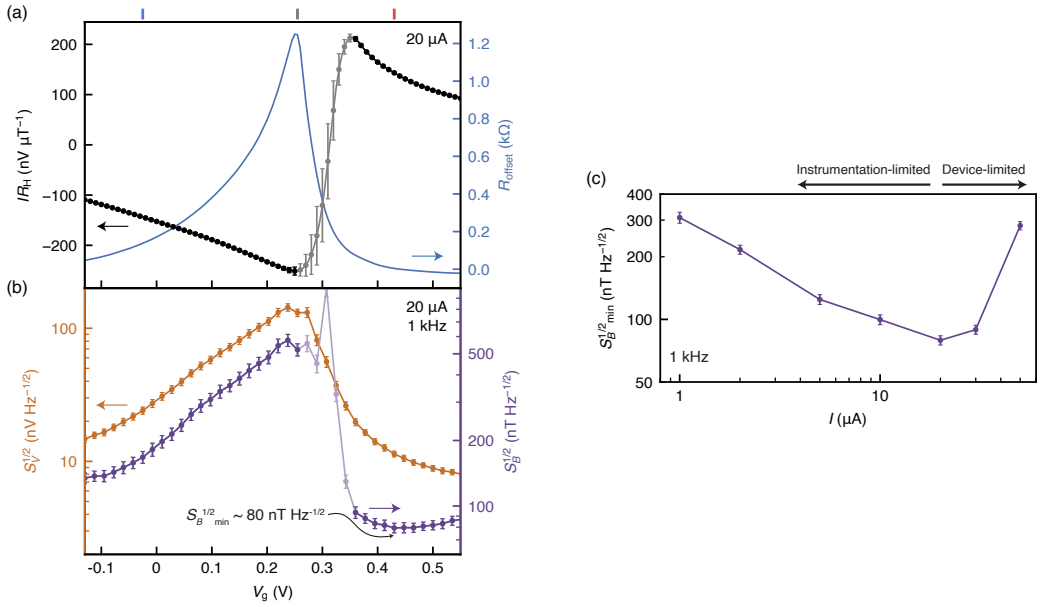

Figure 4.5: (a) IR_H and $R_{offset} = V_H(B = 0)/I$ for 20 μA bias current. The ticks above the panel correspond to the three curves in Figure 4.3. The error bars here are proportional to the standard error of the linear fit for R_H. (b) $S_V^{1/2}$ and magnetic field detection limit $S_B^{1/2}$ at 1 kHz. (c) Bias current dependence of the minimum $S_B^{1/2}$ at 1 kHz.

Lorentzian RTN spectrum [52].

4.4.2 Detection limit at low temperature

Figure 4.5(b) summarizes the low-temperature gate voltage dependence of $S_V^{1/2}$ at zero B and corresponding magnetic field detection limit $S_B^{1/2} = S_V^{1/2}/(IR_H)$ at 20 μA current bias and 1 kHz. I choose to analyze $S_V^{1/2}$ at this frequency to clarify its dependence on gate voltage; the frequency is low enough that the voltage noise surpasses the instrumentation noise floor, but high enough that the less generic contribution from RTN is small. The shape and asymmetry of the curve in Figure 4.5(b) is similar to that of the offset resistance at zero

background magnetic field $R_{\text{offset}} = V_{\text{H}}(B = 0)/I$ (Figure 4.5(a)). This offset most likely arises in this case from inhomogeneous current flow at doping levels near charge neutrality and has the effect of coupling in additional $1/f$ noise contributions associated with the longitudinal resistance [46,48].

Figure 4.5(c) shows that a 20 µA bias current minimizes the magnetic field detection limit. At this intermediate bias current, the increase in the voltage signal above the instrumentation noise floor is favorable over the reduction of R_{H} at large bias current. Notably, the minimum $S_B^{1/2}$ does not occur at the same value of V_{g} that maximizes R_{H}. This indicates that the optimum working point of the Hall sensor balances tuning away from the CNP to reduce $S_V^{1/2}$ and tuning close to the CNP to increase R_{H}. The minimum value, $S_B^{1/2} \sim 80\,\text{nT}\,\text{Hz}^{-1/2}$ at 1 kHz (lowermost point in Fig. 1), is the smallest magnetic field detection limit ever reported in a micrometer-scale Hall sensor at 4.2 K.

4.4.3 Performance at increasing temperature

The high performance of the sensors discussed so far is primarily a result of the low intrinsic charge inhomogeneity in the devices (Figure 4.1(d)), and $R_{\text{H}}^{\text{max}}$ is constant at low temperature (Figure 4.6(b)). Upon increasing the temperature T, thermal excitation of charge carriers and acoustic phonon scattering increase the charge inhomogeneity, limit the carrier mobility, and effectively decrease $R_{\text{H}}^{\text{max}}$ (Figure 4.6(a)) [63,97,98]. The total temperature-dependent effective charge inhomogeneity is often modeled as

$$\delta n(T) = \frac{1}{2\pi(\hbar v_{\text{F}})^2}\left[\Delta^2 + \frac{\pi^2}{3}(k_B T)^2\right], \tag{4.1}$$

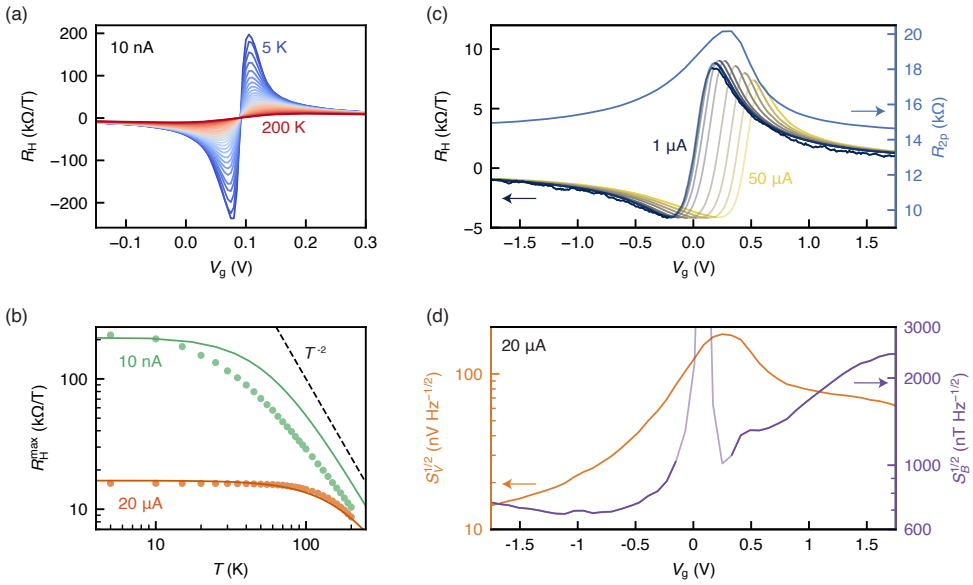

Figure 4.6: (a)-(b) R_H as a function of gate voltage and temperature, estimated from measurements of V_H at $B = \pm 50$ mT in a Quantum Design Physical Property Measurement System. Solid curves are fits to Equation 4.1 with $\Delta = 9$ meV (10 nA) and $\Delta = 32$ meV (20 μA). (c) R_H and R_{2p} at room temperature for 20 μA bias. (d) $S_V^{1/2}$ and $S_B^{1/2}$ at room temperature.

where $v_F = 10^6\,\mathrm{m\,s^{-1}}$ is the Fermi velocity and Δ is the amplitude of potential fluctuations due to charge disorder [97]. This model describes the temperature-dependent behavior in Figure 4.6(b) well, capturing a transition to a common T^{-2} dependence at high temperature for both low and high bias current. Thermal contributions to charge inhomogeneity are therefore dominant at room temperature even for high bias current, and the change in the R_H curve upon increasing bias current is less drastic than at low temperature (Figure 4.6(c)).

A full characterization of the noise at room temperature* (Figure 4.6(d)) reveals a similar dependence of $S_V^{1/2}$ and $S_B^{1/2}$ on gate voltage as at low tempera-

*For room temperature characterization, I used the same cryostat insert and wiring as for low-temperature measurements, with the insert positioned between the poles of a C-frame electromagnet (GMW Associates, model 5403).

		w (μm)	δn (cm^{-2})	min $S_B^{1/2}$ ($\mathrm{nT\,Hz}^{-1/2}$)	min $S_B^{1/2} w$ ($\mu\mathrm{m\,nT\,Hz}^{-1/2}$)
Graphite-gated	G1	1	$\sim 4 \times 10^9$	80	80
	G2	0.5	$\sim 10^{10}$	150	75
	G3	0.5	$\sim 10^{10}$	200	100
Metal-gated	M1	1	$\sim 10^{10}$	250	250
	M2	2	$\sim 10^{10}$	100	200

Table 4.1: Summary of the performance of additional devices at 4.2 K. δn is estimated from the R_{H} extrema and the width of the $R_{2\mathrm{p}}$ peak.

ture. The minimum $S_B^{1/2} \sim 700\,\mathrm{nT\,Hz}^{-1/2}$ is somewhat larger than that measured at low temperature, but still competitive with but still competitive with the best Hall sensors reported in the literature (see Section 4.6).

4.4.4 Summary of additional devices

Table 4.1 and Figure 4.7 summarize the performance of additional devices. Each device structure either consists of top and bottom few-layer graphite gates (G1, G2, G3, Figure 4.7(b)) or a single top metal gate (M1, M2, Figure 4.7(c)) fabricated as described in Appendix B.2. The charge inhomogeneity $\delta n \sim 10^{10}\,\mathrm{cm}^{-2}$ in devices other than G1 is comparable to that reported previously in hBN-encapsulated graphene devices [63, 91], contrary to the naive expectation that all graphite-gated devices should have a smaller δn [69, 70]. It is likely here that the small lateral size of G2 and G3 sets an upper bound for the Fermi wavelength λ_{F} leading to poor screening of charge disorder [89, 99]. Indeed,

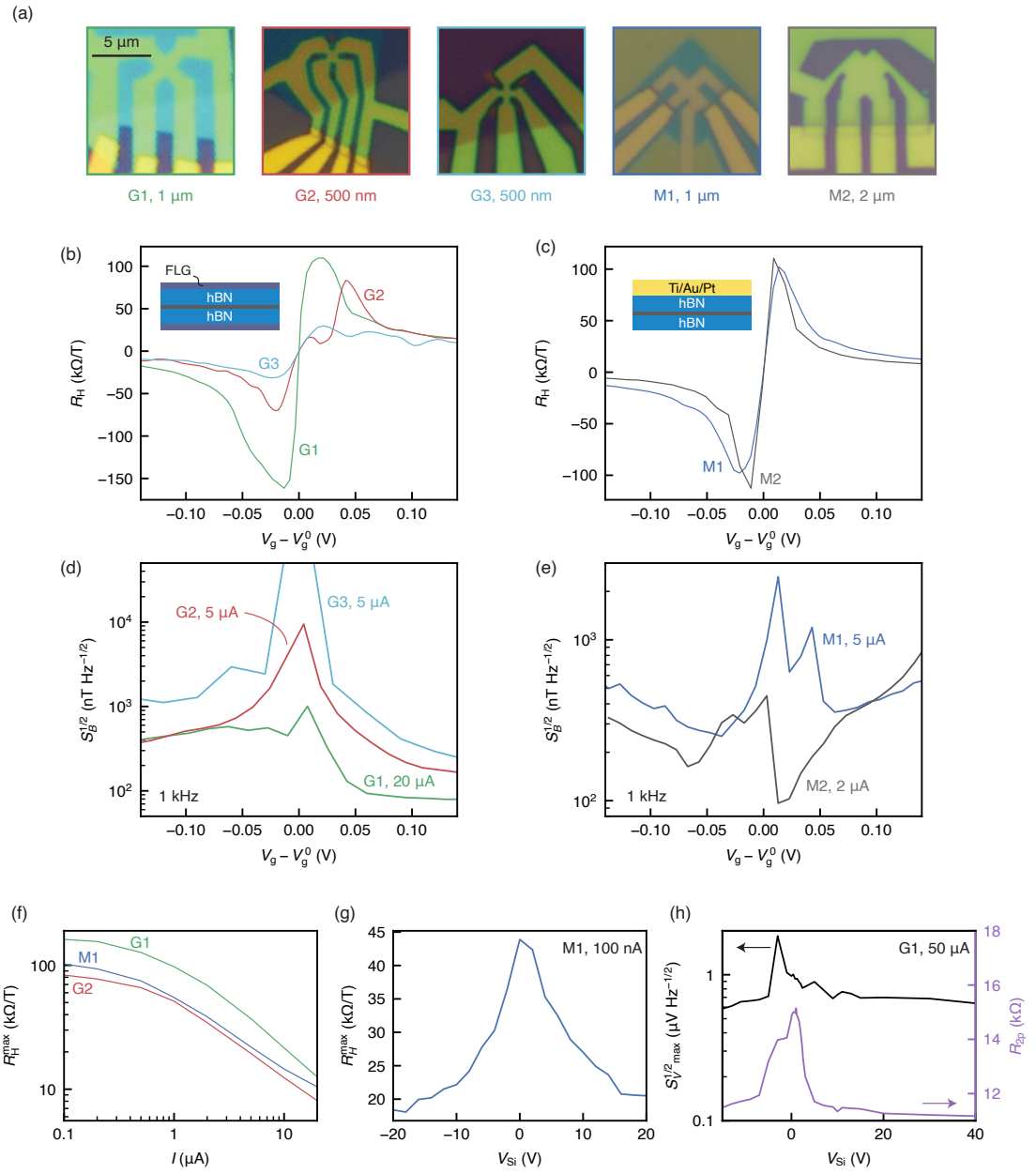

Figure 4.7: (a) Optical images of the devices summarized in Table 4.1 with indicated Hall cross width w. (b)-(c) R_{H} for 100 nA DC bias at 4.2 K. Insets: schematic device structure. (d)-(e) $S_B^{1/2}$ at 1 kHz and 4.2 K, shown for the current that yields the minimum $S_B^{1/2}$ for each device. (f) Dependence of $R_{\mathrm{H}}^{\mathrm{max}}$ on current bias. (g) Reduction in $R_{\mathrm{H}}^{\mathrm{max}}$ upon applying voltage to the silicon gate of M1. (h) Reduction of dc two-point resistance and peak voltage noise at 1 kHz upon applying silicon gate voltage to G1.

assuming $\lambda_F = 0.5\,\mu m$ suggests an effective minimum charge inhomogeneity $\delta n = \frac{2}{\pi}\left(\frac{2\pi}{\lambda_F}\right)^2 \approx 10^{10}\,cm^{-2}$, in agreement with our measurements.

The potential and carrier density gradients at high current bias (see Figure C.2) have a similar effect on the R_H curves for both graphite- and metal-gated devices (Figure 4.7(f)). However, the devices do not perform equivalently at high current bias; device G1 still demonstrates the highest R_H^{max} and smallest detection limit, a result of the smaller charge inhomogeneity.

Applying voltage to the silicon gate inhibits the performance of metal-gated devices, but improves the performance of graphite-gated devices. The grounded bottom graphite gate in device G1 enables doping of the contacts with the silicon gate without affecting the Hall cross, reducing the two-point resistance and voltage noise without decreasing R_H^{max} (Figure 4.7(h)). However, applying silicon gate voltage to M1 can actually decrease R_H^{max} (Figure 4.7(g)), suggesting that the silicon gate effectively increases the charge inhomogeneity in the Hall cross.

4.5 Performance in large background magnetic field

Finally, I return to device G1 to characterize the detection limit for small changes in magnetic field in the presence of a large background magnetic field. Hall sensors based on high-mobility two-dimensional conductors are not typically compatible with high background magnetic fields because these sensors exhibit the quantum Hall effect (QHE). The QHE creates wide regions of parameter space in which the Hall voltage is constant either as a function of magnetic field or carrier density. Specifically, the Hall resistance (Figure 4.8(a)) develops

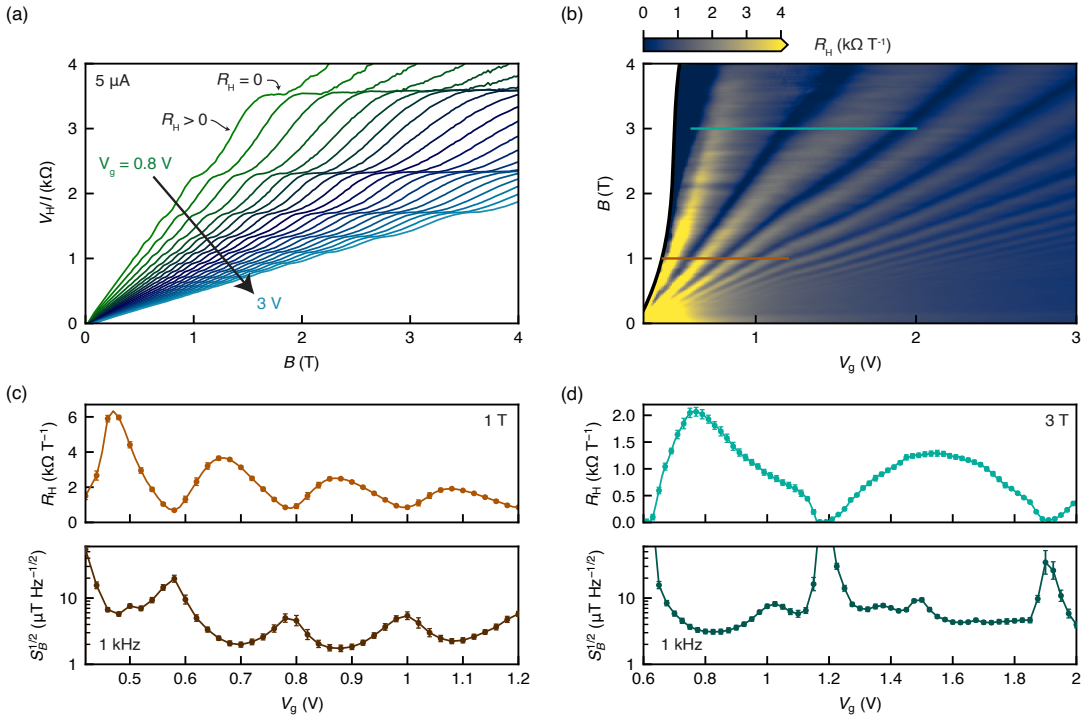

Figure 4.8: (a) Magnetic field dependence of V_H/I in the quantum Hall regime for device G1 at 4.2 K. The curves span gate voltages corresponding to electron density 0.24-1.14 $\times 10^{12}$ cm^{-2} at zero field. (b) R_H determined locally at each point (V_g, B). (c), (d) R_H and $S_B^{1/2}$ at 1 kHz along the horizontal lines in (b): (c) $B = 1$ T, (d) 3 T. Error bars are determined considering the standard error of the linear fit for R_H and the standard deviation of $S_V^{1/2}$ in a window of width 200 Hz centered at 1 kHz. All measurements are performed under 5 μA dc current bias.

plateaus spaced by $\Delta(V_H/I)^{-1} = 4e^2/h$ as expected for MLG in the quantum Hall regime [89]. The deviation of the resistance plateaus from precise quantization is caused by the large bias current and wide, extended Hall voltage contacts in the device (see Figure 4.1(a)), which mix a significant fraction of the longitudinal resistance into the Hall resistance [100].

I computed the local Hall coefficient $R_H = I^{-1}(\partial V_H/\partial B)$ over a grid of (V_g, B) coordinates to obtain the fan diagram in Figure 4.8(b). The dark regions in this diagram correspond to values of B and V_g at which V_H exhibits a plateau,

giving essentially zero sensitivity to B. Tuning the gate voltage such that the device simultaneously exhibits large R_{H} and small $S_V^{1/2}$ results in an optimum $S_B^{1/2}$ (Figure 4.8(c)-(d)). In this way, the devices can achieve a low magnetic field detection limit at high background magnetic field despite the presence of the QHE. Device G1 exhibits $S_B^{1/2} \sim 3\,\mu\mathrm{T\,Hz^{-1/2}}$ at 1 kHz and optimum carrier density tuning ($V_{\mathrm{g}} \sim 0.8\,\mathrm{V}$) under 3 T background field (Figure 4.8(d)).

At low temperature and large background magnetic field, device G1 maintains a detection limit of ~2-3 $\mu\mathrm{T\,Hz^{-1/2}}$ at 1 kHz. The larger detection limit compared to measurements at zero field is a result of both the reduced R_{H} and a general increase in voltage noise in large background magnetic field. The increase in voltage noise is likely correlated with large longitudinal magnetoresistance and may also be attributed to charge fluctuations between localized and extended quantum Hall states [101, 102].

4.6 Comparison to other materials

Table 4.6 compiles performance benchmarks for a variety of high-performing micrometer-scale Hall sensors based on graphene or other two-dimensional conductors. I plot these benchmarks alongside those for my own devices (black and red markers) in Figure 4.9. For the sake of establishing the most valid possible comparison to the devices discussed above, I choose to evaluate the detection limit for each device at 1 kHz at which $1/f$ noise is likely the dominant noise component. I also normalize the detection limit by the device size w, using the metric $S_B^{1/2}w$ to compare the performance of Hall sensors across materials [45]. The choice of this metric follows from the typical approximate scaling

Material (label)	w (μm)	$S_B^{1/2}$ (nT Hz$^{-1/2}$)	$S_B^{1/2}w$ (μm nT Hz$^{-1/2}$)	T (K)
Epitaxial graphene (G/SiC)* [103]	0.5	(79500, 101000)	(40000, 50500)	300 K
	5	(6300, 8000)	(31500, 40000)	300 K
	10	(4000, 5100)	(40300, 51000)	300 K
CVD graphene (G)† [49]	1.5	10000	15000	300 K
	1.5	4000	6000	4 K
CVD graphene (G)* [48]	0.085	(40400, 46000)	(3400, 3900)	300 K
	1	(4100, 4700)	(4100, 4700)	300 K
hBN/G/hBN (hBN) [45]	3	175	(525, 875)	300 K
GaAs [104]	0.8	25000	20000	300 K
	2	6000	12000	300 K
	10	1700	17000	300 K
	20	700	14000	300 K
	40	200	8000	300 K
GaAs* [46]	0.35	(1300, 2000)	(440, 700)	4 K
InGaAs [105]	1.5	800	1200	300 K
InSb [37]	0.6	12000	7200	300 K
InSb [50]	1.5	600	800	300 K
InAsSb‡ [106]	–	58	–	300 K
Si [104]	5	1000	5000	300 K
	10	1000	10000	300 K
	20	470	9400	300 K
Bi [47]	0.05	80000	4000	300 K

Table 4.2: Lateral size w and magnetic field detection limit $S_B^{1/2}$ at 1 kHz for Hall sensors reported in the literature. Entries expressed as a pair of numbers are estimates of lower and upper bounds.
* $S_B^{1/2}$ extrapolated to 1 kHz assuming $1/f$ noise scales as $f^{-\alpha}$ ($0.4 < \alpha < 0.6$).
† Width inferred from optical image.
‡ Ref. [106] does not clearly state the size of the device for which the detection limit is reported, so I do not include this work in Figure 4.9. Although the authors show an image of a device with $w = 1\,\mu$m, the reported carrier density and carrier mobility suggest a series resistance a factor of 10 larger than the resistance stated for the device exhibiting the reported detection limit.

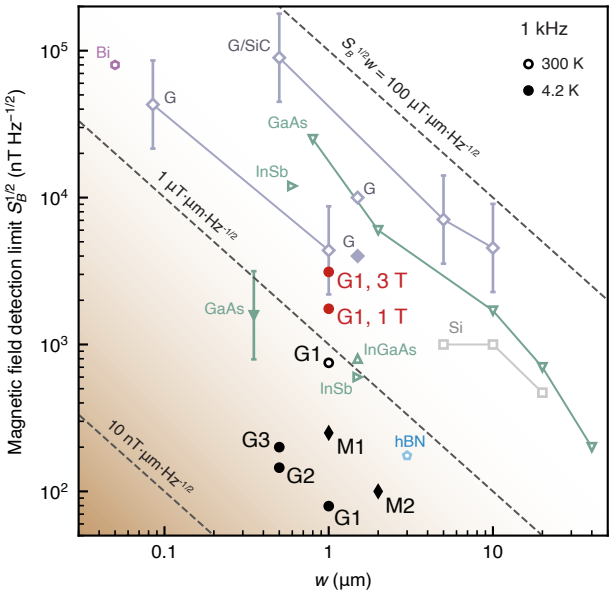

Figure 4.9: Minimum magnetic field detection limit $S_B^{1/2}$ at 1 kHz vs. the width w of Hall sensors reported here and in the literature. Filled black circles: graphite-gated devices G1-G3 at low temperature. Open black circle: G1 at room temperature. Filled red circles: graphite-gated devices at low temperature and high magnetic field as indicated. Black diamonds: metal-gated devices M1 and M2. The other markers estimate the performance of Hall sensors made from other materials at 4.2 K (filled) and 300 K (open) and zero background field. Solid lines are a guide to the eye connecting markers corresponding to the same material and fabrication process. Dashed lines mark constant $S_B^{1/2}w$. Error bars indicate the extent of the ranges estimated in Table 4.6.

of $S_B^{1/2} \propto A^{-1/2} \propto w^{-1}$ when the noise spectrum is dominated by $1/f$ noise (see Section 2.3). According to $S_B^{1/2}w$, devices with similar performance lie along the dashed diagonal lines in Figure 4.9, with the best-performing devices located towards the lower left corner of the plot.

At room temperature, the performance of device G1 is similar to that of the best sensors made from InGaAs [105], InSb [50], and hBN-encapsulated graphene [45]. At low temperature (4.2 K), the detection limit of device G1 decreases by an order of magnitude, reaching the smallest values of $S_B^{1/2}$ and $S_B^{1/2}w$ reported for any Hall sensor to date. Even when subjected to a large background

magnetic field of up to 3 T, the detection limit of device G1 still remains comparable to that of many high-performing Hall sensors tested at zero magnetic field. Additional graphite-gated devices (G2 and G3) show performance consistent with an approximate w^{-1} scaling of the detection limit, while metal-gated devices exhibit somewhat larger detection limits (see Table 4.1).

4.7 Discussion and outlook

It is insightful to compare the performance of ultraclean graphene Hall sensors to that of SQUID magnetometers. A typical magnetic field detection limit for planar niobium-based SQUIDs at kHz frequencies is $S_B^{1/2} \sim 1\,\mu\Phi_0\,\mathrm{Hz}^{-1/2}$, or $S_B^{1/2} \sim 40\,\mathrm{nT\,Hz}^{-1/2}$ for a circular sensitive area with a 0.25 µm diameter and $S_B^{1/2} \sim 3\,\mathrm{nT\,Hz}^{-1/2}$ for a 1 µm diameter (see Section 2.3). While this is superior to the detection limit of the Hall sensors reported here, it is still quite comparable. Given that the noise performance of the sensors discussed here is still limited by instrumentation, Hall sensors have the potential to outperform submicron SQUIDs [27] following implementation of more sophisticated read-out techniques [60].

Moreover, ultraclean graphene Hall sensors work in a much less restricted parameter space than SQUIDs. Importantly, tuning the carrier density enables optimization of the detection limit over large ranges of both temperature and magnetic field. Also, the dry-transfer fabrication process offers flexibility to fabricate Hall sensors directly on top of materials of interest or incorporate the devices into a scanning probe. Scanning Hall probe microscopy with a high-performing graphene sensor can enable the imaging of magnetic fields over a

combined range of temperatures and magnetic fields not accessed with a single scanning probe to date. The detection of small magnetic field variations with a single solid-state sensor over a broad parameter space is promising for studying a range of condensed matter systems including unconventional superconductors across their magnetic field-temperature phase diagram, magnetic-field-tuned phases of matter, and electric currents in regimes of electronic transport that appear at high temperature and magnetic field.

CHAPTER 5

CALCULATION OF ELECTRICALLY TUNABLE AND REVERSIBLE MAGNETOELECTRIC COUPLING IN STRAINED BILAYER GRAPHENE

In this Chapter, I calculate the strength of an orbital magnetoelectric effect in strained bilayer graphene. This effect is remarkable in that it describes a magnetization that is predicted to develop in a system without any intrinsic spin magnetism, with an expected magnitude ~5400 $\mu_B/\mu m^2$ for 1 % uniaxial strain and a 10 µA bias current. This is three orders of magnitude larger than a similar magnetization reported experimentally for strained monolayer MoS_2. Moreover, I identify regimes in which the magnetoelectric effect switches sign not only upon reversal of the interlayer electric field but also in response to small changes in the carrier density. Finally, I propose to use scanning magnetometry to probe the effect directly. The theoretical results discussed here directly motivate the experimental progress towards strained graphene devices in Chapter 6.

This work is based on a manuscript in preparation, and I acknowledge Kin Fai Mak and Erich Mueller for productive and enlightening discussions.

5.1 Introduction

Two-dimensional hexagonal Dirac materials are a promising platform for realizing orbital magnetic effects. In these materials, the low-energy band structure features two degenerate energy minima (or "valleys") at the K and K' points at the corners of the Brillouin zone [107]. If inversion symmetry is broken, the energy bands are directly gapped at each valley. In this case, the electronic states in

each valley are characterized by a strong intrinsic magnetic moment and Berry curvature [108]. These quantities differ in sign between the two valleys, exhibiting distributions centered at K and K' with maxima that typically increase with decreasing magnitude of the gap [109]. The control of orbital magnetic moments is both fundamentally and technologically interesting: it provides a direct window into phenomena driven by the Berry curvature and may provide an efficient way to switch magnetic layers through the generation of strong magnetic torques [110, 111]. However, in equilibrium the contributions to the total magnetic moment from the two valleys cancel precisely. Different strategies to induce and detect a net magnetization have been demonstrated in particular for devices involving transition metal dichalcogenides (TMDs) and graphene.

Here, I focus on Bernal-stacked bilayer graphene (BLG) which is promising for generating a strong, purely orbital magnetization for several reasons. First, the maximum magnetic moment is expected to be inversely related to the interlayer asymmetry Δ [109]. This quantity describes a potential energy difference between the two layers and controls the size of the bandgap (see Appendix D.2) [109]. In dual-gated BLG devices, the size and sign of Δ can be tuned independently of the carrier density through an interlayer electric field [112–114]. The low charge inhomogeneity in BLG devices enables operation at low carrier densities, which is necessary to take advantage of the enhanced magnetic moment at small bandgap. Second, graphene has a nearly vanishing spin-orbit coupling [107]. This suggests that the magnetic moment in BLG is entirely orbital in origin, in contrast with TMDs in which spin contributions can be intertwined with orbital effects [108, 115]. Finally, BLG has a rich low-energy fermiology due to trigonal warping of the band structure, offering an interesting platform in which to study orbital magnetism [116–118].

5.1.1 Approaches to create a net orbital magnetization

Naturally, one route towards generating a net orbital magnetization is to create a net valley polarization [109]. This can be achieved by selective optical excitation of electrons in a single valley using circularly polarized light as demonstrated previously in MoS_2 [119, 120]. An electrically tunable valley polarization has also been realized in WSe_2/CrI_3 heterostructures, in which the valley polarization of WSe_2 is controlled through proximity coupling to CrI_3 [121]. However, the terahertz-scale optical transitions and lack of spin-orbit coupling in BLG make these methods difficult to extend to BLG.

An alternative way to create a net orbital magnetization was demonstrated in uniaxially strained MoS_2 devices through a magnetoelectric effect: application of an in-plane electric field drives a transport current that induces a net orbital magnetization [122, 123]. Here, I consider the analogous effect in strained bilayer graphene (sBLG). This effect does not rely on a net valley polarization but rather on the combination of uniaxial tensile* strain, which breaks the rotational symmetry of the lattice, a bias current, which breaks time-reversal symmetry, and an interlayer electric field, which breaks layer inversion symmetry.

In the following, I briefly illustrate the key principle behind the effect using results from the model described below (Section 5.2). In Figure 5.1(a), I show the lattice, Brillouin zone, and low-energy band structure for gapped BLG at zero strain. The magnetic moment associated with each valley (colored shading) is strongly enhanced close to the K and K′ points. In BLG, trigonal warping of the band structure gives rise to three mini-valleys while preserv-

*Graphene-based devices often possess a small critical buckling strain in compression [124, 125], so I restrict my attention to tensile strain states.

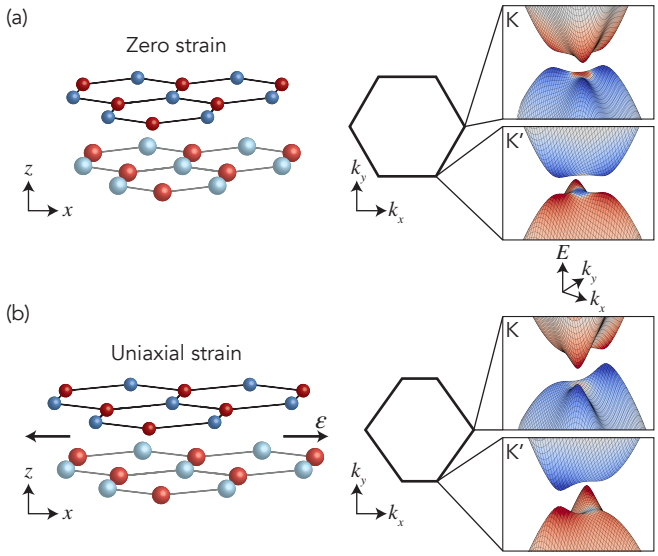

Figure 5.1: Schematics of the BLG lattice, Brillouin zone, and low-energy band structure for the K and K′ valleys under (a) zero strain (b) uniaxial tensile strain along the zigzag crystal axis (geometry exaggerated). The low-energy band structure is calculated with $\Delta = 7$ meV, $\theta = 0$, and (c) $\varepsilon = 0$ or (d) $\varepsilon = 0.01$ (see Section 5.2). The intensity of the shading represents the magnitude of the orbital magnetic moment, and the color of the shading represents its sign, which differs in each band and between the two valleys.

ing three-fold rotational symmetry [116]. The mini-valleys produce hotspots for the orbital magnetic moment distribution as represented by the shading in Figure 5.1(a) [117, 118]. Applying uniaxial strain to the BLG lattice (Figure 5.1(b)) breaks the three-fold rotational symmetry and distorts the energy bands and magnetic moment distribution as shown. Despite this distortion, the magnetic moment distributions in the two valleys are still equal in magnitude and opposite and sign, leading to zero net magnetization. However, an in-plane electric field creates a time-reversal symmetry breaking electric current. This induces a non-equilibrium occupation of charge carriers whose center is shifted in the same direction in momentum space for each valley. Integrating over contributions from occupied states in each valley therefore leads to a net bulk magnetization that is purely orbital in nature. The strength of this effect is characterized

by a magnetoelectric susceptibility, i.e. the coefficient describing the magnitude of induced magnetization per unit applied electric field.

As I show later, the sign of the magnetoelectric susceptibility can be switched electrically in a few different ways: by reversal of the current bias direction, tuning the uniaxial strain, changing the carrier type, or with even smaller changes in carrier density in some regimes. These observations are consistent with the previously reported behavior of the Berry curvature dipole in sBLG [118]. The Berry curvature dipole is related to the magnetoelectric susceptibility and has been studied in the context of nonlinear Hall effects [126–129]. In Ref. [118], the authors demonstrate that the trigonal warping of the sBLG band structure leads to a strong Berry curvature dipole in the presence of uniaxial strain and a bias current, exhibiting sign reversal upon continuous tuning of either strain or carrier density. My analysis supports, expands upon, and recontextualizes these general observations as a magnetoelectric effect with similar origin.

Recently, strong orbital magnetic effects have also been discovered and explored both experimentally and theoretically in twisted bilayer graphene (TBG) systems [13, 130–136]. Interestingly, the magnetization in these systems undergoes electric switching, sometimes hysteretic, induced by small changes in either carrier density or an applied bias current. The exact physical origin of the magnetization reversal in TBG is yet unclear. Recent articles suggest either a magnetoelectric effect similar to the one considered here [133, 134] or entirely different mechanisms related to strong electronic interactions in the flat bands of TBG [137, 138]. In contrast with TBG, the sign change in sBLG coincides with rich changes in the Fermi surface originating from the warping of the band structure under strain.

5.1.2 Chapter overview

In Section 5.2, I describe the tight-binding model I use to calculate the energy bands and eigenstates for sBLG under uniaxial strain*. Then, I calculate the Berry curvature and orbital magnetic moment (Section 5.3), and I define the linear magnetoelectric susceptibility (Section 5.3.1). Next, I explore tuning the susceptibility as a function of various tuning parameters and comment on the expectations for the analogous experimental quantities (Section 5.4). I discuss the expected magnitude of the effect in Section 5.5 and conclude by proposing an experiment to detect the effect using scanning magnetometry in Section 5.6.

5.2 Tight-binding model

I construct a tight-binding model for sBLG with a 4×4 Hamiltonian yielding four energy bands E_n labeled with $n \in (0, 1, 2, 3)$ from lowest to highest energy. The wavefunction $\mathbf{\Psi}_n(\mathbf{k})$ for each band has components $\psi_n^{\sigma i}(\mathbf{k})$ corresponding to the wavefunction amplitude for each layer $\sigma \in (\mathrm{A}, \mathrm{B})$ and sublattice $i \in (1, 2)$.

*The Python source code used for the calculations is available at `https://github.com/nowacklab/blg_strain`.

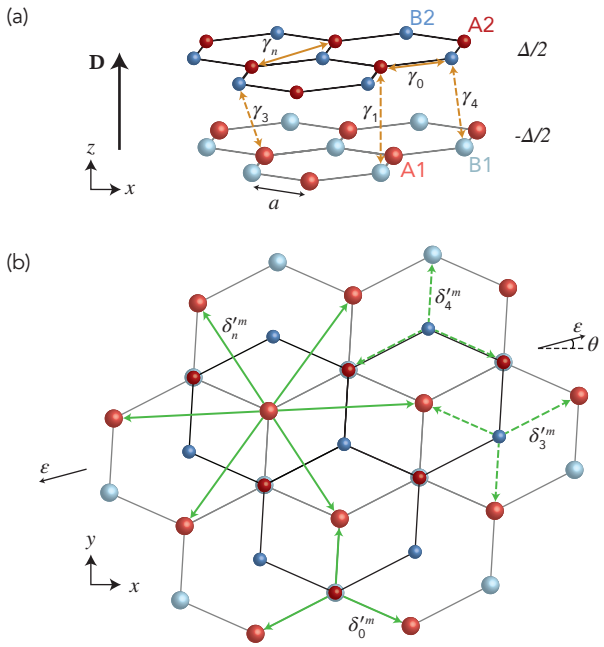

Figure 5.2: (a) Schematic of the unstrained BLG lattice, with hopping parameters γ_j, interlayer asymmetry Δ, and displacement field $\mathbf{D}$. Atoms A2 and B1 are stacked directly on top of one another. (b) Schematic top view of BLG lattice under uniaxial strain with magnitude ε applied at an angle $\theta \approx 15°$ to the x (zigzag) axis, with modified bond vectors $\boldsymbol{\delta}''^m_j$. The dashed (solid) arrows in each panel represent interlayer (intralayer) coupling.

Written in the basis (A1, B2, A2, B1), the Hamiltonian and its eigenstates are

$$H = \begin{pmatrix} -\frac{1}{2}\Delta + h_n & h_3 & h_4 & h_0 \\ h_3^* & \frac{1}{2}\Delta + h_n & h_0^* & h_4^* \\ h_4^* & h_0 & \frac{1}{2}\Delta + \Delta' + h_n & h_1 \\ h_0^* & h_4 & h_1^* & -\frac{1}{2}\Delta + \Delta' + h_n \end{pmatrix} \tag{5.1}$$

$$|n\rangle \equiv \boldsymbol{\Psi}_n(\mathbf{k}) = \begin{pmatrix} \psi_n^{\mathrm{A1}}(\mathbf{k}) \\ \psi_n^{\mathrm{B2}}(\mathbf{k}) \\ \psi_n^{\mathrm{A2}}(\mathbf{k}) \\ \psi_n^{\mathrm{B1}}(\mathbf{k}) \end{pmatrix},$$

Hopping processes	Matrix element	γ_j (eV)	η_j	Zero-strain bond vectors $\boldsymbol{\delta}_j^m/a$
A1-B1 A2-B2	h_0	3.16	−2	$\left(\frac{\sqrt{3}}{2}, -\frac{1}{2}\right)$; $\left(-\frac{\sqrt{3}}{2}, -\frac{1}{2}\right)$; $(0, 1)$
A2-B1	h_1	−0.381	—	$(0, 0)$
A1-B2	h_3	0.38	−1	$\left(-\frac{\sqrt{3}}{2}, \frac{1}{2}\right)$; $\left(\frac{\sqrt{3}}{2}, \frac{1}{2}\right)$; $(0, -1)$
A1-A2 B1-B2	h_4	0.14	−1	$\left(\frac{\sqrt{3}}{2}, -\frac{1}{2}\right)$; $\left(-\frac{\sqrt{3}}{2}, -\frac{1}{2}\right)$; $(0, 1)$
A1-A1 A2-A2 B1-B1 B2-B2 (next-nearest neighbor)	h_n	~ 0.3	−1	$\left(\sqrt{3}, 0\right)$; $\left(-\sqrt{3}, 0\right)$; $\left(\frac{\sqrt{3}}{2}, \frac{3}{2}\right)$; $\left(-\frac{\sqrt{3}}{2}, \frac{3}{2}\right)$; $\left(\frac{\sqrt{3}}{2}, -\frac{3}{2}\right)$; $\left(-\frac{\sqrt{3}}{2}, -\frac{3}{2}\right)$

Table 5.1: Hopping processes in the tight-binding model and corresponding matrix elements h_j, Slonczewski-Weiss-McClure hopping parameters γ_j, Grüneisen parameters η_j, and zero-strain bond vectors $\boldsymbol{\delta}_j^m$ reported in units of the carbon-carbon distance $a = 0.142$ nm. The magnitudes of the hopping parameters use the values reported in Ref. [139] and the typical estimate $\gamma_n \sim 0.1\gamma_0$ [140]. The signs of the hopping parameters are chosen to address the ambiguity discussed in Ref. [141,142]. The magnitude of the Grüneisen parameter η_0 follows from both Raman spectroscopy measurements ($\eta_0 \approx -1.99$) and first principles calculations ($\eta_0 \approx -1.87$) [143]. The estimate $\eta_{3,4,n} \sim -1$ accounts for the longer intralayer and next-nearest neighbor bond lengths [117,144].

where the elements h_j are defined below. Δ is the interlayer asymmetry resulting from an applied electric displacement field D between the layers (Figure 5.2(a)) and $\Delta' \sim 0.022$ eV accounts for a small energy cost associated with the dimerization of B1-A2 atoms [117,139,145].

The matrix elements h_j describe inter- and intralayer interactions using the Slonczewski-Weiss-McClure parameterization (Table 5.1) [146,147]. In the notation of this model, each h_j involves hopping parameters with amplitudes γ_j, multiplied by a structure factor considering the relevant bonds for the hop-

ping interactions with bond vectors $\boldsymbol{\delta}_j^m$ as listed in Table 5.1 and illustrated in Figure 5.2(a). Here, the subscript j denotes either intralayer nearest neighbor ($j = 0$), dimer ($j = 1$), interlayer ($j = 3, 4$), or intralayer next-nearest-neighbor ($j =$ "n") interactions. Introducing strain into the model leads to deformation of each bond vector in a way that depends on its direction, leading to modified hopping parameters γ_j^m paired with structure factors involving modified bond vectors $\boldsymbol{\delta}'^m_j$. In the end, this leads to matrix elements with the form $h_j = \sum_m \gamma_j^m e^{i\mathbf{k}\cdot\boldsymbol{\delta}'^m_j}$, where the index m runs over the bonds listed in Table 5.1 and illustrated in Figure 5.2(b).

Here, strain modifies the bond vectors to linear order according to $\boldsymbol{\delta}'^m_j = \left(\bar{\mathbf{I}} + \bar{\boldsymbol{\epsilon}}\right) \cdot \boldsymbol{\delta}_j^m$, where $\bar{\mathbf{I}}$ is the 2×2 identity matrix and $\bar{\boldsymbol{\epsilon}}$ is an arbitrary two-dimensional strain tensor [148, 149]. The strength of each corresponding hopping parameter is expected to depend exponentially on the bond length following $\gamma_j^m = \gamma_j e^{\eta_j\left(\left|\boldsymbol{\delta}'^m_j\right|/\left|\boldsymbol{\delta}_j^m\right| - 1\right)}$, where η_j is the appropriate Grüneisen parameter (Table 5.1) [148–150]. For uniaxial tensile strain as illustrated in Figure 5.2(b), the strain tensor is

$$\bar{\boldsymbol{\epsilon}} = \varepsilon \begin{pmatrix} \cos^2\theta - \nu \sin^2\theta & (1+\nu)\cos\theta\sin\theta \\ (1+\nu)\cos\theta\sin\theta & \sin^2\theta - \nu\cos^2\theta \end{pmatrix}. \tag{5.2}$$

Here, ε is the strain magnitude, θ is the direction of the principal strain axis, and $\nu \approx 0.165$ is the Poisson's ratio for graphene* [148].

The tunable parameters in the Hamiltonian are the strain state $\bar{\boldsymbol{\epsilon}}(\varepsilon, \theta)$ and interlayer asymmetry Δ resulting from an applied electric field between the layers (Figure 5.2(a)). For each choice of $\bar{\boldsymbol{\epsilon}}$ and Δ, I compute and diagonalize the Hamiltonian to obtain the energy bands and eigenstates over a momentum-space grid

*If strain is transferred via adhesion to a flexible substrate, it would instead be appropriate to use the Poisson's ratio for the substrate [143].

around the K valley. Rather than performing the same diagonalization for states around the K′ valley, I obtain energy and eigenstates in the K′ valley directly from the corresponding values in the K valley considering the in-plane inversion symmetry of the Hamiltonian $H(k_x, k_y) = H(-k_x, -k_y)$, valid even under uniaxial strain.

5.3 Orbital magnetic moment

I now calculate the orbital magnetization from the eigenstates of the Hamiltonian. The total orbital magnetization includes contributions from the orbital magnetic moment $\boldsymbol{\mu}$ and Berry curvature $\boldsymbol{\Omega}$. For a Hamiltonian independent of k_z (see Appendix D.1),

$$\begin{aligned}\boldsymbol{\mu}_n(\mathbf{k}) &= \frac{e}{2\hbar} i \left\langle \boldsymbol{\nabla}_{\mathbf{k}} n \right| \times \left[E_n(\mathbf{k}) - H(\mathbf{k}) \right] \left| \boldsymbol{\nabla}_{\mathbf{k}} n \right\rangle = -\frac{e}{\hbar} \operatorname{Im} \sum_{m \neq n} \frac{\langle n | \partial_{k_x} H | m \rangle \langle m | \partial_{k_y} H | n \rangle}{E_n(\mathbf{k}) - E_m(\mathbf{k})} \hat{\mathbf{z}} \\ \boldsymbol{\Omega}_n(\mathbf{k}) &= i \left\langle \boldsymbol{\nabla}_{\mathbf{k}} n \right| \times \left| \boldsymbol{\nabla}_{\mathbf{k}} n \right\rangle = -2 \operatorname{Im} \sum_{m \neq n} \frac{\langle n | \partial_{k_x} H | m \rangle \langle m | \partial_{k_y} H | n \rangle}{\left[E_n(\mathbf{k}) - E_m(\mathbf{k}) \right]^2} \hat{\mathbf{z}}\end{aligned} \tag{5.3}$$

where $|\boldsymbol{\nabla}_{\mathbf{k}} n\rangle$ is the momentum-space gradient of the eigenstate for band n [117]. These both contribute to a total magnetic moment $\boldsymbol{\mathcal{M}}_n$ for each band n originating from orbital degrees of freedom:

$$\begin{aligned}\boldsymbol{\mathcal{M}}_n(\mathbf{k}) &= \boldsymbol{\mu}_n(\mathbf{k}) + \frac{e \boldsymbol{\Omega}_n(\mathbf{k})}{\hbar} \left[\mu - E_n(\mathbf{k}) \right] \\ &= -\frac{e}{\hbar} \operatorname{Im} \sum_{m \neq n} \frac{\langle n | \partial_{k_x} H | m \rangle \langle m | \partial_{k_y} H | n \rangle}{E_n(\mathbf{k}) - E_m(\mathbf{k})} \left[1 + 2 \frac{\mu - E_n(\mathbf{k})}{E_n(\mathbf{k}) - E_m(\mathbf{k})} \right] \hat{\mathbf{z}}\end{aligned} \tag{5.4}$$

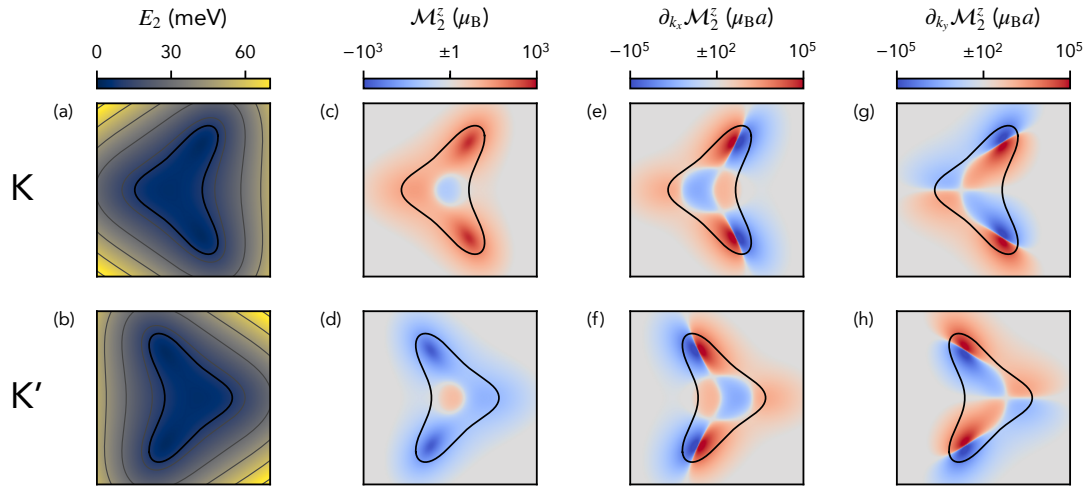

Figure 5.3: (a)-(b) Conduction band, (c)-(d) magnetic moment distributions, and (e)-(h) their gradients for sBLG in the K (top row) and K′ (bottom row) valley. The black contour outlines the Fermi surface at chemical potential μ = 10 meV. The model parameters are Δ = 7 meV, ε = 0.01, and θ = 0° (strain applied along the x zigzag axis). The maps span a $0.05a^{-1} \times 0.05a^{-1}$ region of momentum space centered at each valley. Panels (c)-(h) use a logarithmic color scale, where the neutral-colored regions represent regions of momentum space in which $|\mathcal{M}_2^z| \leq \mu_B$ or $|\partial_{k_x}\mathcal{M}_2^z| \leq 10^2\ \mu_B a$.

At zero temperature, the orbital magnetization is an integral of this quantity over occupied states in momentum space* [108, 151–153]:

$$\mathbf{M} = \sum_n \int \frac{\mathrm{d}^2\mathbf{k}}{(2\pi)^2} f_n(\mathbf{k}) \boldsymbol{\mathcal{M}}_n(\mathbf{k}) \tag{5.5}$$

where $f_n(\mathbf{k})$ is the occupation function, which is a step function in equilibrium at zero temperature:

$$f_n^0(\mathbf{k}) = \Theta[\mu - E_n(\mathbf{k})].$$

Figure 5.3(a-d) shows an example of the conduction band $E_2(\mathbf{k})$ and its magnetic moment distribution $\mathcal{M}_n^z(\mathbf{k})$ in the K and K′ valleys under applied strain. The magnetic moment differs in sign between the two valleys as expected from

*The zero-temperature expression should describe well experiments performed at liquid-helium temperature, at which $k_B T$ = 0.36 meV.

overall inversion symmetry, but is concentrated asymmetrically into hotspots reflecting the breaking of three-fold rotational symmetry from strain. With the equilibrium occupation function, the total magnetization (Equation 5.5) vanishes due to equal and opposite contributions from the two valleys. However, an electric current creates non-equilibrium occupation functions that encompass different amounts of magnetic moment in each valley.

5.3.1 Linear magnetoelectric susceptibility

Under the linear relaxation-time approximation, application of an in-plane electric field $\boldsymbol{\mathcal{E}} = (\mathcal{E}_x, \mathcal{E}_y)$ leads to a non-equilibrium occupation function [154]

$$f_n(\mathbf{k}) \approx f_n^0(\mathbf{k}) + \frac{e\tau\boldsymbol{\mathcal{E}}}{\hbar} \cdot \boldsymbol{\nabla}_{\mathbf{k}} f_n^0(\mathbf{k}),$$

where τ is a mean scattering time. In graphene, I assume a typical universal Planckian scattering time of typical magnitude $\hbar/k_{\mathrm{B}}T \sim 2$ ps at liquid-helium temperature [155, 156]. The electric field essentially causes a shift of the Fermi surface by a wave vector $|\delta\mathbf{k}| = e\tau|\boldsymbol{\mathcal{E}}|/\hbar$ in the same direction for each valley. As a result, the magnetic moment associated with occupied states differs between valleys and leads to a net magnetization. Inserting the occupation into Equation 5.5 and dropping the equilibrium term which integrates to zero, the $\boldsymbol{\mathcal{E}}$-dependent orbital magnetization is

$$M_z = \frac{e\tau\boldsymbol{\mathcal{E}}}{\hbar} \cdot \sum_n \int \frac{\mathrm{d}^2\mathbf{k}}{(2\pi)^2} \boldsymbol{\nabla}_{\mathbf{k}} f_n^0(\mathbf{k}) \mathcal{M}_n^z(\mathbf{k}).$$

Integrating by parts and discarding the boundary term which evaluates to zero,

$$M_z = -\frac{e\tau\boldsymbol{\mathcal{E}}}{\hbar} \cdot \sum_n \int \frac{\mathrm{d}^2\mathbf{k}}{(2\pi)^2} f_n^0(\mathbf{k}) \boldsymbol{\nabla}_{\mathbf{k}} \mathcal{M}_n^z(\mathbf{k}).$$

This result can be reframed as a magnetoelectric effect with a linear relationship between applied electric field $\boldsymbol{\mathcal{E}}$ and a resultant magnetization M_z. I define a dimensionless linear magnetoelectric susceptibility $\boldsymbol{\alpha} = (\alpha_x, \alpha_y)$ such that

$$\mu_0 M_z = \tau(\boldsymbol{\alpha} \cdot \boldsymbol{\mathcal{E}}), \tag{5.6}$$

with

$$\boldsymbol{\alpha} = -\frac{e\mu_0}{\hbar} \sum_n \int \frac{\mathrm{d}^2\mathbf{k}}{(2\pi)^2} f_n^0(\mathbf{k}) \boldsymbol{\nabla}_{\mathbf{k}} \mathcal{M}_n^z(\mathbf{k}). \tag{5.7}$$

Defining $\boldsymbol{\alpha}$ in this way separates the dependence on τ and $\boldsymbol{\mathcal{E}}$, facilitating comparison of the magnitude of M_z for different experimental conditions.

To visualize that the integration yields non-vanishing $\boldsymbol{\alpha}$, I show the k_x and k_y components of $\boldsymbol{\nabla}_{\mathbf{k}} \mathcal{M}_2^z(\mathbf{k})$ in Figure 5.3(e-h). In the case of a diagonal strain tensor, each distribution exhibits symmetry over a central horizontal mirror line. Within either valley, this symmetry leads to $\alpha_y = 0$, but net nonzero α_x. The contributions to α_x from each valley are equal in both sign and magnitude and therefore contribute to a magnetoelectric effect of form $\mu_0 M_z = \tau \alpha_x \mathcal{E}_x$, proportional to only the x component of electric field. Non-diagonal strain tensors lead to nonzero components of both α_x and α_y (see Section 5.4.3).

5.4 Tuning the magnetoelectric susceptibility

In the following sections, I explore the magnetoelectric susceptibility along several directions of the parameter space spanned by strain magnitude ε, strain direction θ, electric field direction ϕ (see Section 5.4.2), interlayer asymmetry Δ, and chemical potential μ:

- Section 5.4.1: Dependence on electrically tunable parameters Δ, μ with fixed ε, θ.
- Section 5.4.2: Dependence on strain magnitude with varying ε, μ and fixed θ, Δ.
- Section 5.4.3: Dependence on strain and electric field directions θ, ϕ with fixed Δ, μ, ε.

5.4.1 Interlayer asymmetry and chemical potential

I map out α_x as a function of Δ and μ in Figure 5.4(b) for two different orientations of strain as indicated in Figure 5.4(a). Experimentally, applying gate voltages does not directly control these parameters, but rather the related parameters of interlayer electric displacement field D and carrier density n (see Appendix D.3) [112–114]. I therefore re-map the values of α_x versus n and D, which distorts the map as shown in Figure 5.4(c). I compute the carrier density n_i for each layer i as the sum of the amplitudes of the wave function on each sublattice, with a factor of 4 for spin-valley degeneracy [116]:

$$n_i = 4 \sum_n \int \frac{\mathrm{d}\mathbf{k}}{(2\pi)^2} f_n^0(\mathbf{k}) \left[\left|\psi_n^{Ai}\right|^2 + \left|\psi_n^{Bi}\right|^2 \right]. \tag{5.8}$$

The total carrier density is merely $n = n_1 + n_2$, and the displacement field D is related to Δ accounting for screening from charge distributed unequally between the layers [116, 157]:

$$\Delta = \frac{ed}{\epsilon_0} \left[D + e(n_2 - n_1) \right], \tag{5.9}$$

where $d = 0.34$ nm is the interlayer spacing.

These maps exhibit a rich structure. They are asymmetric between the conduction ($\mu > 0$) and valence ($\mu < 0$) bands but symmetric upon reversal of Δ

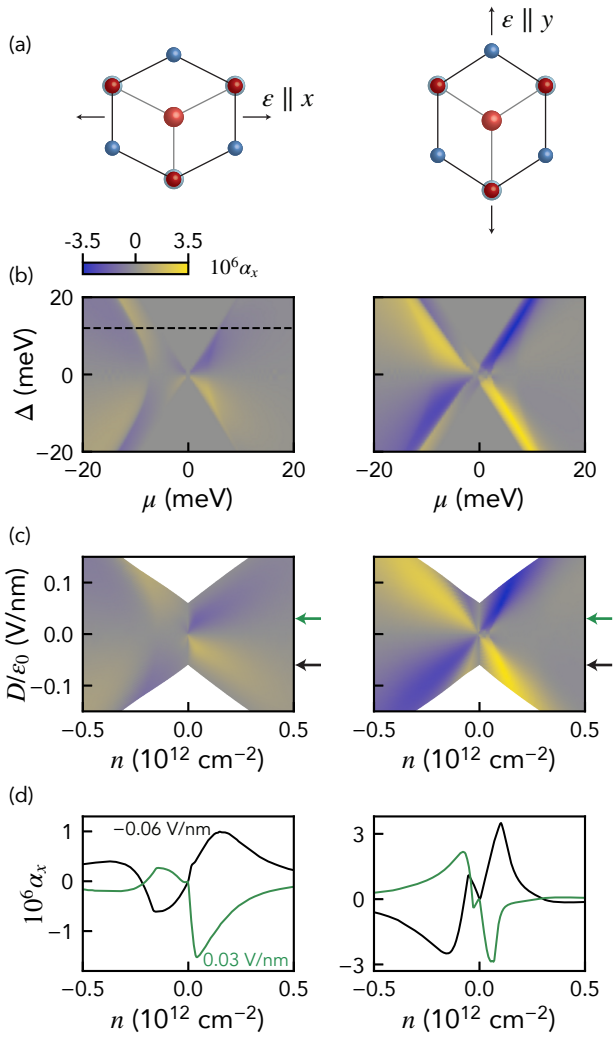

Figure 5.4: Magnetoelectric susceptibility α_x for strain of magnitude $\varepsilon = 0.01$ aligned along the x axis (left panels) or y axis (right panels). (a) Schematic illustration of each strain state (not to scale). (b) Maps against freely tunable model parameters Δ and μ. (c) The same maps as in (b) transformed onto axes of derived parameters D and n. The white triangular regions correspond to values of D and n not covered by the range of Δ and μ considered in (b). (d) Line profiles for fixed D/ε_0 at positions indicated by the arrows in (c).

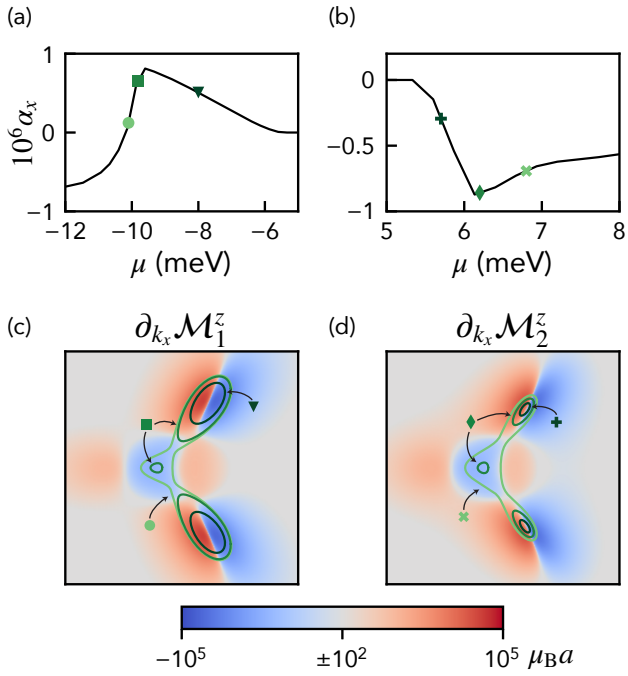

Figure 5.5: (a) Valence band and (b) conduction band line profiles of α_x from Figure 5.4(b) at $\Delta = 12$ meV. (c) $\partial_{k_x}\mathcal{M}_1^z$ at $\mu = -10.1$ meV and (d) $\partial_{k_x}\mathcal{M}_2^z$ at 6.8 meV, with Fermi surface contours at the values of μ marked in (a)-(b). From left to right: circle, −10.1 meV; square, −9.8 meV; triangle, −8.0 meV; "+", 5.7 meV; diamond, 6.2 meV; "×", 6.8 meV.

or D, with a clear non-monotonic dependence on the parameters. In both strain configurations, α_x reaches a broad maximum centered at larger $|n|$ for larger $|D|$, as evident in the line profiles in Figure 5.4(d). Notably, the sign of α_x is fairly uniform in each of the four quadrants of the map, but also exhibits a sharp reversal in the valence band ($\mu < 0$ or $n < 0$). This suggests that the orientation of M_z can be reversed upon changing the carrier type, reversing the direction of the displacement field, or applying even smaller perturbations to either n or D.

The distinctive features in α_x coincide with Lifshitz transitions, changes in the topology of the Fermi surface. Figure 5.5(a,b) shows line profiles from the left panel of Figure 5.4(b) at fixed Δ, and Figure 5.5(c,d) shows the Fermi surfaces for a few values of μ superimposed on the momentum-space distribution

of $\partial_{k_x} \mathcal{M}^z$. For small $|\mu|$ near the band edges, the Fermi surface first consists of two pockets approximately centered around the hotspots of $\mathcal{M}$ (darkest contours). Sweeping to larger $|\mu|$, a central third pocket appears, and the three pockets eventually merge into a single continuous Fermi surface (lightest contour). The appearance of the third pocket coincides with a cusp in α_x, and the merging of the pockets coincides with an inflection point. In the valence band, α_x changes sign approximately at this inflection point. The electron-hole asymmetry here is a consequence of the electron-hole asymmetry induced by model parameters Δ', γ_4, and γ_n [116]. These observations are also similar to those reported in Ref. [118], which demonstrates a sign change in the Berry curvature dipole resulting from Lifshitz transitions and warping of the Fermi surface under uniaxial strain.

5.4.2 Strain magnitude

Increasing the strain amplitude ε alters the magnetic moment distribution and Fermi surface nontrivially. My calculations support a saturation of the net magnetic moment; i.e. larger strain does not monotonically increase the magnetization. In Figure 5.6, I fix Δ and show α_x as a function of μ and ε. As ε increases, α_x also generally increases for strain below ~0.5 %, but becomes highly nonlinear and non-monotonic for larger strain (see right panels). The colored bands in Figure 5.6 indicate an approximate saturation of the peak value of $|\alpha_x|$. The sharp features related to the Fermi surface topology as discussed in Section 5.4.1 generally occur at larger values of $|\mu|$ when the bands are distorted upon increasing strain. However, for large $|\mu|$ where the Fermi surface consists of a single pocket, α_x is approximately proportional to ε (dotted curves in Figure 5.6). This

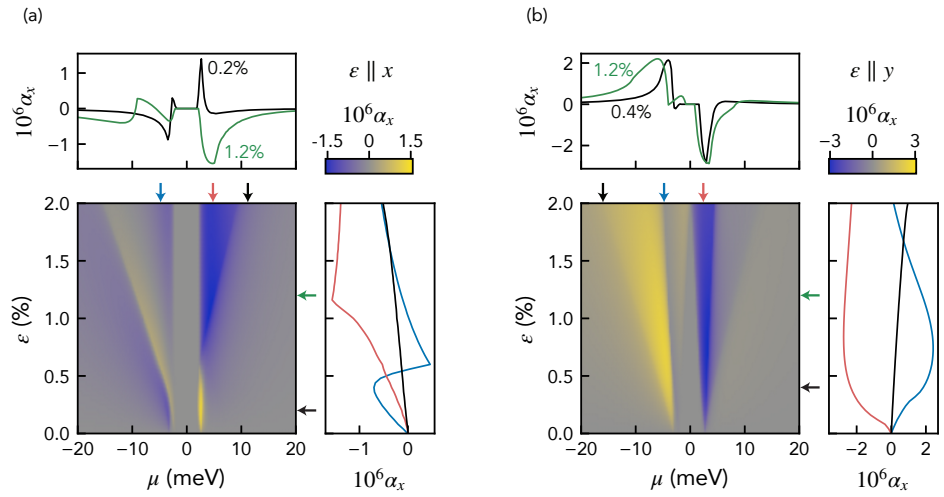

Figure 5.6: α_x versus strain magnitude ε and chemical potential μ for fixed $\Delta = 5$ meV, with strain along either (a) the x direction or (b) the y direction. The arrows above (to the right of) the main panel indicate the positions of the line profiles in the upper (right) panels. The upper arrows correspond to the following values of μ (in meV, from left to right): (a) −4.8, 4.8, 11.2; (b) −16.0, −4.8, 2.4. The arrows to the right correspond to the following values of ε (from top to bottom): (a) 1.2 %, 0.2 %; (b) 1.2 %, 0.4 %.

monotonic, linear dependence of α_x on ε is consistent with the magnetoelectric effect previously reported in strained monolayer MoS_2, which has a larger and approximately circular Fermi surface [122, 123].

5.4.3 Strain and electric field orientation

Next, I consider how the magnetization depends on the relative orientation of the principal strain axis, in-plane electric field, and crystallographic axes. In Figure 5.7(a), I consider the case of fixed strain along x or y resulting in a diagonal strain tensor and $\alpha_y = 0$. The magnetization therefore follows $M_z \propto \boldsymbol{\alpha} \cdot \hat{\boldsymbol{\mathcal{E}}} = \alpha_x \cos\varphi$, where φ is the angle between $\boldsymbol{\mathcal{E}}$ and the x axis. Importantly, for strain along either x or y, M_z is maximized (zero) with $\boldsymbol{\mathcal{E}}$ along x

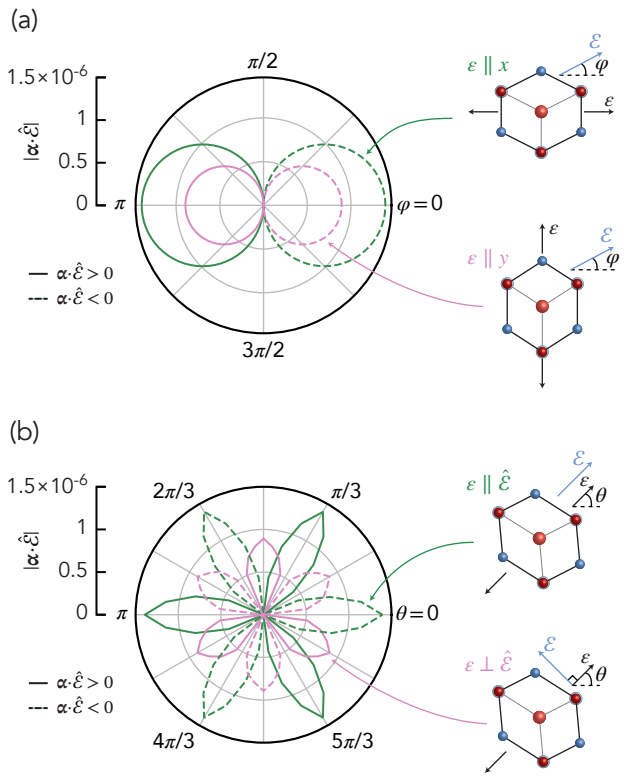

Figure 5.7: Polar plots of $|\boldsymbol{\alpha} \cdot \hat{\boldsymbol{\mathcal{E}}}| \propto |M_z|$ versus (a) the angle φ between $\hat{\boldsymbol{\mathcal{E}}}$ and the x axis or (b) the angle θ between the principal strain axis and the x axis. In both panels, the fixed model parameters are $\Delta = 4$ meV, $\mu = 4$ meV, and $\varepsilon = 0.01$, and the radial coordinate represents $|\boldsymbol{\alpha} \cdot \hat{\boldsymbol{\mathcal{E}}}|$ up to a maximum of 1.5×10^{-6}. The solid (dashed) part of each curve indicates where $M_z > 0$ ($M_z < 0$). In (a), the principal strain axis is fixed along x (y) for the upper/green (lower/pink) configuration. In (b), $\hat{\boldsymbol{\mathcal{E}}}$ is parallel (perpendicular) to the principal strain axis for the upper/green (lower/pink) configuration.

(y).

In Figure 5.7(b), I instead essentially consider a rotation of the crystal relative to two configurations of $\boldsymbol{\mathcal{E}}$ and the principal strain axis, with the two directions either parallel or perpendicular to each other. The angular dependence here demonstrates a six-fold symmetry originating from the unstrained crystal, with the maxima and minima aligning with armchair and zigzag directions. The magnitude of M_z changes monotonically between these extrema, approximately

following $\boldsymbol{\alpha} = |\alpha|(\cos 3\theta, \sin 3\theta)$. This is consistent with the expectation that both components of $\boldsymbol{\alpha}$ should be nonzero only when the strain tensor is non-diagonal, which occurs when the principal strain axis is along either an armchair or zigzag crystal axis.

The angular orientation of strain and electric field is clearly an important consideration in the fabrication of sBLG devices in pursuit of a magnetoelectric effect. To provide a concrete recommendation, for practical devices with parallel strain and electric field (see Section 5.6 and Section 6.5), the crystal should be strained along a zigzag axis to maximize the effect.

5.5 Overall magnitude of the effect

The results discussed above are obtained within the linear relaxation-time approximation. This assumes that the shift of the Fermi surface $|\delta\mathbf{k}| = e\tau|\boldsymbol{\mathcal{E}}|/\hbar$ does not exceed the momentum-space width (typically $0.01a^{-1} = 7 \times 10^7\,\mathrm{m}^{-1}$, from Figure 5.5). Together with the estimate $\tau \sim 2$ ps (see Section 5.3.1), this suggests a maximum electric field strength $|\boldsymbol{\mathcal{E}}| < 23\,000\,\mathrm{V\,m}^{-1}$, and I will choose $|\boldsymbol{\mathcal{E}}|^{\max} = 10^4\,\mathrm{V\,m}^{-1}$ to be concrete. For a device with channel width W and sheet resistance ρ, the the magnetoelectric effect (Equation 5.6) can be written

$$M_z = \frac{\tau\alpha_x\rho}{W\mu_0} I \sim 0.005I, \tag{5.10}$$

where the dimensionless coefficient is calculated using estimates $W \sim 1\,\mu\mathrm{m}$, $\rho \sim 1\,\mathrm{k}\Omega$, and maximum $\alpha_x \sim 3 \times 10^{-6}$ for 1 % uniaxial strain (Figure 5.4).

This is expected to describe the system up to a maximum bias current* $I^{\max} = |\mathcal{E}|^{\max} W/\rho \sim 10\,\mu\text{A}$, corresponding to a maximum magnetization of magnitude $50\,\text{nA} = 5400\,\mu_B/\mu\text{m}^2$.

The strength of the orbital magnetization estimated here is among the highest magnitudes previously reported in both theoretical and experimental studies summarized in Appendix D.4. For tight-binding predictions with typical ~0.5-1 % uniaxial tensile strain as considered here, $M_z/I \sim 5 \times 10^{-6}$ in strained single-layer MoS_2 [122,123], $M_z/I \sim 10^{-3}$ in strained monolayer $NbSe_2$ [160], and $M_z/I \sim 4 \times 10^{-4}$ in a moiré heterostructure based on twisted bilayer graphene and hexagonal boron nitride [133]. The sBLG system studied here is predicted to exhibit a larger effect with $M_z/I \sim 5 \times 10^{-3}$ (Equation 5.10), a result of the larger magnetic moment and asymmetric redistribution of magnetic moment around the valley center.

5.6 Experimental detection of the magnetoelectric effect

Experiments to study the magnetoelectric effect in sBLG require two essential components: (1) a technique to introduce large-scale homogeneous strain into dual-gated BLG devices with electrical contacts and (2) a technique to detect the resultant magnetization. In MoS_2 [122, 123], the magnetization can be probed using magneto-optic imaging, but due to the small bandgap in BLG this technique proves challenging here. I therefore consider scanning magnetometry

*While graphene devices are in principle able to sustain large bias current densities > $10^8\,\text{A cm}^{-2}$ ($I \gtrsim 1\,\text{mA}$ for a $W = 1\,\mu\text{m}$ device), in practice transport currents in micrometer-scale devices are limited to ~10 µA to avoid self-heating and thermal or potential gradients [44, 158, 159].

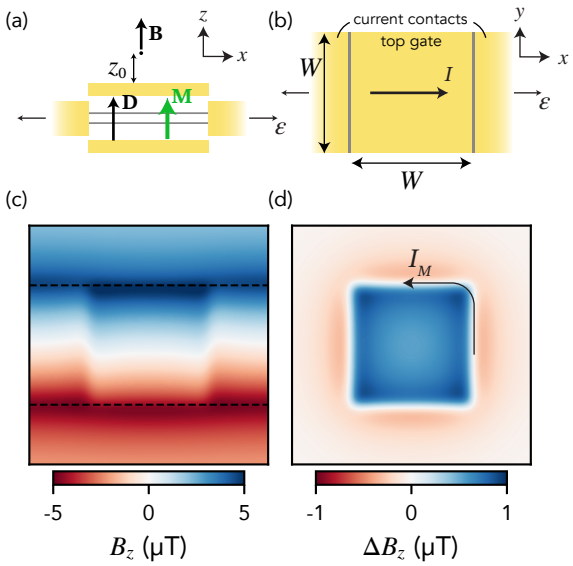

Figure 5.8: (a) Side view and (b) top view schematics of a 1 μm × 1 μm square sBLG device with orbital magnetization $\mathbf{M} = M_z\hat{z}$. The metal electrodes simultaneously strain the device along the x axis and bias the device with a current I in the $+x$ direction. The top and bottom metal gates tune the carrier density n and displacement field D. (c) Total out-of-plane stray magnetic field B_z at a height $z_0 = 100$ nm above the surface of the device for $M_z/I = 0.05$ and $I = 10$ μA. (d) Difference in magnetic field $\Delta B_z = [B_z(D) - B_z(-D)]/2$ between images at opposite D.

techniques that detect the stray magnetic field above the surface of a device (see Chapter 2). Scanning SQUID, Hall probe, and nitrogen-vacancy center microscopy are well-established techniques and lend themselves well to this system [9,13,23,30,39]. Achieving an ideal sBLG device is less straightforward (see Chapter 6), but several recently developed experimental approaches enable the simultaneous application of continuous and reversible strain and electric current to devices made from two-dimensional materials, albeit with the devices strained in a bending configuration [123,161–163].

The structure illustrated in Figure 5.8(a,b) is an idealized architecture for a $W \times W$ square sBLG device that is strained and electrically biased with the same pair of metal contacts. Applying voltage to the top and bottom metal gates

tunes the electric displacement field D and carrier density n and is expected to modify the strength of the effect (see Figure 5.4). The total magnetic field is a superposition of two effective magnetic field sources:

$$B_z(\mathbf{r}) = B_{\text{bias}}(\mathbf{r}) + B_{\text{sBLG}}(\mathbf{r}).$$

$B_{\text{bias}}(\mathbf{r})$ is the Oersted field from the bias current, modeled using an infinitely long, width-W wire with current flowing in the $+x$ direction (see Appendix A.4). $B_{\text{sBLG}}(\mathbf{r})$ is the stray magnetic field from the orbital magnetization, which is modeled as an effective current I_M of the same magnitude flowing at the boundary of the device (see Appendix A.5).

Figure 5.8(c) shows a typical magnetic image of the z component of the stray magnetic field at height $z_0 = 100$ nm above the surface of a sBLG device. $B_{\text{bias}}(\mathbf{r})$ dominates the image, with a slight distortion from the magnetization. The contrast between the two sources of field is essentially controlled by the ratio M_z/I, which is predicted to be rather small, and Figure 5.8(c) uses a value of M_z/I ten times larger than estimated from the tight-binding model to clarify the features. Subtracting images corresponding to opposite values of D essentially removes the Oersted field contribution and reveals the stray field from the magnetization (Figure 5.8(d)).

To improve the sensitivity of measurements, it is often useful to operate with ac signals typically at frequencies below 1 kHz. Applying an ac bias current, for example, will generate an ac magnetic field signal that can be demodulated using a lock-in amplifier to extract the magnitude of the magnetic response. Alternatively, applying a small ac perturbation to a dc gate voltage can modulate the carrier density and displacement field, thereby causing a modulation of the magnetoelectric susceptibility. This technique eliminates the need to take the

difference between images of the magnetic field under opposite D, but complicates the quantitative extraction of the magnetoelectric susceptibility because of its nonlinear dependence on n and D. Moreover, such ac modulation has the potential to couple electrically to a metallic probe and introduce artifacts into the magnetic images [164]. Nevertheless, the calculations here establish a promising experimental approach to measuring the magnitude of the magnetoelectric effect in sBLG and its dependence on tunable parameters.

5.7 Conclusion

In summary, I developed a tight-binding model for strained bilayer graphene that predicts an orbital magnetization on the order of up to $5000\,\mu_B/\mu m^2$ under a 1 % uniaxial strain and 10 µA bias current. My tight-binding construction improves upon formerly developed low-energy models, including the next-nearest neighbor coupling and supporting an arbitrary strain tensor. The results discussed here not only motivate the experimental confirmation of the effect (see Chapter 6), but also encourage the conception of functional devices making use of the orbital magnetoelectric effect. For example, substitution of magnetized sBLG for traditionally ferromagnetic layers in spintronic device architectures can lead to the development of magnetic tunnel junctions and spin transistors driven by orbital degrees of freedom [110].

CHAPTER 6

FABRICATION OF STRAINED BILAYER GRAPHENE DEVICES

In Chapter 5, I predicted the magnitude of an orbital magnetoelectric effect expected in strained bilayer graphene (sBLG). Here, I describe my experimental progress towards detecting this effect as proposed in Section 5.6. I focus on three key experimental components:

- Design of a uniaxial mechanical strain rig compatible with scanning magnetometry (Section 6.1)
- Fabrication of BLG devices on strainable polyimide substrates (Section 6.2, Section 6.3)
- Raman spectroscopy measurements to measure uniaxial strain in sBLG devices (Section 6.4, Section 6.5)

The combined constraints imposed by these components necessitate a significant departure from the standard fabrication and sample preparation approach as discussed in Chapter 3. Not only do sBLG devices require a completely different substrate than the conventional process, but the device design must enable adequate transfer of strain from the substrate into the sBLG layer. Below, I realize each of the three experimental components and point out any necessary modifications to the fabrication process. This work was performed in collaboration with Justin Oh.

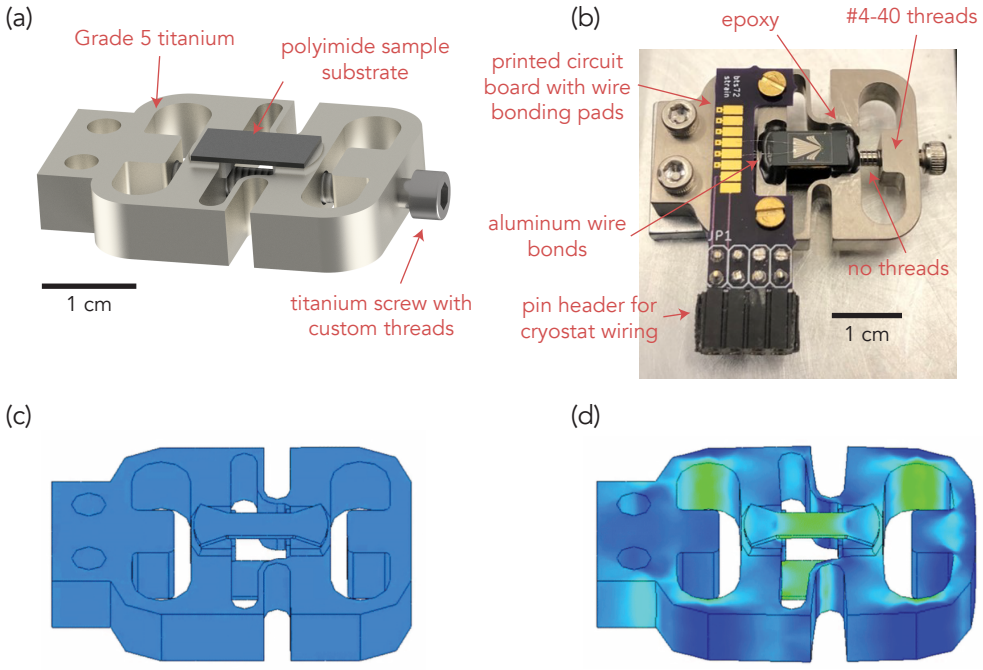

Figure 6.1: (a) Computer-aided design drawing of the screw-actuated strain rig. (b) Picture of the strain rig with sample. (c)-(d) Finite-element simulations, with the color representing the magnitude of strain under (c) zero displacement (d) finite displacement.

6.1 Mechanical strain apparatus design

I designed a screw-actuated mechanical strain rig based on a design from Veronika Sunko, Cliff Hicks, and Andy Mackenzie (Max Planck Institute for Chemical Physics of Solids, Dresden, Germany). As originally designed, the strain rig is capable of applying uniaxial tensile strain to bulk crystals in a geometry compatible with photoemission spectroscopy measurements, with the upper surface of the crystal fully exposed [165]. Scanning magnetometry also benefits from a fully accessible upper sample surface (see Section 2.4), making this an attractive base design for my experiment.

The strain rig in Figure 6.1 consists of a single-piece titanium spring

(High-Strength Grade 5 Titanium, McMaster-Carr 9081K259) and a partially threaded titanium screw (Titanium 4-40×1" Socket Head Screw, McMaster-Carr 95435A36). Using titanium for both the spring and screw avoids differential thermal contraction between the spring and screw when the assembly is cooled to cryogenic temperatures [165]. The left end of the screw rests against a flat surface on the left-hand side of the rig, and turning the screw engages threads on the right-hand side of the screw and rig, pulling apart the two halves of the central platform. Before engaging the screw*, I affix each sample substrate to the platform using Stycast 2850 FT epoxy, chosen for its known compatibility with the cryostat and its high thermal conductivity. Turning the screw displaces the two halves of the central platform and induces uniaxial strain in the sample. This rig can in principle induce strain into any material with sufficiently small elastic modulus, so long as the stress in the epoxy does not exceed its fracture strength. I performed finite-element simulations to illustrate that the strain is expected to be approximately uniform throughout the sample (Figure 6.1(c,d)).

Indium-bonded aluminum wire bonds (see Section 6.3) electrically connect the sample to a printed circuit board (PCB), which terminates in standard 0.1-inch pin headers that connect to the internal wiring of the measurement system. On the non-PCB side of the assembly, the top surface of the sample substrate is the most prominent feature, accommodating approach with a scanning probe microscope. Figure 6.2 shows a test fit of the strain rig mounted in a cryostat, demonstrating in principle the compatibility of this rig with a scanning SQUID microscope.

*Slightly engaging the screw prior to mounting the sample could help ensure that the screw is already engaged at zero strain in the sample.

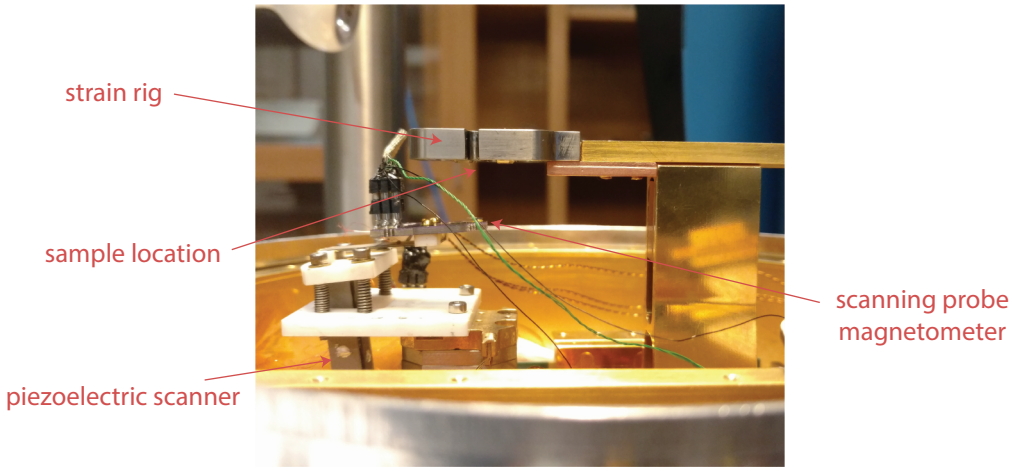

Figure 6.2: Scanning probe microscope with strain rig mounted to the sample platform (missing PCB, sample, and screw). Strain rig mounted in the cryostat with a scanning probe magnetometer. The lower left edge of the rig here is the upper right edge of the view in Figure 6.1.

6.2 Graphene devices on polyimide substrates

The fabrication of graphene-based devices with simultaneous electrical and strain control demands a readily accessible, thermally stable substrate with a low elastic modulus. Polyimide (often known by the brand name Kapton®) is widely used in cryogenic applications and flexible electronics and is available as a tape, film, wafer, or precursor solution. I purchased commercial polyimide wafers (Valley Design, 23250-1) with low surface roughness (advertised 5 nm) and dimensions similar to standard silicon wafers (thickness 500 µm, diameter 100 mm) for compatibility with existing fabrication tools. Despite the nominal nanometer-scale surface roughness, the bare wafer surfaces clearly exhibited scratches and inclusions on a mesoscopic scale (Figure 6.3(a)). An additional spun polyimide film ~2 µm (HD MicroSystems, PI-2610) improved the surface uniformity (Figure 6.3(b)) and resulted in an average roughness < 3 nm confirmed using atomic-force microscopy. The recipe for spinning this additional

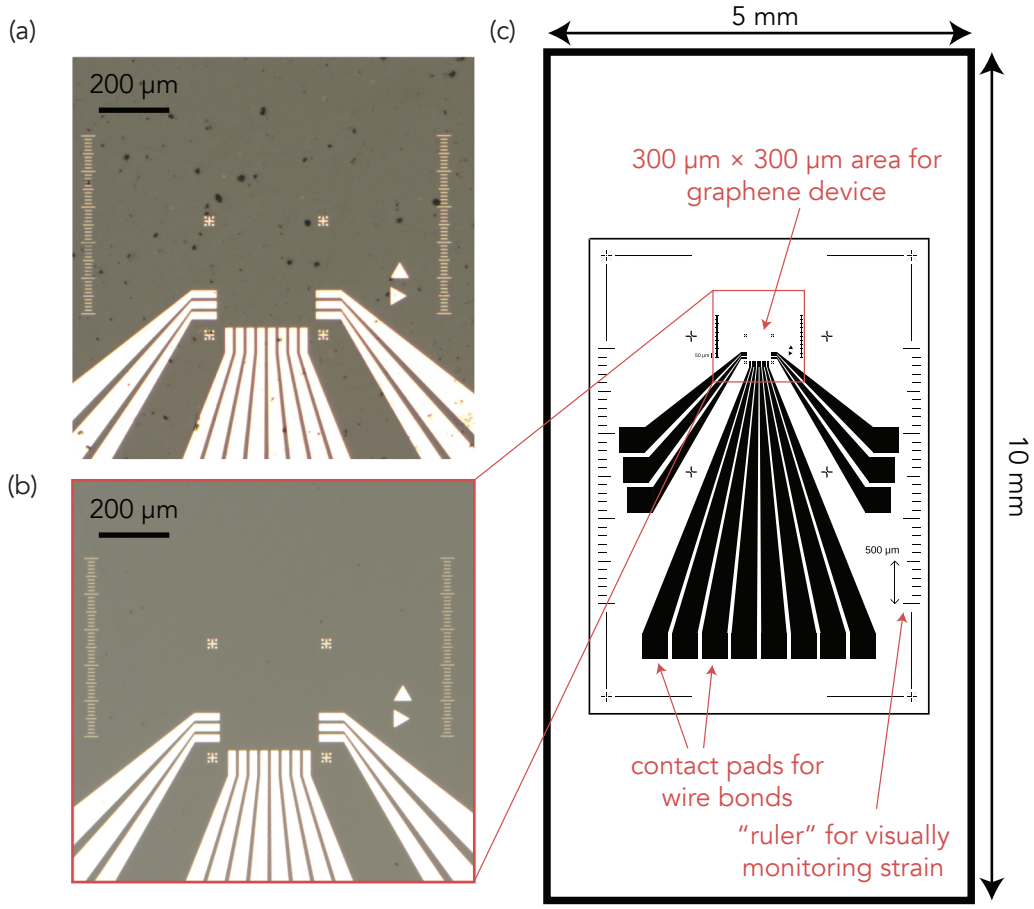

Figure 6.3: Patterned electrical contacts and alignment marks on a polyimide substrate (a) as received and (b) with an additional spin-coated polyimide layer.

polyimide layer is as follows (courtesy Justin Oh):

- Drop a generous amount of polyimide solution in the center of the wafer (as received, no cleaning steps)
- Spin at 500 rpm for 5 s with a ramp rate of 500 rpm/s
- Spin at 3000 rpm for 30 s with a ramp rate of 500 rpm/s
- Soft bake at 90 °C for 90 s
- Soft bake at 150 °C for 90 s

- Ramp temperature at ~4 °C min^{-1} to 280 °C and cure for 120 min
- Turn off hot plate and let cool to room temperature gradually

To aid with future fabrication steps, I pre-patterned the wafers with metal wire bonding pads and alignment marks using the standard photolithography process described in Appendix B.1. I then diced the wafers into individual 0.5 cm × 1 cm substrates compatible with the strain rig. Figure 6.3(c) shows an overview of the pre-patterned polyimide substrate design. Notably, the pre-patterned design also includes two sets of "rulers" used to estimate the amount of strain in the substrate. Similar to the procedure described in Chapter 3, each device involves a graphene-based heterostructure transferred to the marked central area. The following fabrication steps only involve this area of the substrate and use the innermost set of alignment marks.

In most cases, I deposited a pre-patterned metal backgate or contacts before transferring the heterostructure (using the metal evaporation/liftoff recipe in Appendix B.2 with 3 nm Cr/100 nm Au). A metal backgate is useful for several reasons: (1) it enables electrostatic tuning of carriers in the device, (2) it provides a smoother surface (~1 nm average roughness) upon which to place heterostructures, and (3) it enables the monitoring of strain via Raman spectroscopy (see Section 6.4). The subsequent electron-beam lithography, etching, metal evaporation, and liftoff steps are nearly identical to those discussed for graphene-based devices on silicon substrates discussed in Section 3.4, with full process details in Appendix B.2. Below I list the key considerations unique to fabrication on polyimide substrates:

- Polyimide substrates are slippery and pliable; manipulate them with flat-

tipped tweezers gripping along the long edges or flat top and bottom surfaces

- The pre-patterned metal has limited adhesion to the substrate and is readily scratched off. Avoid scraping the pre-pattern with tweezers.
- Exposure to organic solvents for extended periods of time can lead to likely irreversible swelling or deformation of the substrates. Immerse the substrates in solvents for the minimum necessary amount of time.
- The substrates are electrically insulating and can accumulate electrostatic charge.
  - Spin a layer of DisCharge (DisChem, Inc.) on top of resist before electron-beam lithography to avoid charging artifacts.
  - Once devices are wire-bonded, the risk of electrostatic discharge (ESD) is high. Strictly follow the suggestions discussed in Section 3.5, maintaining shorted device pins whenever possible.
  - Wire bond the devices a minimal number of times. Repeated bonding and de-bonding increases the chances of damage from ESD.

6.3 Sample preparation

Mounting substrates to strain rig

After finishing the cleanroom fabrication process and before making wire bond connections, I mount each polyimide substrate to the strain rig using the following procedure (potentially applicable to other types of samples as well):

- Roughen the sample mounting surfaces with medium-grit sandpaper to promote adhesion.
- Apply a drop of uncured epoxy to each mounting surface.
- Position the sample and press lightly on the surface of the sample until it lies flat.
- Apply additional epoxy to the edges of the sample at each mounting surface. Avoid dripping epoxy on the sample surface.
- Repeat the same steps for a dummy sample with similar geometry on the opposite side of the rig. Without the symmetric sample on the bottom, the rig does not displace uniaxially.
- Cure the epoxy on a hot plate according to the cure schedule for the epoxy, either 80 °C overnight (> 8 hours) or 120 °C for ~3 hours.

To remove a sample from the rig:

- Submerge the entire assembly in dichloromethane (DCM) for 30 min to partially dissolve the epoxy.
- Remove the assembly from the DCM bath while constantly rinsing with isopropyl alcohol (IPA).
- Gently blow dry with nitrogen.
- If the sample has not detached from the rig, use a razor blade underneath the sample to pry it off the rig without excessive bending.
- If the sample will not come free, repeat the procedure. Note: polyimide substrates will swell if left in DCM for too long and may not survive repeated mounting and unmounting.

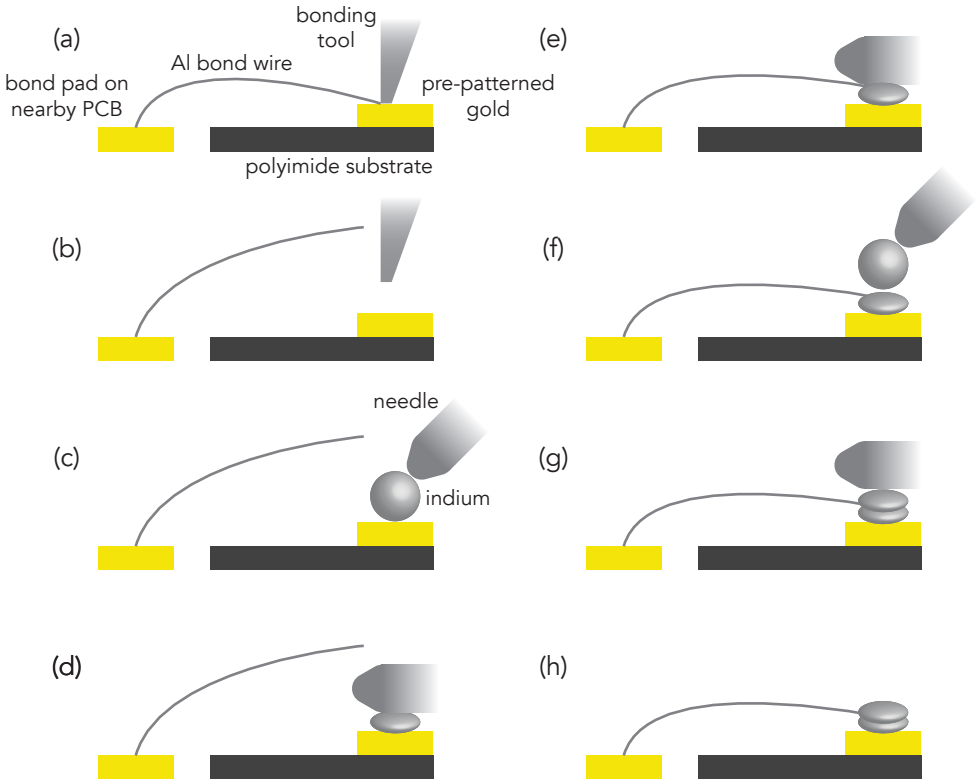

Figure 6.4: Process for attaching wire bonds to contact pads on polyimide substrates using indium ball bonding. (a) Attempt to make wire bond to the contact pad on the substrate. (b) Lift the bonding tool; the wire bond breaks and does not stick to the pad. (c) Pick up an indium ball with the tip of a needle and carefully place on top of the pad. (d) Gently press the indium ball with the side of the needle so that it sticks onto the pad. (e) Gently manipulate the free end of the wire with the side of the needle and press into the indium. (f) Pick up a second indium ball and place on top of the end of the wire stuck in the indium on the substrate. (g) Press the indium balls together to encapsulate the end of the wire. (h) Inspect the bond to ensure that the wire is securely embedded within the indium.

Indium ball bonding

Conventional wire bonding is not effective in creating electrical connections to soft substrates because the substrates absorb the ultrasonic energy from the wire bonder, preventing the formation of a cold weld between the wire and contact pad. I therefore developed an indium ball bonding technique to fix aluminum

wire bonds onto the gold contact pads on the substrate, illustrated in Figure 6.4 and described in the caption. In short, this process involves attaching one end of an aluminum wire to the nearby PCB (see Figure 6.1(b)) using conventional wire bonding and encapsulating the other end with indium*, which sticks to the metal pads on the substrate. All bonding pads on the PCB should be shorted together both during and after the bonding process, and the process should be carried out with ESD-safe tools while wearing a grounding strap. Keeping all electrical connections shorted together during handling and transportation of the strain rig assembly is essential towards preventing ESD, which can destroy the device contacts randomly and uncontrollably.

6.4 Raman spectroscopy

Raman spectroscopy is an attractive technique for estimating the amount of strain in graphene heterostructures non-invasively [149, 161]. The application of the technique to graphene is discussed thoroughly in Ref. [82], and I summarize some of the key principles here. The Raman spectrum is essentially a measurement of the inelastic scattering of photons that interact with materials to excite vibrational modes. The wavelengths associated with each of these modes provide a "fingerprint" identifying the material. Straining the lattice of a material changes the bond lengths between atoms, in turn changing the resonant wavelength of each mode.

In high-quality graphene with a low defect density, there are two primary

*I used 0.008-inch diameter indium spheres with 99.99 % purity (The Indium Corporation, SPHEREIN-41016).

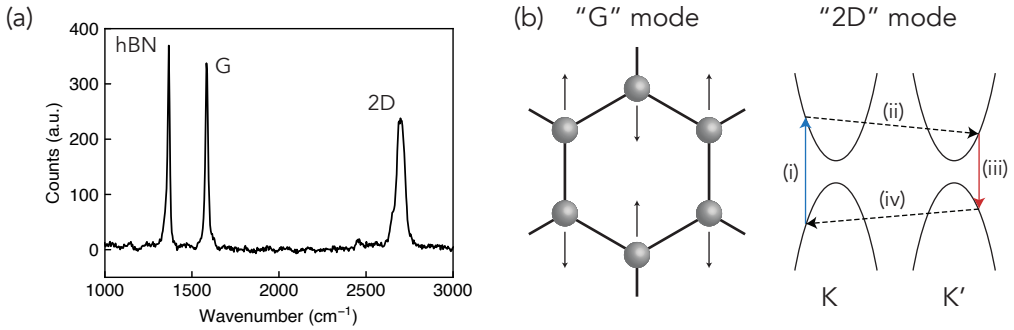

Figure 6.5: (a) Raman spectrum for a BLG/hBN device at zero strain. (b) Physical interpretation of the G and hBN peaks: an E_{2g} phonon mode. (c) Physical interpretation of one component of the 2D peak: (i) photon absorption, (ii) intervalley scattering and phonon emission, (iii) photon emission, and (iv) intervalley scattering and phonon emission. Adapted from Ref. [166].

resonances that appear in the Raman spectrum (see Figure 6.5): the G peak (~1585 cm^{-1}) and the 2D peak (~2700 cm^{-1}). The G peak corresponds to an E_{2g} phonon mode, while the 2D peak involves the exchange of phonons with opposite wavevector between the K and K' valleys [166]. Both the G and 2D modes are in-plane vibrations and therefore each resonance appear at approximately the same wavenumber for both MLG and BLG, but with different relative integrated intensity between the two. Also, the 2D mode for BLG consists of four overlapping components, arising from the presence of four electronic bands in BLG with slight electron-hole asymmetry. Hexagonal boron nitride (hBN) possesses a vibrational mode similar to the G mode but appearing at lower wavenumber (~1365 cm^{-1}), which appears in Raman spectra of graphene/hBN heterostructures alongside the graphene peaks.

6.4.1 Raman spectra of graphene and hBN under uniaxial strain

The application of strain to graphene distorts the lattice and therefore changes the wavelengths associated with the G and 2D vibrational modes [167]. The G (or hBN) mode both describe in-plane phonon modes, so the effect of strain on these peaks is not expected to differ between monolayer and multilayer graphene (or hBN) [143,168]. In short, uniaxial strain breaks the rotational symmetry of the lattice, creating two distinct modes that appear in the Raman spectrum as a split G (or hBN) peak. The two peaks emerge from the single G (or hBN) peak at zero strain, shifting linearly to lower wavenumber as strain increases. The shift rates are different for each of the peaks, and the shift rates are comparable between graphene and hBN [161,169].

The 2D peak, however, depends on the band structure and therefore responds differently to strain between MLG and BLG. In MLG, the 2D peak splits and shifts similarly to the G peak [170, 171]. However, in BLG the four overlapping modes of the 2D peak lead to a complicated dependence on strain and Raman laser polarization. Instead of splitting the 2D mode into multiple distinct peaks, strain instead changes the intensity and position of each of the overlapping modes, thereby changing the lineshape of the 2D peak [168]. Fitting this lineshape to four independent spectral peaks could prove challenging, so the 2D peak has limited utility towards estimating strain in BLG.

The specific evolution of the Raman peaks with strain depends on the relative orientation of the crystallographic axes, principal strain axis, and polarization of the Raman probe laser [143,167]. Straightforward calibration of the strain magnitude from Raman spectra therefore suggests the fabrication of devices with known crystallographic orientation, for simplicity with either an armchair

or zigzag axis oriented along the principal strain axis. It is also necessary to perform Raman measurements with linearly polarized photons, with a polarization angle known with respect to the crystal orientation.

6.4.2 Crystallographic orientation of exfoliated flakes

Polarized Raman spectroscopy allows for the identification of the crystallographic orientation of exfoliated graphene flakes via the intensity of the Raman D peak. The D mode is an intervalley process appearing when defects are present in the crystal. As such, it is usually absent in the center of pristine exfoliated graphene flakes, due to the lack of defect sites, and along zigzag edges, because these edges cannot scatter phonons between valleys [82]. Pristine armchair edges, however, can be seen as extended defects that break the overall translational symmetry of the lattice and permit intervalley scattering, leading to a D resonance [82]. Comparing the D mode intensity between a pair of edges with different chirality (i.e., straight edges of exfoliated flakes forming an odd multiple of 30° angle) therefore enables identification of the crystallographic orientation.

Following Ref. [172], I implemented a straightforward procedure to determine the crystallographic orientation of a BLG flake. I selected a flake with multiple straight edges and oriented the flake such that the horizontal Raman polarization makes an equal 15° angle with each straight edge (Figure 6.6(a)). I obtained Raman spectra along both the top and bottom edges of the flake (Figure 6.6(b)) to compare the relative intensity of the D peaks. In this case, the stronger D peak along the top edge identifies the top edge as an armchair

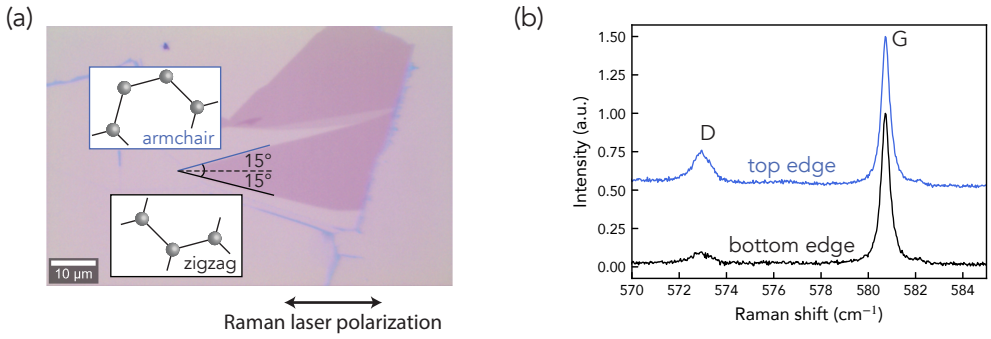

Figure 6.6: (a) Microscope image of a BLG flake with straight edges corresponding to the armchair (top edge) and zigzag (bottom edge) crystal axes. (b) Raman spectra normalized to the G peak intensity, with the laser spot focused on each edge as indicated.

axis and the bottom edge as a zigzag axis. Distinguishing the edge chirality of exfoliated BLG is essential towards experimentally realizing the orbital magnetoelectric effect discussed in Chapter 5, which depends strongly on the crystal orientation.

6.5 Progress towards robust strained bilayer graphene devices

I discuss here the design elements essential towards the fabrication of planar strain-tunable BLG devices, with the ultimate goal to fabricate a device with the ideal structure described in Figure 5.8, with a pair of electrical contacts and a pair of electrostatic gates. Each prototypical device includes a ~100 nm Au backgate, which enhances the optical contrast of the flakes against the substrate and attenuates a fluorescence interaction between the Raman probe laser and the polyimide substrate*. I consider three devices as shown in Figure 6.7, fabri-

*This fluorescence signal obscures the BLG and hBN Raman peaks without a sufficiently thick back gate (35 nm Au is too thin to attenuate the signal, but 100 nm Au is sufficient)

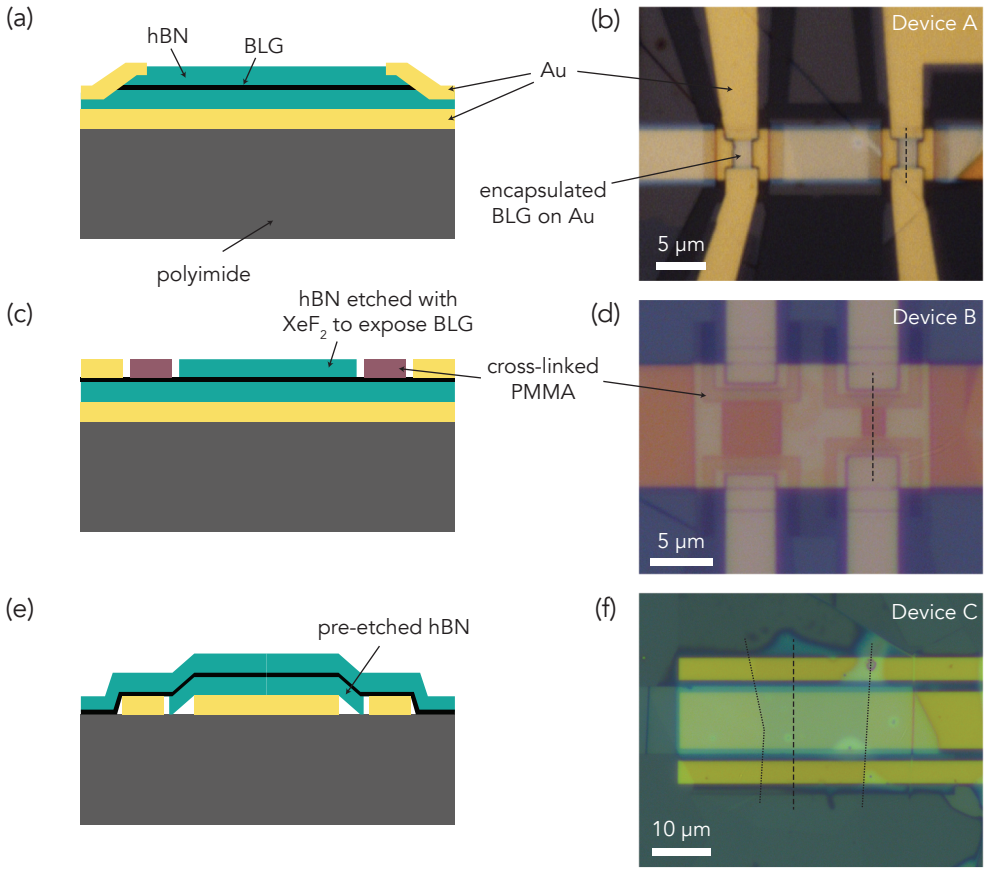

Figure 6.7: Cross-sectional views (a,c,e) and microscope images (b,d,f) of three prototypical sBLG devices: (a-b) Device A, (c-d) Device B, (e-f) Device C. The cross-sections are along the dashed lines in (b,d,f). The dotted lines in (f) outline the BLG flake.

cated as described briefly below. Each device demonstrates low-resistance electrical contact and conduction through the BLG layer, but Device C shows the most promise for controllability and reversibility of the applied strain:

- Device A: I etched partially through the bottom hBN layer and deposited edge contacts, following the general procedure of Ref. [161].
- Device B: I used XeF_2 etching to etch through the top hBN layer, ending precisely on the BLG layer (see Appendix B.3). I then pat-

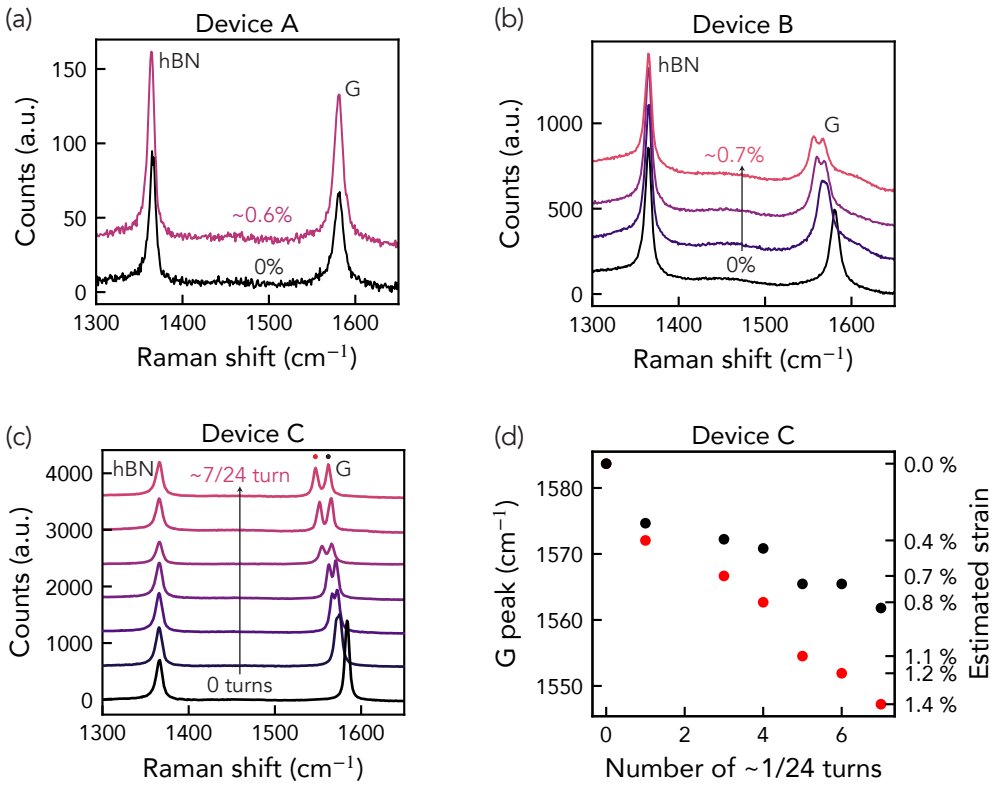

Figure 6.8: (a-c) Raman spectra for Devices A, B, and C. The labeled strain percentages for the spectra in (a) and (b) are estimated via optical inspection of the substrate. The labels for the spectra in (c) are the fractional number of turns of the screw on the strain rig. (d) Locations of the split G peak for increasing displacement of the strain rig. The red (black) markers correspond to the G peak at lower (higher) wavenumber. We estimate the strain by comparing the shift of the peak at lower wavenumber (red markers) to the reported shift in Ref. [174].

terned crosslinked poly(methyl methacrylate) (PMMA) "clamps" (see Appendix B.4), inspired by Ref. [173].

- Device C: I first pre-patterned a pair of metal electrodes surrounding the back gate. I then transferred a single layer of hBN onto the back gate and etched through the portions of the flake overlapping the contacts. Finally, I transferred a hBN/BLG heterostructure to complete the device, ensuring good overlap between the BLG flake and metal electrodes.

Figure 6.8 shows typical Raman spectra for the three devices under increasing strain. The curves are the result of 20 averaged Raman spectra accumulated for 2 s each using a WITec Alpha300R confocal Raman microscope with a 532 nm excitation, 2 mW laser power, and 1200 g/mm grating. The spectra clearly demonstrate no change in the hBN peak position for any device, but a shifting and splitting of the G peak for Devices B and C indicating a sizable amount of strain in the BLG layer. The differences between these spectra are likely attributed to the different contact geometries. In Device A, the one-dimensional edge contacts possess a small graphene-metal contact area and perhaps failed under a relatively small applied force; however, this geometry has been proven successful in a bending geometry [161]. Device B likely benefits from a larger metal-graphene contact area and the addition of crosslinked PMMA clamping strips. Finally, in Device C the large contact area between BLG and both the metal contact and polyimide substrate appears to provide the most promising strain transfer of the three designs.

Translating the redshift for each mode into a strain magnitude depends on the relative orientation of the Raman laser polarization, crystallographic axes of BLG, and principal strain axis [168], which I did not keep track of during these preliminary measurements. However, the clear evolution of the split G peak suggests a maximal strain exceeding 1 %, comparing to prior experimental results [143,168,174]. This is in agreement with the amount of strain in the substrate, estimated using pre-patterned "rulers" on the substrate (see Figure 6.3).

The hBN peak does not change in any of the devices upon application of strain to the substrate, even though it is expected to split into two peaks separated by ~17 cm^{-1} [169], which would be clearly resolved against the con-

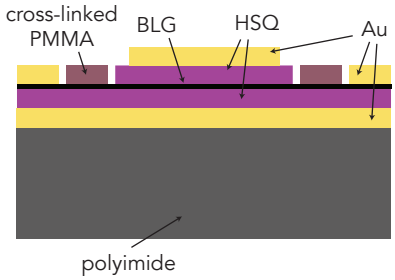

Figure 6.9: A proposed future device architecture for sBLG devices, with hydrogen silsesquioxane (HSQ) dielectric layers, crosslinked PMMA clamps, metal contacts, and metal top and bottom gates.

stant ~8 cm^{-1} linewidth of the hBN peak. Strain therefore does not transfer into the hBN layers, consistent with the observation that low friction at the graphene/hBN interface can enable the relative translation of rotation of the two layers with respect to each other in the absence of strain in either of the layers [64, 175–177]. The absence of strain in hBN suggests that the graphene layer may adhere somehow to the pre-patterned metal or the substrate, while the hBN slides freely above and underneath the graphene layer.

6.5.1 Proposal of alternative sBLG device architecture

Having established steps towards an effective sBLG device, I propose an alternative architecture to help elucidate the strain transfer mechanism. The proposed structure, drawn schematically in Figure 6.9, is similar to that of Device B discussed above, with the substitution of hydrogen silsesquioxane (HSQ) for hBN and the addition of a metal top gate. HSQ is a negative-tone electron-beam lithography resist that, when exposed to high electron-beam doses, becomes a network of bonded silicon and oxygen atoms with composition and function similar to that of SiO_2 [178]. Though often removed

after lithographic patterning, HSQ has also been used as an encapsulating layer [179] and gate dielectric [180] in high-mobility graphene devices. Similar to graphene on hBN, graphene is not expected to adhere strongly to a SiO_2-like surface [177,181]; however, crosslinked PMMA strips can effectively clamp graphene to SiO_2 [173]. This final architecture therefore may facilitate strain transfer from the substrate to the graphene layer, and in addition possesses a top gate as necessary for the experiment proposed in Section 5.6.

6.6 Conclusion and outlook

I have demonstrated a technique to create sBLG devices under uniaxial strain with electrical contacts and electrostatic gates. While my devices so far include only a bottom gate, they provide a solid proof of concept and motivate the continued development of similar devices. These sBLG devices ideally can be electrically tuned over a wide region of electrical gating parameter space, in particular to study the orbital magnetoelectric effect discussed in Chapter 5. Moreover, this work motivates the fabrication of similar devices from MLG and other exfoliated two-dimensional materials, with the potential to explore a variety of unusual photonic, electronic, and topological phenomena enabled by the application of uniaxial strain [117,149,182].

APPENDIX A

MAGNETIC FIELD AND FLUX FROM COMMON SOURCES

Here, I consider each of the magnetic field sources discussed in Section 2.5.1 and calculate the flux through a square loop with side length a at position (x_0, y_0, z) relative to the source. The magnetic flux is an integral of the magnetic field over this bounded surface:

$$\Phi(\boldsymbol{r}_0) = \int_{x_-}^{x_+} \mathrm{d}x \int_{y_-}^{y_+} \mathrm{d}y \hat{\boldsymbol{z}} \cdot \boldsymbol{B}(\boldsymbol{r}),$$

using the shorthand notation $x_\pm \equiv x_0 \pm a/2$ and $y_\pm \equiv y_0 \pm a/2$.

A.1 Magnetic monopole

The magnetic field of a monopole source at the origin contributing total flux $\Phi_0 = h/(2e)$ is:

$$\boldsymbol{B}(\boldsymbol{r}) = \frac{\Phi_0}{2\pi r^2}\hat{\boldsymbol{r}},$$

satisfying $\iint \mathrm{d}\boldsymbol{S} \cdot \boldsymbol{B}(\boldsymbol{r}) = \Phi_0$ when integrated over the entire x-y plane. At a height z, the flux through the square loop is:

$$\begin{aligned}
\Phi(\boldsymbol{r}_0) &= \frac{\Phi_0}{2\pi} \int_{y_-}^{y_+} \mathrm{d}y \int_{x_-}^{x_+} \mathrm{d}x \frac{1}{x^2+y^2+z^2}\hat{\boldsymbol{r}} \cdot \hat{\boldsymbol{z}} \\
&= \frac{\Phi_0}{2\pi} \int_{y_-}^{y_+} \mathrm{d}y \int_{x_-}^{x_+} \mathrm{d}x \frac{z}{(x^2+y^2+z^2)^{3/2}} \\
&= \frac{\Phi_0}{2\pi} \int_{y_-}^{y_+} \mathrm{d}y \left[\frac{xz}{(y^2+z^2)\sqrt{x^2+y^2+z^2}} \right]_{x_-}^{x_+} \\
&= \frac{\Phi_0}{2\pi} \int_{y_-}^{y_+} \mathrm{d}y \left[\frac{x_+ z}{(y^2+z^2)\sqrt{x_+^2+y^2+z^2}} - \frac{x_- z}{(y^2+z^2)\sqrt{x_-^2+y^2+z^2}} \right]
\end{aligned}$$

$$= \frac{\Phi_0}{2\pi}\left[\tan^{-1}\frac{x_+ y}{z\sqrt{x_+^2+y^2+z^2}} - \tan^{-1}\frac{x_- y}{z\sqrt{x_-^2+y^2+z^2}}\right]_{y_-}^{y_+}$$
$$= \frac{\Phi_0}{2\pi}[\mathcal{M}(x_+, y_+) + \mathcal{M}(x_-, y_-) - \mathcal{M}(x_+, y_-) - \mathcal{M}(x_-, y_+)]$$

where

$$\mathcal{M}(x, y) \equiv \tan^{-1}\frac{xy}{z\sqrt{x^2+y^2+z^2}}.$$

Directly above the source ($x_0 = y_0 = 0$),

$$\Phi(\boldsymbol{r}_0) = \frac{2\Phi_0}{\pi}\tan^{-1}\frac{a^2}{4z\sqrt{a^2/2+z^2}}.$$

A.2 Magnetic dipole

The magnetic field of a dipole point source at the origin with magnetic moment $\boldsymbol{m} = m\hat{\boldsymbol{z}}$ is:

$$\begin{aligned}\boldsymbol{B}(\boldsymbol{r}) &= \frac{\mu_0}{4\pi}\frac{3\hat{\boldsymbol{r}}(\hat{\boldsymbol{r}}\cdot\boldsymbol{m}) - \boldsymbol{m}}{r^3} \\ &= \frac{\mu_0 m}{4\pi}\left[\frac{3z}{(x^2+y^2+z^2)^2}\hat{\boldsymbol{r}} - \frac{1}{(x^2+y^2+z^2)^{3/2}}\hat{\boldsymbol{z}}\right]\end{aligned}$$

As above,

$$\begin{aligned}\Phi(\boldsymbol{r}_0) &= \frac{\mu_0 m}{4\pi}\int_{y_-}^{y_+}\mathrm{d}y\int_{x_-}^{x_+}\mathrm{d}x\left[\frac{3z^2}{(x^2+y^2+z^2)^{5/2}} - \frac{1}{(x^2+y^2+z^2)^{3/2}}\right] \\ &= \frac{\mu_0 m}{4\pi}\int_{y_-}^{y_+}\mathrm{d}y\int_{x_-}^{x_+}\mathrm{d}x\left[\frac{2z^2-x^2-y^2}{(x^2+y^2+z^2)^{5/2}}\right] \\ &= \frac{\mu_0 m}{4\pi}\int_{y_-}^{y_+}\mathrm{d}y\left[\frac{x[(x^2+y^2)(z^2-y^2)+2z^4]}{(y^2+z^2)^2(x^2+y^2+z^2)^{3/2}}\right]_{x_-}^{x_+} \\ &= \frac{\mu_0 m}{4\pi}\int_{y_-}^{y_+}\mathrm{d}y\left[x_+\frac{(x_+^2+y^2)(z^2-y^2)+2z^4}{(y^2+z^2)^2(x_+^2+y^2+z^2)^{3/2}}\right. \\ &\qquad\left. - x_-\frac{(x_-^2+y^2)(z^2-y^2)+2z^4}{(y^2+z^2)^2(x_-^2+y^2+z^2)^{3/2}}\right]\end{aligned}$$

$$= \frac{\mu_0 m}{4\pi} \left[x_+ \frac{y(x_+^2 + y^2 + 2z^2)}{(x_+^2 + z^2)(y^2 + z^2)\sqrt{x_+^2 + y^2 + z^2}} \right.$$
$$\left. - x_- \frac{y(x_-^2 + y^2 + 2z^2)}{(x_-^2 + z^2)(y^2 + z^2)\sqrt{x_-^2 + y^2 + z^2}} \right]_{y_-}^{y_+}$$
$$= \frac{\mu_0 m}{4\pi} \left[\mathcal{D}(x_+, y_+) + \mathcal{D}(x_-, y_-) - \mathcal{D}(x_+, y_-) - \mathcal{D}(x_-, y_+) \right]$$

where

$$\mathcal{D}(x, y) \equiv xy \frac{x^2 + y^2 + 2z^2}{(x^2 + z^2)(y^2 + z^2)\sqrt{x^2 + y^2 + z^2}}.$$

Directly above the source ($x_0 = y_0 = 0$),

$$\Phi(\boldsymbol{r}_0) = \frac{\mu_0 m a^2}{2\pi} \frac{1}{(a^2/4 + z^2)\sqrt{a^2/2 + z^2}}.$$

A.3 Current from an infinitesimal-width wire

From Ampere's law, the field circulating around an infinitely long, infinitesimally thin wire carrying current I in the $+x$ direction* is:

$$\boldsymbol{B}(\boldsymbol{r}) = \frac{\mu_0 I}{2\pi\sqrt{y^2 + z^2}} \hat{\boldsymbol{\theta}} \qquad \hat{\boldsymbol{\theta}} = \frac{y\hat{\boldsymbol{z}} - z\hat{\boldsymbol{y}}}{\sqrt{y^2 + z^2}}$$

The corresponding flux is:

$$\Phi(\boldsymbol{r}_0) = \frac{\mu_0 I}{2\pi} \int_{y_-}^{y_+} \mathrm{d}y \int_{x_-}^{x_+} \mathrm{d}x \left[\frac{y}{y^2 + z^2} \right]$$
$$= \frac{\mu_0 I a}{4\pi} \log(y^2 + z^2)\Big|_{y_-}^{y_+}$$
$$= \frac{\mu_0 I a}{4\pi} \log \frac{y_+^2 + z^2}{y_-^2 + z^2}$$

*The calculation for current in the $+y$ direction is nearly identical.

A.4 Current from a finite-width wire

The current density for an infinitely long, width-w wire with current flowing in the $+x$ direction is:

$$\mathbf{J}_{\text{bias}}(\mathbf{r}') = \frac{I}{w}\delta(z')\Theta\left(w/2 + y'\right)\Theta\left(w/2 - y'\right)\hat{x}.$$

With the Biot-Savart law,

$$B_z(\mathbf{r}) = \frac{\mu_0}{4\pi}\int \mathrm{d}\mathbf{r}'\frac{\mathbf{J}(x', y', z') \times (\mathbf{r} - \mathbf{r}')}{|\mathbf{r} - \mathbf{r}'|^3},$$

the out-of-plane component of magnetic field is:

$$\begin{aligned} B_z(x, y, z) &= -\frac{\mu_0 I}{4\pi w}\int_{-\infty}^{\infty}\mathrm{d}y'\int_{-w/2}^{w/2}\mathrm{d}x'\frac{x - x'}{\left[(x - x')^2 + (y - y')^2 + z^2\right]^{3/2}} \\ &= -\frac{\mu_0 I}{2\pi w}\int_{-w/2}^{w/2}\mathrm{d}x'\frac{x - x'}{(x - x')^2 + z^2} \\ &= \frac{\mu_0 I}{4\pi w}\log\frac{(x - w/2)^2 + z^2}{(x + w/2)^2 + z^2}. \end{aligned}$$

Calculating flux as before,

$$\begin{aligned} \Phi(\boldsymbol{r}_0) &= \frac{\mu_0 I}{4\pi w}\int_{y_-}^{y_+}\mathrm{d}y\int_{x_-}^{x_+}\mathrm{d}x\log\frac{(x - w/2)^2 + z^2}{(x + w/2)^2 + z^2} \\ &= \frac{\mu_0 I a}{4\pi w}\int_{x_-}^{x_+}\mathrm{d}x\left\{\log[(x - w/2)^2 + z^2] - \log[(x + w/2)^2 + z^2]\right\} \\ &= \frac{\mu_0 I a}{4\pi w}\left[C(x_+ - w/2) + C(x_- + w/2) - C(x_+ + w/2) - C(x_- - w/2)\right], \end{aligned}$$

where

$$C(s) \equiv s[\log(s^2 + z^2) - 2] + 2z\tan^{-1}\frac{s}{z}.$$

This numerically approaches the result from the previous section for $w \to 0$.

A.5 Two-dimensional slab with uniform magnetization

The magnetization of a uniformly magnetized two-dimensional $w \times w$ square sheet is:

$$\mathbf{M}(\mathbf{r}) = M\Theta(w/2+x)\Theta(w/2-x)\Theta(w/2+y)\Theta(w/2-y)\delta(z)\hat{\mathbf{z}}$$

Taking the curl of the magnetization yields an effective current density equivalent to a current of magnitude M flowing counter-clockwise along the boundary of the device [66]:

$$\begin{aligned}\mathbf{J_M}(\mathbf{r}) &= \boldsymbol{\nabla} \times \mathbf{M}(\mathbf{r}) \\ &= M\delta(z)\{\Theta(w/2+x)\Theta(w/2-x)[\delta(w/2+y)-\delta(w/2-y)]\hat{\mathbf{x}} \\ &\quad - \Theta(w/2+y)\Theta(w/2-y)[\delta(w/2+x)-\delta(w/2-x)]\hat{\mathbf{y}}\}.\end{aligned} \tag{A.1}$$

Again using the Biot-Savart law, I calculate the stray magnetic field from each edge of the square. For brevity, I show below only the contribution from the first term in Equation A.1, corresponding to the bottom edge of the square:

$$\begin{aligned}B_z^{\text{bottom}}(x,y,z_0) &= \frac{\mu_0 M}{4\pi}\int_{-w/2}^{w/2} \mathrm{d}x' \frac{y+w/2}{\left[(x-x')^2+(y+w/2)^2+z_0^2\right]^{3/2}} \\ &= \frac{\mu_0 M}{4\pi}\frac{y+w/2}{(y+w/2)^2+z_0^2}\left[\mathcal{F}_+(x,y,z_0)-\mathcal{F}_-(x,y,z_0)\right],\end{aligned}$$

where

$$\mathcal{F}_\pm(x,y,z_0) = \frac{x \pm w/2}{\sqrt{(x\pm w/2)^2+(y+w/2)^2+z_0^2}}$$

APPENDIX B

DETAILED FABRICATION PROCESSES

In this section, I provide details for fabrication processes carried out at the Cornell NanoScale Science and Technology Facility (CNF), noting the specific cleanroom tools used for each step.

B.1 Photolithography process for substrate pre-patterning

The following procedure describes the patterning of a 4-inch wafer with metal wire bonding pads and alignment marks. The individual chips diced from the resulting wafer are used as substrates for devices from graphene-based heterostructures.

- Use wafers directly as received, with no additional cleaning steps
- Resist layer 1: LOR 3A
  - Dehydrate wafers 5 min at 180 °C
  - Coat entire wafer with resist
  - Spin at 3000 rpm, 3000 rpm/s, 60 s
  - Bake 5 min at 180 °C
- Resist layer 2: S1813
  - Coat entire wafer with resist
  - Spin at 3000 rpm, 3000 rpm/s, 60 s
  - Bake 1 min at 115 °C

- Exposure
  - GCA 6300 DSW 5X g-line Wafer Stepper
  - Perform dose test to determine exposure time (base dose: 0.1 s)
- Development
  - 90 s automatic develop process with 300MIF developer (Hamatech wafer developer)
  - Descum with 200 W oxygen plasma for 1 min at room temperature (YES Asher)
- Metal evaporation
  - CVC SC-4500 "odd-hour" evaporator
  - 5 nm Ti/25 nm Au/10 nm Pt*
- Liftoff
  - Leave upside-down in bath of Microposit Remover 1165 (NMP) overnight
  - After soaking overnight, move to fresh bath
  - Sonicate in 1165 for 15 min, then isopropyl alcohol (IPA) for 15 min
  - Rinse surface of wafer thoroughly with a stream of IPA
  - Blow dry with nitrogen

*I use a relatively thin metal stack to ensure that metal layers evaporated in later fabrication steps make good electrical contact to the pre-patterned electrodes. The platinum layer is resistant to many plasma etch recipes and is included so that the devices are compatible with material restrictions for the shared plasma etch tools.

  - Descum with 200 W oxygen plasma for 1 min at room temperature (YES Asher)

- Dicing
  - Spin a protective S1813 resist layer (2000 rpm, 1000 rpm/s, 60 s)
  - Softbake resist at 90 °C for 1 min
  - Dice in DISCO DAD3240 dicing saw using "all-purpose" blade

- Final cleaning steps
  - Soak each chip in acetone for a few hours to dissolve resist
  - Rinse in IPA and blow dry with nitrogen
  - Descum with 200 W oxygen plasma for 1 min at 80 °C (YES Asher)

B.2 Graphene fabrication steps

The following steps describe the fabrication of devices from graphene-based heterostructures on substrates with pre-patterned alignment marks and wire bonding pads.

- Optional: metal top gate
  - Spin 495 PMMA 4 % in anisole at 2000 rpm, 1000 rpm/s, 60 s
  - Bake 2 min at 170 °C
  - Spin 950 PMMA 2 % in MIBK at 2000 rpm, 1000 rpm/s, 60 s
  - Bake 6 min at 170 °C

  - Expose metal top gate pattern at 20 kV, 320 $\mu C\,cm^{-2}$ (Nabity/NPGS e-beam system)
  - Develop 1 min in refrigerated 3:1 DI:IPA mixture, rinse quickly in IPA, and blow dry with nitrogen.
  - Descum with 200 W oxygen plasma for 1 min at 80 °C (YES Asher)
  - Evaporate 5 nm Ti/30 nm Au/10 nm Pt (typical) using e-beam evaporation (Sharon evaporator or Odd-hour evaporator)
  - Soak in acetone for a few hours, squirt with acetone from bottle to help complete liftoff
  - Rinse in IPA and blow dry with nitrogen

- Etching device shape
  - Spin 495 PMMA 4 % in anisole at 2000 rpm, 1000 rpm/s, 60 s
  - Bake 6 min at 170 °C
  - Optional: spin and bake second layer of 950 PMMA resist as described above
  - Expose metal top gate pattern at 20 kV, 300 $\mu C\,cm^{-2}$ (Nabity/NPGS e-beam system)
  - Descum with 200 W oxygen plasma for 1 min at 80 °C (YES Asher)
  - Etch for ~1-2 min with $CHF_3/O_2/Ar$ (20/10/10 sccm) inductively coupled plasma at 10 mTorr, 30 W ICP, 10 W RF (Trion etcher)
  - Descum with 200 W oxygen plasma for 1 min at 80 °C (YES Asher)
  - Soak in acetone for 5 min, rinse in IPA and blow dry with nitrogen

- Metal edge contacts

- Spin 495 PMMA 4 % in anisole at 2000 rpm, 1000 rpm/s, 60 s
- Bake 2 min at 170 °C
- Spin 950 PMMA 2 % in MIBK at 2000 rpm, 1000 rpm/s, 60 s
- Bake 6 min at 170 °C
- Expose metal contact pattern at 20 kV, 320 $\mu C\,cm^{-2}$ (Nabity/NPGS e-beam system)
- Develop 1 min in refrigerated 3:1 DI:IPA mixture, rinse quickly in IPA, and blow dry with nitrogen.
- Descum with 200 W oxygen plasma for 1 min at 80 °C (YES Asher)
- Evaporate 3 nm Cr/80 nm Au (typical) using e-beam evaporation (Sharon evaporator)
- Soak in acetone for a few hours, squirt with acetone from bottle to help complete liftoff
- Rinse in IPA and blow dry with nitrogen

B.3 Xenon difluoride etching for graphene/hBN heterostructures

Xenon difluoride (XeF_2) is most commonly used to isotropically etch silicon, as discussed in Section 2.4.2. This technique is also useful for selectively etching hBN layers in hBN/graphene/hBN heterostructures. Upon exposure to XeF_2 vapor, the top hBN layer reacts to form a volatile byproduct and is completely removed, while the graphene layer becomes fluorinated and acts as an etch

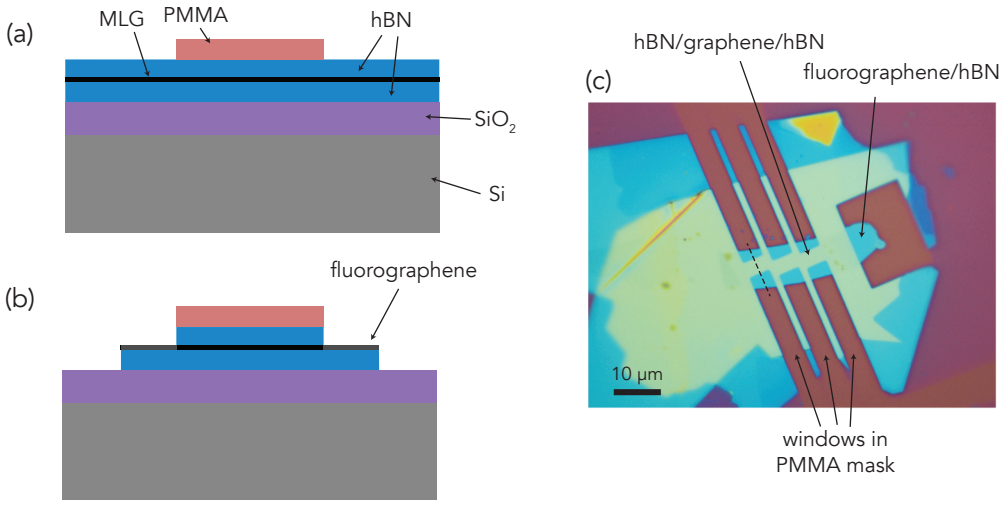

Figure B.1: Schematic cross-section of an hBN/graphene/hBN stack (a) just prior to XeF_2 exposure (b) after XeF_2 exposure. (c) Optical image of an XeF_2-etched device after PMMA removal. Cross sections in (a) and (b) are along the dashed line.

stop for the underlying hBN layer [183]. Electrical contacts made to the fluorographene demonstrate a low contact resistance and can be deposited using the same resist mask, resulting in high-quality devices [183]. Interestingly, upon exposure to XeF_2, bilayer graphene on SiO_2 becomes insulating (both layers become fluorinated) while bilayer graphene on hBN remains conducting (only the top layer becomes fluorinated) [184]. Thermal annealing may be effective in defluorinating graphene if compatible with the other materials involved in the structure [185].

I use XeF_2 etching to expose a fluorographene surface and fabricate structures on top of the exposed surface, in attempt to effectively transfer strain into graphene (see Section 6.5). Figure B.1 illustrates the general XeF_2 etching process using an example device with an SiO_2/Si substrate, detailed below:

- Pattern windows in a PMMA mask using electron-beam lithography; the

XeF_2 process only acts on the exposed regions

- Run a series of 10-second XeF_2 cycles at a vapor pressure of 1.5 Torr in a Xactix xenon difluoride etcher
  - The hBN flakes typically start etching after 5-6 cycles
  - Use an attached stereo microscope to directly monitor the color of the hBN flakes to be etched, and stop the etch when the color stops changing
  - If target hBN flakes are difficult to monitor, exfoliate hBN onto a dummy silicon substrate, find a flake of the same thickness as the target flake, and monitor its thickness to judge the etch progress
- Soak in acetone to remove PMMA resist. Rinse in IPA and blow dry with nitrogen.

The presence of Si in the etching chamber is necessary for effective hBN etching, as it is likely the reaction between XeF_2 and hBN requires an intermediate step involving Silicon [185]. When running the XeF_2 etch process on devices fabricated on polyimide substrates, I observe effectively zero etch rate unless a bare piece of Si is present within the chamber nearby the sample. Finally, I note that exposure to XeF_2 appears to slightly etch polyimide substrates, but the etch rate should be more carefully investigated.

B.4 Crosslinked PMMA

When exposed to high electron-beam doses, PMMA resist (ordinarily a positive resist) becomes crosslinked and acts as a negative resist [186]. Crosslinked

PMMA is chemically resistant to acetone (the solvent normally used to remove PMMA) and in principle allows the simultaneous patterning of negative and positive lithographic features using the same resist layer. In graphene devices, crosslinked PMMA most often serves a specialized purpose in the final device architecture, rather than serving as a lithographic mask. For example, in Ref. [187], an insulating "bridge" of crosslinked PMMA enables the fabrication of a metal top gate to an encapsulated graphene device, avoiding an electrical short between the top gate and graphene layer. Alternatively, in Ref. [173], crosslinked PMMA strips effectively clamp graphene flakes to a micromachined strain apparatus.

I include crosslinked PMMA in the design of Device B in Figure 6.7 and in the proposed device design in Figure 6.9, taking inspiration from Ref. [173]. Fabrication of crosslinked PMMA structures:

- Spin PMMA 950 M2 at 2000 rpm (for 75 nm thickness) and bake at 170 °C for 6 min (other standard recipes yielding thicker films should also work)
- Expose using Nabity e-beam system at 10 000 $\mu C\,cm^{-2}$
- Dissolve unexposed PMMA using acetone, leaving behind crosslinked structures. Rinse in IPA and blow dry with nitrogen.
- Crosslinked structures are meant to be permanent, but can likely be removed using oxygen plasma etching

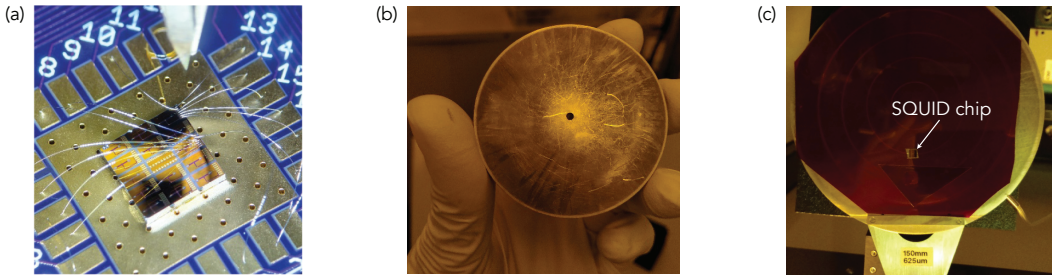

Figure B.2: (a) Wire-bonded SQUID chip on testing PCB. (b) Flat-surfaced spin chuck. (c) Stepper chuck with blocked vacuum ports.

B.5 SQUID deep etch process

The following sections describe the steps necessary to deep etch SQUIDs as discussed in Section 2.4.1. The procedure below works in principle, but it is not yet a "tried and true" process.

Preparing SQUIDs for testing

Characterization of the noise in SQUIDs is outside the scope of this dissertation, but I would like to mention nevertheless the steps necessary to enable deep etching after SQUID testing:

- Dissolve photoresist from SQUID chips (if present) in acetone. Rinse in a stream of isopropyl alcohol (IPA) and blow dry with nitrogen.
- Inspect chips for cleanliness and soak longer in acetone if residues remain.
- Mount SQUIDs onto a printed circuit board (PCB) for testing with a small amount of GE varnish (Figure B.2(a)). Let dry at room temperature.
- Make wire bond connections using lowest possible power*, preferring

*For a WestBond 747630E wedge bonder, power 100, time 15, low force.

SQUIDs with bond pads near the border of the chip.

- After testing SQUIDs, slowly remove wire bonds with tweezers to minimize the size of the remaining wire bond foot.
- Remove SQUIDs from the PCB and dissolve GE varnish thoroughly in acetone, followed again by an IPA rinse and nitrogen blow dry.

Resist spinning

- Use a flat-surfaced spin chuck with vacuum port smaller than the size of the chip (Figure B.2(b)).
- Blow off the surface of the chip with nitrogen before spinning resist.
- Carefully place a small drop of Microposit SC1827 photoresist onto the chip surface, avoiding spillage.
- Spin using a two stage recipe:
  - 2000 rpm, 1000 rpm/s, 10 s (to spread out resist)
  - 10 000 rpm, 30 000 rpm/s, 3 s (to "fling off" the edge bead)
- Use a swab slightly dampened with acetone to clean the back side of the chip. Avoid acetone wicking to the top surface of the chip.
- Check resist uniformity before baking. If resist quality is visibly unacceptable, clean chip in acetone/IPA and re-spin the resist.
- Bake at 90 °C for 2 min. This softbake recipe avoids excessive heating in consideration of the possible thermal budget of the process.
- Check resist and edge bead thickness. Typical resist thickness is ~2.3 µm, with a ~3-5 µm thick edge bead of typical width ~200 µm. The thick resist layer is necessary to enable clean removal post-etching (see below).

Exposure in GCA 6300 ("5x") *g*-line stepper

- Use the "150 mm, 625 µm" chuck. The SQUID chips are 675 µm thick, and the chuck accommodates samples with thickness 625 ± 100 µm.
- Position the chip on top of a vacuum ring near the bottom of the chuck, and block all other vacuum rings and ports with Rubylith masking film (Figure B.2(c)).
- Align manually to alignment marks near the bottom edge of the chip.
- Due to the small size of the sample, auto-focus errors are common. However, the exposure usually works, especially if an exposure with failed auto-focusing directly follows an exposure that succeeded at auto-focusing.

Development

- Do not perform a post-exposure bake. This causes the thick parts of the resist to "bubble up" and inhibits proper development.
- Develop in AZ 726 MIF for 90 seconds with mild agitation (shaking chip every ~20 s).
- Rinse in a stream of DI water and blow dry with nitrogen.
- If pattern is unacceptable, remove resist with Microposit Remover 1165 for 20 min, thoroughly rinse in IPA, blow dry with nitrogen, and re-pattern.

Etching

- Descum with 200 W oxygen plasma for 1 min at room temperature (YES Asher)

- Oxide etch (through 1100 nm of various SiO_2 and SiN_x layers)
  - Clean chamber with oxygen plasma for 10 min and season with etch recipe for 3 min prior to etching
  - Affix chip to a carrier wafer using COOL-GREASE (CGR7016)
  - Etch for 8 min using standard CHF_3/O_2 oxide etch (substrate cooled to 10 °C)
  - Clean chamber with oxygen plasma for 8 min after etching
- Deep etch for 25 loops in Plasma-Therm Versaline etcher using standard silicon etch (Bosch process)
  - Affix chip to a carrier wafer using COOL-GREASE (CGR7016)
  - Ensure resist covers all metal features; the only exposed material should be silicon
- Descum with 200 W oxygen plasma for 1 min at room temperature (YES Asher)

Resist removal

The etch process damages the top portion of the resist, making chemical removal more difficult. Using a thick resist layer described above allows liftoff of the damaged resist layer via dissolution of the lower part of the resist.

- Soak in 1165 for ~20 min with chips oriented resist side down (to avoid redeposition of the damaged resist layer).
- Sonicate in Microposit Remover 1165 for ~5-10 min.
- Rinse in IPA, blow dry with nitrogen

Dicing

- Spin Microposit S1813 photoresist using standard spin recipe (2000 rpm, 1000 rpm/s, 60 s). Thickness is not crucial here.
- Soft-bake resist at 90 °C for 1 min.
- Mount chip to white UV-sensitive dicing tape on a wafer frame. Press firmly on the back side of the tape to promote adhesion
- Place wafer frame in DISCO DAD3240 dicing saw with 30 µm diameter "silicon only" blade.
- Manually align dicing blade to dicing guides between individual SQUIDs and dice one cut at a time to ensure accuracy.
- Remove each individual SQUID and mount to a wafer frame with white dicing tape as before.
- Carefully align blade to dice diagonally through the deep-etched trench to create a new chip corner near the pickup loop, as in Figure 2.5(e).
- Dissolve resist in 1165 for ~5 min, rinse in IPA, and blow dry. Be careful not to damage the newly diced tip.

B.6 Graphene Hall sensor deep etch process

Like the above deep etch recipe for SQUIDs, the following baseline process describes steps that create a plateau around an existing finished graphene-based Hall sensor (see Chapter 3 and Chapter 4).

Oxide etch mask patterning

- Resist stack for ~1500 nm total
  - Spin 495 PMMA 8 % in anisole at 2000 rpm, 1000 rpm/s, 60 s
  - Bake 2 min at 170 °C
  - Spin 495 PMMA 8 % in anisole at 2000 rpm, 1000 rpm/s, 60 s
  - Bake 6 min at 170 °C
- Expose oxide etch pattern at 20 kV, 300 $\mu C\,cm^{-2}$ (Nabity/NPGS e-beam system)
- Develop 1 min in refrigerated 3:1 DI:IPA mixture, rinse quickly in IPA, and blow dry with nitrogen.

Oxide etch

- Descum with 200 W oxygen plasma for 1 min at 80 °C (YES Asher)
- Etch in 2-3 100 s steps with $CHF_3/CF_4/Ar$ (28/9/9 sccm) inductively coupled plasma at 20 °C, 30 mTorr, 500 W ICP, 50 W RF (Trion etcher). This recipe initially has excellent selectivity towards PMMA resist, but heats up the chip substantially, worsening the selectivity towards resist over time. Take out the wafer between runs to inspect etch progress and cool sample before the next step.
- Descum with 200 W oxygen plasma for 1 min at 80 °C (YES Asher).
- Soak in acetone for 5 min, rinse in IPA and blow dry with nitrogen.

Silicon etch mask patterning

- Resist stack for ~1500 nm total
  - Spin 495 PMMA 8 % in anisole at 2000 rpm, 1000 rpm/s, 60 s
  - Bake 2 min at 170 °C
  - Spin 495 PMMA 8 % in anisole at 2000 rpm, 1000 rpm/s, 60 s
  - Bake 6 min at 170 °C
- Expose silicon etch pattern at 20 kV, 300 µC cm^{-2} (Nabity/NPGS e-beam system)
- Wait to develop until after dicing. The undeveloped resist acts as a protective mask during dicing.

Dicing

- Mount chip to white UV-sensitive dicing tape on a wafer frame. Press firmly on the back side of the tape to promote adhesion.
- Place wafer frame in DISCO DAD3240 dicing saw with 30 µm diameter "silicon only" blade.
- Manually align dicing blade and dice chips as in Figure 2.6.
- Develop resist 1 min in refrigerated 3:1 DI:IPA mixture, rinse quickly in IPA, and blow dry with nitrogen. Be careful not to damage the newly diced tip.

XeF_2 silicon etch

- Etch using XeF_2 in batches of 10 cycles, 10 s each at 1.5 mTorr (Xactix etcher). Inspect etch progress between batches. Decrease number of cycles per batch as undercut front approaches the device (see Section 2.4.2).
- Soak in acetone for 5-10 min, rinse in IPA and blow dry with nitrogen

APPENDIX C

APPENDICES FOR CHAPTER 4

C.1 Charging models at low carrier density

For measurements of Hall sensors under a small ac bias current as discussed in Chapter 4, applying the relationship $n = 1/(eR_H)$ independently for electron and hole doping and extrapolating n to zero reveals that electrons and holes appear to reach charge neutrality at different V_g (see Figure 4.1(d), upper axis). This is consistent with non-constant contributions to the charging behavior of the graphene sheet from the quantum capacitance and/or charge traps, which become significant because of the large gate capacitance and small charge inhomogeneity [89, 93, 94]. Figure C.1(a) illustrates the energy band diagram for the gated graphene sheet. Here, the difference in electrochemical potential V_g between the gate electrode and the graphene sheet is a sum of the electric potential ϕ and the shift in Fermi level E_F due to the induced carriers [188]:

$$eV_g = e\phi + E_F.$$

Taking the derivative with respect to the total induced charge $Q = ne$ reveals that the total capacitance C_{tot} is a series combination of the gate capacitance C_g and quantum capacitance C_q [188]:

$$\frac{1}{C_{tot}} = \frac{dV_g}{dQ} = \frac{d\phi}{dQ} + \frac{1}{e^2}\frac{dE_F}{dn} = \frac{1}{C_g} + \frac{1}{C_q}.$$

Here, $C_g = n_g e/V_g$ and $C_q \equiv e^2 D(E)$, where $D(E) = \frac{2}{\hbar v_F}\sqrt{\frac{|n|}{\pi}}$ is the density of states for graphene [89, 94, 188, 189]. Integrating this expression yields the following expression for V_g:

$$V_g = en\left[\frac{1}{C_g} + \frac{2}{C_q}\right].$$

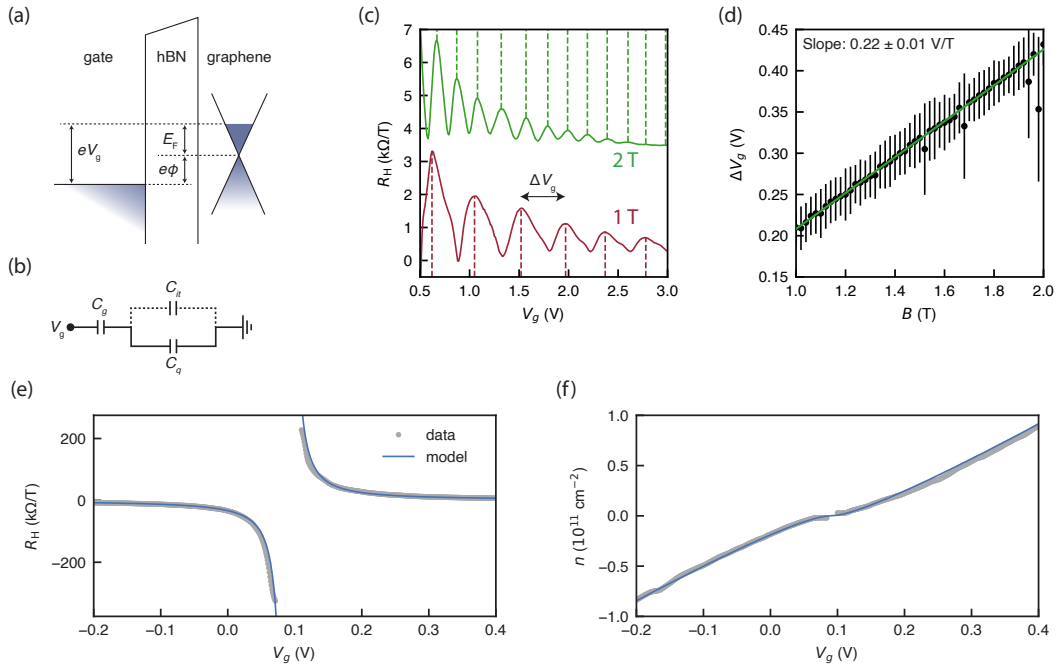

Figure C.1: (a) Energy-band diagram for the device with gate voltage V_g, electric potential ϕ, and Fermi level E_F. (b) Capacitor model for the system, including geometric gate capacitance C_g, quantum capacitance C_q, and interface trap capacitance C_t. (c) R_H versus V_g at 1 T (upper, offset for clarity) and 2 T (lower). (d) Linear fit to quantum oscillation spacing ΔV_g as a function of B. (e) Quantum capacitance model fit to the measured R_H from Figure 4.1(d). (f) Nonlinear relationship between n and V_g calculated directly from R_H.

Here, the linear dispersion in graphene leads to a factor of 2 in the second term*, which is absent in the usual expression derived for two-dimensional electron systems with quadratic dispersion [89]. Accounting for a voltage offset of the CNP (V_g^0) and defining $n_q \equiv \frac{\pi}{2}\left(\frac{C_g \hbar v_F}{e^2}\right)^2$ results in an expression for n as a function of V_g.

$$n(V_g) = \frac{C_g(V_g - V_g^0)}{e} - \mathrm{sgn}(V_g - V_g^0) n_q \left(\sqrt{1 + 2\frac{C_g|V_g - V_g^0|}{e n_q}} - 1 \right). \tag{C.1}$$

For $n \gg n_q$, the quantum capacitance term is negligible, allowing calibra-

*This factor of 2 is missing from a number of articles (including Refs [89, 189]) and has led to small interpretation errors therein.

tion of C_g at large n via measurement of the oscillations in R_H in the quantum Hall regime at large magnetic field. The gate voltage spacing ΔV_g of quantum oscillations follows the relationship

$$C_g \Delta V_g = \frac{4e^2}{h} B,$$

where ΔV_g is the oscillation period and e^2/h is the conductance quantum [83]. The quantum oscillations in this device (Figure C.1(c,d)) suggest $C_g = 0.0712 \pm 0.0006\,\mathrm{F\,cm^{-2}}$. With this value for C_g and the CNP voltage offset $V_g^0 = 0.09$ V, I extracted $n_q = (1.18 \pm 0.06) \times 10^{10}\,\mathrm{cm^{-2}}$ from fitting the measurement in Figure 4.1(d) to Equation C.1.

The fitted value of n_q is an order of magnitude larger than the estimate $n_q = \frac{\pi}{2}\left(\frac{C_g \hbar v_F}{e^2}\right)^2 \approx 2 \times 10^9\,\mathrm{cm^{-2}}$. This may suggest the presence of charge traps that add an additional constant capacitance contribution C_t in parallel with C_q (Figure C.1(b)) [94]. These charge traps can be incorporated unintentionally during device fabrication and most likely reside either within the hBN layer or at the edges of the graphene sheet [94, 190].

C.2 Carrier density gradient under large current bias

To understand the effect of a large dc bias current to the transport properties of my Hall sensors, I consider an $L \times L$ square device as in Figure C.2(a) with one contact at potential $V_{2p} = IR_{2p}$, one grounded contact, and two floating contacts that measure the average Hall voltage. The potential $\psi(x)$ varies with position along the length of the device, leading to electron (n_g) and hole (p_g) densities

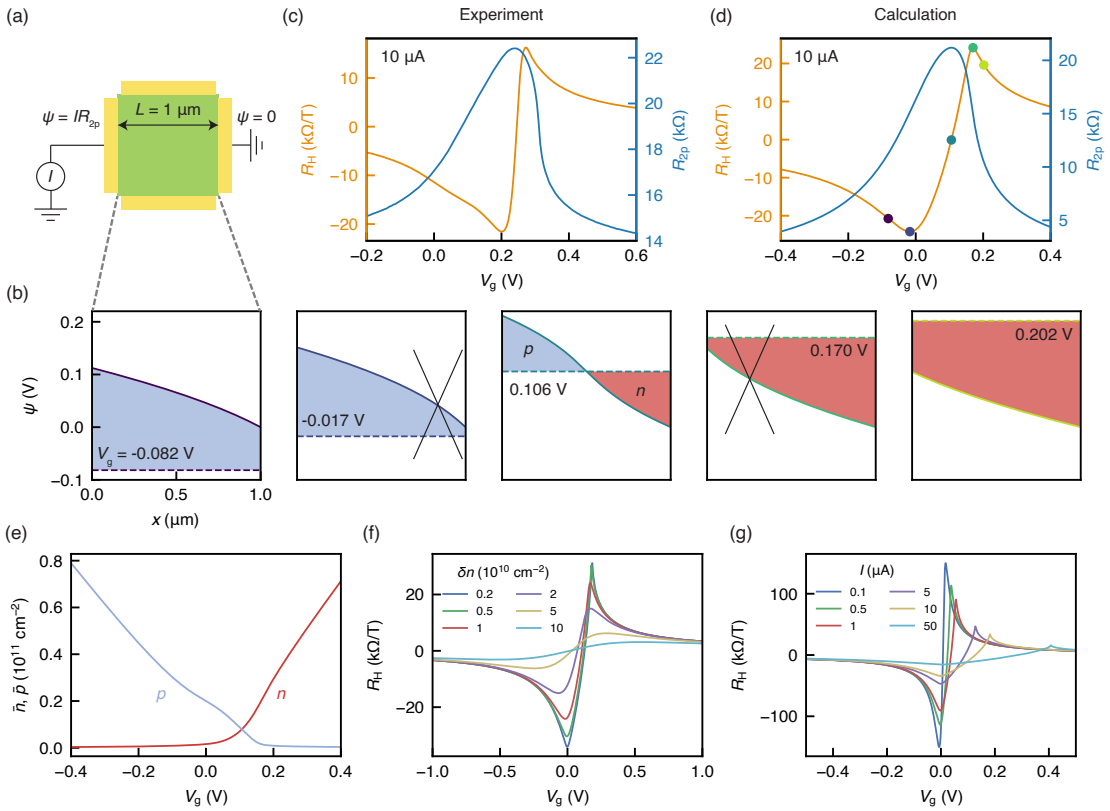

Figure C.2: (a) Schematic of the model device. (b) Potential drop along the device corresponding to the gate voltages marked in (d). The carrier density (shading) is related to the difference between $\psi(x)$ and V_g (dashed line). (c) Measured and (d) calculated R_H and R_{2p} under 10 μA dc bias current. The calculation uses $\mu = 20\,000\,\mathrm{cm^2\,V^{-1}\,s^{-1}}$, $C_g = 0.03\,\mathrm{F\,cm^{-2}}$, and $\delta n = 10^{10}\,\mathrm{cm^{-2}}$. (e) Calculated average electron and hole densities in the Hall cross. (f) Calculated charge inhomogeneity and (g) bias current dependence of R_H.

that also vary with x:

$$n_g(x) = \frac{C_g}{e}[V_g - \psi(x)] \qquad p_g(x) = \frac{C_g}{e}[\psi(x) - V_g], \tag{C.2}$$

In most transport experiments under small current bias, $V_{2p} \ll V_g$ and the carrier densities are approximately constant. Here, with $V_{2p} \sim 100\,\mathrm{mV}$, the carrier density gradient along the device becomes significant.

Accounting for charge inhomogeneity δn and applying Ohm's law, the po-

tential gradient along the device is

$$\frac{\partial \psi}{\partial x} = -\frac{I\rho(x)}{L} = -\frac{I}{Le\mu\sqrt{\frac{C_g^2}{e^2}[V_g - \psi(x)]^2 + \delta n^2}},$$

where μ is the carrier mobility [191]. Solving this differential equation numerically reveals that the potential $\psi(x)$ drops nonlinearly for small V_g (Figure C.2(b)). Equation C.2 then yields the electron and hole densities as a function of position, and the corresponding value of the average Hall coefficient is given by [94]:

$$R_H = \frac{1}{e}\frac{\bar{n} - \bar{p}}{(\bar{n} + \bar{p})^2},$$

where $\bar{n}$ and $\bar{p}$ are the average electron and hole densities (Figure C.2(e)). The calculated R_H and R_{2p} curves (Figure C.2(d,f,g)) demonstrate a marked electron-hole asymmetry, broadened Dirac peak, and reduction of peak R_H upon increasing charge inhomogeneity or bias current. These general observations are in good agreement with the measurements in Figure C.2(c).

APPENDIX D

APPENDICES FOR CHAPTER 5

D.1 Berry curvature and orbital magnetic moment

Here, I show how the conventional definitions of the Berry curvature $\boldsymbol{\Omega}_n$ and orbital magnetic moment $\boldsymbol{\mu}_n$ can be transformed from expressions involving momentum-space derivatives of the eigenstates of the Hamiltonian to expressions involving derivatives of the Hamiltonian itself, which are more convenient to work with [192, 193]. I abbreviate the momentum-space derivatives as $\boldsymbol{\nabla} \equiv \boldsymbol{\nabla}_{\mathbf{k}}$ and write the eigenstate for band n as $|n\rangle$. The conventional definitions of the Berry curvature and orbital magnetic moment are [108]:

$$\boldsymbol{\Omega}_n = \boldsymbol{\nabla} \times (i \langle n|\boldsymbol{\nabla} n\rangle) = i \langle \boldsymbol{\nabla} n| \times |\boldsymbol{\nabla} n\rangle$$

$$\boldsymbol{\mu}_n = -i\frac{e}{2\hbar} \langle \boldsymbol{\nabla} n| \times (H - E_n)|\boldsymbol{\nabla} n\rangle \,.$$

Inserting a complete set of eigenstates,

$$\begin{aligned}
\boldsymbol{\Omega}_n &= i \sum_m \langle \boldsymbol{\nabla} n|m\rangle \times \langle m|\boldsymbol{\nabla} n\rangle \\
\boldsymbol{\mu}_n &= -i\frac{e}{2\hbar} \sum_m \langle \boldsymbol{\nabla} n|m\rangle \times \langle m|(H - E_n)|\boldsymbol{\nabla} n\rangle \\
&= -i\frac{e}{2\hbar} \sum_m (E_m - E_n) \langle \boldsymbol{\nabla} n|m\rangle \times \langle m|\boldsymbol{\nabla} n\rangle \,.
\end{aligned}$$

This can be simplified using the identity* $\langle m|\nabla n\rangle \equiv \langle m|\nabla H|n\rangle / (E_n - E_m)$, and the expressions become:

$$\boldsymbol{\Omega}_n = i \sum_{m \neq n} \frac{\langle n|\nabla H|m\rangle \times \langle m|\nabla H|n\rangle}{(E_n - E_m)^2}$$
$$\boldsymbol{\mu}_n = i \frac{e}{2\hbar} \sum_{m \neq n} \frac{\langle n|\nabla H|m\rangle \times \langle m|\nabla H|n\rangle}{E_n - E_m}.$$

Finally, because the Hamiltonian is two-dimensional, the numerator only involves the k_x and k_y derivatives of the Hamiltonian and simplifies to† [117]:

$$\Omega_n^z(\mathbf{k}) = -2 \operatorname{Im} \sum_{m \neq n} \frac{\langle n|\partial_{k_x} H|m\rangle \langle m|\partial_{k_y} H|n\rangle}{(E_n - E_m)^2}$$
$$\mu_n^z(\mathbf{k}) = -\frac{e}{\hbar} \operatorname{Im} \sum_{m \neq n} \frac{\langle n|\partial_{k_x} H|m\rangle \langle m|\partial_{k_y} H|n\rangle}{E_n - E_m}.$$

We use these expressions in Section 5.3 to avoid taking numerical derivatives of the eigenstates.

*The eigenvalue equation for eigenstate $|n\rangle$ is $H|n\rangle = E_n|n\rangle$. Taking the gradient and calculating the inner product with an orthogonal eigenstate $|m\rangle$ (such that $\langle m|n\rangle = 0$) yields a convenient expression for $\langle m|\nabla n\rangle$:

$$(\nabla H)|n\rangle + H|\nabla n\rangle = (\nabla E_n)|n\rangle + E_n|\nabla n\rangle$$
$$\langle m|\nabla H|n\rangle + E_m \langle m|\nabla n\rangle = (\nabla E_n)\langle m|n\rangle + E_n \langle m|\nabla n\rangle$$
$$\langle m|\nabla n\rangle = \frac{\langle m|\nabla H|n\rangle}{E_n - E_m}$$

†For a Hamiltonian independent of k_z,

$$(\langle n|\nabla H|m\rangle \times \langle m|\nabla H|n\rangle)_z = \langle n|\partial_{k_x} H|m\rangle \langle m|\partial_{k_y} H|n\rangle - \langle n|\partial_{k_y} H|m\rangle \langle m|\partial_{k_x} H|n\rangle .$$

The second term is the complex conjugate of the first term, and for any complex quantity ζ and its complex conjugate $\zeta^\dagger$, $\zeta - \zeta^\dagger = 2i \operatorname{Im}(\zeta)$. Therefore, the expression becomes:

$$(\langle n|\nabla H|m\rangle \times \langle m|\nabla H|n\rangle)_z = 2i \operatorname{Im} \langle n|\partial_{k_x} H|m\rangle \langle m|\partial_{k_y} H|n\rangle$$

D.2 Magnetic moment for effective two-band BLG Hamiltonian

To capture intuitively the dependence of the orbital magnetic moment and Berry curvature on the band gap, parameterized by the interlayer asymmetry Δ, I consider a simpler model for BLG in the absence of strain. A low-energy two-band effective Hamiltonian for electronic states at location $\mathbf{q} = (q_x, q_y)$ in momentum space relative to the K or K′ point is [116]:

$$H = -\frac{\hbar^2}{2m}\begin{pmatrix} 0 & (q_x - iq_y)^2 \\ (q_x + iq_y)^2 & 0 \end{pmatrix} + \frac{\Delta}{2}\begin{pmatrix} 1 & 0 \\ 0 & -1 \end{pmatrix},$$

where $m = \gamma_1/2v^2$ is an effective mass, with $v = (\sqrt{3}/2)a\gamma_0/\hbar$. This Hamiltonian only includes the hopping elements γ_0 and γ_1 (Table 5.1), therefore maintaining electron-hole symmetry and lacking trigonal warping. Diagonalizing this Hamiltonian leads to symmetric parabolic energy bands with a mass gap Δ:

$$E_n(\mathbf{k}) = \pm\sqrt{\left(\frac{\hbar^2|\mathbf{k}|^2}{2m}\right)^2 + \left(\frac{\Delta}{2}\right)^2}.$$

For any two-band model with particle-hole symmetry [109],

$$\mu_n^z(\mathbf{k}) \equiv \frac{e}{\hbar}E_n(\mathbf{k})\Omega_n^z(\mathbf{k})$$

and Equation 5.4 becomes

$$\mathcal{M}(\mathbf{k}) = \frac{e}{\hbar}\mu\Omega_n^z(\mathbf{k}),$$

where μ is the chemical potential. Using an expression for the Berry curvature reported previously [113, 194, 195], I obtain

$$\mathcal{M}(\mathbf{k}) = \mp\frac{e\hbar}{2m}\frac{\mu\Delta\sqrt{E_n(\mathbf{k})^2 - \left(\frac{\Delta}{2}\right)^2}}{E_n(\mathbf{k})^3},$$

where the upper (lower) sign corresponds to the K (K′) valley. The magnetic moment is zero at the valley center and is distributed in a finite-width ring at finite momentum

$$|\mathbf{k}^*| = \sqrt{\frac{m}{\sqrt{2}}}\frac{\Delta}{\hbar}$$

surrounding the valley center. At this momentum, the magnetic moment reaches a maximum value of

$$\mathcal{M}^{\max} = \mp\frac{8}{3\sqrt{3}}\frac{e\hbar}{2m}\frac{\mu}{\Delta}$$

which depends on the ratio of the chemical potential to interlayer asymmetry (μ/Δ). This expression implies that systems with smaller Δ will exhibit stronger effects originating from the valley magnetic moment.

D.3 Relationship between gate voltage and model parameters

In the calculations discussed in Chapter 5, I fix the interlayer asymmetry Δ and chemical potential μ and remap them to corresponding related values of displacement field D and carrier density n using Equation 5.8 and Equation 5.9. The latter parameters are electrostatically tunable via application of gate voltage. Considering the device structure in Figure 5.8(a-b), the displacement field D is essentially a difference between top and bottom gate voltages V_t and V_b, while the carrier density n is essentially a sum of the gate voltages. Accounting for different dielectric constants (ε_t, ε_b) and dielectric layer thickness (d_t, d_b) [112]:

$$D = \frac{\varepsilon_\mathrm{t}\varepsilon_0 V_\mathrm{t}}{d_\mathrm{t}} - \frac{\varepsilon_\mathrm{b}\varepsilon_0 V_\mathrm{b}}{d_\mathrm{b}}$$

$$n_\mathrm{tot}e = (n_\mathrm{t} + n_\mathrm{b})e = \frac{\varepsilon_\mathrm{t}\varepsilon_0 V_\mathrm{t}}{d_\mathrm{t}} + \frac{\varepsilon_\mathrm{b}\varepsilon_0 V_\mathrm{b}}{d_\mathrm{b}}.$$

Solving for the gate voltages directly, I arrive at the following relationships:

$$\frac{\varepsilon_\mathrm{t} V_\mathrm{t}}{d_\mathrm{t}} = \frac{1}{2}\frac{\varepsilon_0 \Delta}{de} + n_\mathrm{b} e$$

$$\frac{\varepsilon_\mathrm{b} V_\mathrm{b}}{d_\mathrm{b}} = -\frac{1}{2}\frac{\varepsilon_0 \Delta}{de} + n_\mathrm{t} e,$$

where n_t and n_b are the carrier density on each layer (labeled n_1 and n_2 previously). These expressions are useful for comparing the expected magnitude of the magnetoelectric susceptibility calculated here to that obtained experimentally under equivalent conditions. The reverse problem (determining Δ, μ from gate voltages V_t, V_b) is less approachable, since the calculation of n_t, n_b requires integration over a Fermi surface with nontrivial geometry and topology (see Equation 5.8).

D.4 Orbital magnetization magnitude in other systems

I briefly review here the strength of orbital magnetization reported for other solid-state systems, benchmarks used in Section 5.5. The magnetoelectric effects described below are expected to be linear in both strain magnitude ε and bias current I, so I calculate the normalized magnetization $M_z/(I\varepsilon)$.

MoS_2

Kerr rotation microscopy of strained single-layer MoS_2 supported by a simple tight-binding model leads to a typical estimated $M_z \sim 4 \times 10^{-11}\,\mathrm{A}$ with current density $J \sim 10\,\mathrm{A/m}$ for a $W \sim 8\,\mu\mathrm{m}$ device under $\varepsilon \sim 0.5\,\%$ strain [122]. This is equivalent to a bias current of $I \sim 80\,\mu\mathrm{A}$ and normalized magneti-

zation $M_z/(I\varepsilon) \sim 10^{-6}\,\mathrm{A}/(\mathrm{A}\,\%)$. A follow-up study reports a maximum estimated volume magnetization per unit current density $(M_z/t)/(I/W) \sim 0.1$ for a $W \sim 12\,\mu\mathrm{m}$ device with thickness $t = 0.67$ nm under $\varepsilon \sim 1\,\%$ strain [122]. This corresponds to a normalized area magnetization $M_z/(I\varepsilon) = 0.1(t/W)/(1\,\%) = 5 \times 10^{-6}\,\mathrm{A}/(\mathrm{A}\,\%)$.

$NbSe_2$

A tight-binding model for strained monolayer $NbSe_2$ [160] predicts $M_z \sim 10^4\,\mu_\mathrm{B}/\mu\mathrm{m}^2 \sim 10^{-7}\,\mathrm{A}$ for $\varepsilon = 5\,\%$ and $\mathcal{E} = 10^4\,\mathrm{V\,m^{-1}}$. Presuming a resistivity $\rho \sim 1\,\mathrm{k}\Omega$ and device length $L \sim 10\,\mu\mathrm{m}$, this corresponds to an approximate bias current $I \sim 100\,\mu\mathrm{A}$ and normalized magnetization $M_z/(I\varepsilon) \sim 2 \times 10^{-4}\,\mathrm{A}/(\mathrm{A}\,\%)$.

Twisted bilayer graphene

There are also three established predictions for the strength of orbital magnetization in twisted bilayer graphene (TBG). In Ref. [133], the authors consider a model describing TBG with a relative rotation of 1.2° between the layers and with the symmetry between the layers further broken by a hexagonal boron nitride substrate. For 0.1 % uniform uniaxial strain and $\mathcal{E} = 10^4\,\mathrm{V\,m^{-1}}$, the authors estimate $M_z \sim 2 \times 10^4\,\mu_\mathrm{B}/\mu\mathrm{m}^2 \sim 2 \times 10^7\,\mathrm{A}$. Using $\rho \sim 1\,\mathrm{k}\Omega$ and $L \sim 10\,\mu\mathrm{m}$, the normalized magnetization is $M_z/(I\varepsilon) \sim 4 \times 10^{-4}\,\mathrm{A}/(\mathrm{A}\,\%)$.

Experimental studies of TBG also report a spontaneous orbital magnetization in the absence of electric current. In a scanning magnetometry experiment, magnetic images of a TBG system reveal a spontaneous orbital magnetization

appearing in the absence of electric current [13]. The estimated magnitude of the orbital magnetic moment is $4\,\mu_B$ per moiré unit cell, or $M_z \sim 3 \times 10^4\,\mu_B/\mu m^2$ [13]. Finally, scanning tunneling spectroscopy on TBG with $0.38\,\%$ heterostrain between the layers leads to a spontaneous orbital magnetization of estimated magnitude $15\,\mu_B$ per moiré unit cell, equivalent to $M_z \sim 10^5\,\mu_B/\mu m^2$ [196]. The magnitude of M_z in these systems is quite large, exceeding that predicted here. However, the effect in TBG is quasi-ferromagnetic and sensitive to twist angle disorder, demonstrating a hysteretic response and inhomogeneous magnetic domains upon application of an external magnetic field [13, 130, 131]. The orbital magnetization in sBLG is in principle non-hysteretic and continuously tunable through *in situ* control of the uniaxial strain and bias current, making sBLG a more desirable component for magnetic memory devices [110].

BIBLIOGRAPHY

[1] J. A. Bert, *et al.*, *Nat. Phys.* **7**, 767 (2011).

[2] J. A. Bert, *et al.*, *Phys. Rev. B* **86**, 060503 (2012).

[3] H. Noad, *et al.*, *Phys. Rev. B* **98**, 064510 (2018).

[4] S. I. Davis, *et al.*, *Phys. Rev. B* **98**, 014506 (2018).

[5] I. P. Zhang, *et al.*, *Phys. Rev. B* **100**, 024514 (2019).

[6] A. Kremen, *et al.*, *Nano Lett.* **16**, 1626 (2016).

[7] S. Wissberg, A. Frydman, B. Kalisky, *Appl. Phys. Lett.* **112**, 262602 (2018).

[8] A. Kremen, *et al.*, *Nat. Phys.* **14**, 1205 (2018).

[9] L. Thiel, *et al.*, *Science* **364**, 973 (2019).

[10] A. Jenkins, *et al.*, *Phys. Rev. Mater.* **3**, 83801 (2019).

[11] Y. Dovzhenko, *et al.*, *Nat. Commun.* **9**, 2712 (2018).

[12] E. O. Lachman, *et al.*, *Sci. Adv.* **1**, e1500740 (2015).

[13] C. L. Tschirhart, *et al.*, *arXiv:2006.08053* .

[14] K. C. Nowack, *et al.*, *Nat. Mater.* **12**, 787 (2013).

[15] A. Uri, *et al.*, *Nat. Phys.* **16**, 164 (2020).

[16] A. Uri, *et al.*, *Nature* **581**, 47 (2020).

[17] M. D. Bachmann, *et al.*, *Science* **366**, 221 (2019).

[18] A. Jenkins, *et al.*, *arXiv:2002.05065* (2020).

[19] M. J. H. Ku, *et al.*, *Nature* **583**, 537 (2020).

[20] C. Reig, S. Cardoso, S. C. Mukhopadhyay, *Giant Magnetoresistance (GMR) Sensors*, vol. 6 of *Smart Sensors, Measurement and Instrumentation* (Springer Berlin Heidelberg, Berlin, Heidelberg, 2013).

[21] J. Heremans, *J. Phys. D* **26**, 1149 (1993).

[22] G. Xiao, *Handb. Spin Transp. Magn.* (CRC Press, 2011), pp. 665–684.

[23] F. Casola, T. Van Der Sar, A. Yacoby, *Nat. Rev. Mater.* **3**, 17088 (2018).

[24] F. Yang, A. J. Kollár, S. F. Taylor, R. W. Turner, B. L. Lev, *Phys. Rev. Appl.* **7**, 034026 (2017).

[25] M. E. Huber, *et al.*, *Rev. Sci. Instrum.* **79**, 053704 (2008).

[26] C. W. Hicks, Scanning SQUID microscopy on iron pnictide and time-reversal symmetry-breaking superconductors, Ph.D. thesis, Stanford University (2009).

[27] J. R. Kirtley, *et al.*, *Rev. Sci. Instrum.* **87**, 093702 (2016).

[28] J. R. Kirtley, *et al.*, *Supercond. Sci. Technol.* **29**, 124001 (2016).

[29] C. Granata, A. Vettoliere, *Phys. Rep.* **614**, 1 (2016).

[30] D. Vasyukov, *et al.*, *Nat. Nanotechnol.* **8**, 639 (2013).

[31] Y. Anahory, *et al.*, *Nanoscale* **12**, 3174 (2020).

[32] J. Clarke, *Curr. Opin. Solid State Mater. Sci.* **2**, 3 (1997).

[33] E. F. Fleet, S. Chatraphorn, F. C. Wellstood, L. A. Knauss, S. M. Green, *Rev. Sci. Instrum.* **72**, 3281 (2001).

[34] L. Bishop-Van Horn, Z. Cui, J. R. Kirtley, K. A. Moler, *Rev. Sci. Instrum.* **90**, 063705 (2019).

[35] J. R. Kirtley, *et al.*, *Appl. Phys. Lett.* **74**, 4011 (1999).

[36] R. S. Popovic, *Hall Effect Devices* (Institute of Physics Publishing, Bristol and Philadelphia, 2004), second edn.

[37] O. Kazakova, *et al.*, *J. Appl. Phys.* **107**, 09E708 (2010).

[38] M. Kim, *et al.*, *Nat. Electron.* **2**, 457 (2019).

[39] J. R. Kirtley, *Rep. Prog. Phys.* **73**, 126501 (2010).

[40] S. J. Bending, *Adv. Phys.* **48**, 449 (1999).

[41] A. K. Geim, *et al.*, *Nature* **390**, 259 (1997).

[42] E. H. Hall, *Amer. J. Math* **2**, 287 (1879).

[43] A. K. Geim, *et al.*, *Appl. Phys. Lett.* **71**, 2379 (1997).

[44] B. T. Schaefer, *et al.*, *Nat. Commun.* **11**, 4163 (2020).

[45] J. Dauber, *et al.*, *Appl. Phys. Lett.* **106**, 193501 (2015).

[46] C. W. Hicks, L. Luan, K. A. Moler, E. Zeldov, H. Shtrikman, *Appl. Phys. Lett.* **90**, 133512 (2007).

[47] A. Sandhu, K. Kurosawa, M. Dede, A. Oral, *Jpn. J. Appl. Phys* **43**, 777 (2004).

[48] D. Collomb, P. Li, S. J. Bending, *Sci. Rep.* **9**, 14424 (2019).

[49] S. Sonusen, O. Karci, M. Dede, S. Aksoy, A. Oral, *Appl. Surf. Sci.* **308**, 414 (2014).

[50] A. Oral, *et al.*, *IEEE Trans. Magn.* **38**, 2438 (2002).

[51] G. Boero, M. Demierre, P.-A. Besse, R. Popovic, *Sensors Actuators A Phys.* **106**, 314 (2003).

[52] S. Machlup, *J. Appl. Phys.* **25**, 341 (1954).

[53] P. Karnatak, *et al.*, *Phys. Rev. Lett.* **113**, 026601 (2014).

[54] P. Dutta, P. M. Horn, *Rev. Mod. Phys.* **53**, 497 (1981).

[55] F. N. Hooge, T. G. M. Kleinpenning, L. K. J. Vandamme, *Reports Prog. Phys.* **44**, 479 (1981).

[56] J. Clarke, A. I. Braginski, *The SQUID Handbook*, vol. 1 (2005).

[57] R. H. Koch, D. P. Divincenzo, J. Clarke, *Phys. Rev. Lett.* **98**, 267003 (2007).

[58] A. A. Balandin, *Nat. Nanotechnol.* **8**, 549 (2013).

[59] T. G. M. Kleinpenning, *J. Appl. Phys.* **48**, 2946 (1977).

[60] H. Heidari, E. Bonizzoni, U. Gatti, F. Maloberti, *2014 IEEE Int. Symp. Circuits Syst.* (IEEE, 2014), pp. 678–681.

[61] Y. Yuzhelevski, M. Yuzhelevski, G. Jung, *Rev. Sci. Instrum.* **71**, 1681 (2000).

[62] M. Dede, *et al.*, *J. Nanosci. Nanotechnol.* **8**, 619 (2008).

[63] L. Wang, *et al.*, *Science* **342**, 614 (2013).

[64] L. Wang, *et al.*, *Science* **350**, 1231 (2015).

[65] E. M. Spanton, Imaging Current in Materials, Ph.D. thesis, Stanford University (2016).

[66] J. D. Jackson, *Classical Electrodynamics* (Wiley, New York, NY, 1999), third edn.

[67] P. G. Björnsson, Low-Temperature Scanning Magnetic Probe Microscopy of Exotic Superconductors, Ph.D. thesis, Stanford University (2005).

[68] D. Low, *et al.*, *arXiv:2102.09588* (2021).

[69] A. A. Zibrov, *et al.*, *Nature* **549**, 360 (2017).

[70] Y. Zeng, *et al.*, *Phys. Rev. Lett.* **122**, 137701 (2019).

[71] N. Nandi, *et al.*, *npj Quantum Mater.* **3**, 66 (2018).

[72] S. Das Sarma, E. H. Hwang, S. Kodiyalam, L. N. Pfeiffer, K. W. West, *Phys. Rev. B* **91**, 205304 (2015).

[73] A. K. Geim, I. V. Grigorieva, *Nature* **499**, 419 (2013).

[74] K. S. Novoselov, A. Mishchenko, A. Carvalho, A. H. Castro Neto, *Science* **353**, aac9439 (2016).

[75] Y. Liu, *et al.*, *Nat. Rev. Mater.* **1**, 16042 (2016).

[76] M. Yankowitz, Q. Ma, P. Jarillo-Herrero, B. J. LeRoy, *Nat. Rev. Phys.* **1**, 112 (2019).

[77] Y. Cao, *et al.*, *Nature* **556**, 43 (2018).

[78] P. Blake, *et al.*, *Appl. Phys. Lett.* **91**, 063124 (2007).

[79] Y. Huang, *et al.*, *ACS Nano* **9**, 10612 (2015).

[80] T. Taniguchi, K. Watanabe, *J. Cryst. Growth* **303**, 525 (2007).

[81] D. G. Purdie, *et al.*, *Nat. Commun.* **9**, 5387 (2018).

[82] A. C. Ferrari, D. M. Basko, *Nat. Nanotechnol.* **8**, 235 (2013).

[83] P. J. Zomer, M. H. D. Guimarães, J. C. Brant, N. Tombros, B. J. van Wees, *Appl. Phys. Lett.* **105**, 013101 (2014).

[84] K. Kim, *et al.*, *Nano Lett.* **16**, 1989 (2016).

[85] M. Lee, Ballistic conduction in graphene heterostructures, Ph.D. thesis, Stanford University (2016).

[86] F. Pizzocchero, *et al.*, *Nat. Commun.* **7**, 11894 (2016).

[87] M. J. Rooks, *et al.*, *J. Vac. Sci. Technol. B* **20**, 2937 (2002).

[88] M. Ben Shalom, *et al.*, *Nat. Phys.* **12**, 318 (2016).

[89] S. Das Sarma, S. Adam, E. H. Hwang, E. Rossi, *Rev. Mod. Phys.* **83**, 407 (2011).

[90] M. A. Stolyarov, G. Liu, S. L. Rumyantsev, M. Shur, A. A. Balandin, *Appl. Phys. Lett.* **107**, 023106 (2015).

[91] A. V. Kretinin, *et al.*, *Nano Lett.* **14**, 3270 (2014).

[92] G. Song, M. Ranjbar, R. A. Kiehl, *Commun. Phys.* **2**, 65 (2019).

[93] S. A. Thiele, J. A. Schaefer, F. Schwierz, *J. Appl. Phys.* **107**, 094505 (2010).

[94] P. Wehrfritz, T. Seyller, *2D Mater.* **1**, 035004 (2014).

[95] P. D. Welch, *IEEE Trans. Audio Electroacoust.* **15**, 70 (1967).

[96] P. Karnatak, *et al.*, *Nat. Commun.* **7**, 13703 (2016).

[97] Q. Li, E. H. Hwang, S. Das Sarma, *Phys. Rev. B* **84**, 115442 (2011).

[98] W. Zhu, V. Perebeinos, M. Freitag, P. Avouris, *Phys. Rev. B* **80**, 235402 (2009).

[99] D. Halbertal, *et al.*, *Science* **358**, 1303 (2017).

[100] W. van der Wel, C. J. P. M. Harmans, J. E. Mooij, *J. Phys. C Solid State Phys.* **21**, L171 (1988).

[101] A. Kil, R. Zijlstra, P. Koenraad, J. Pals, J. André, *Solid State Commun.* **60**, 831 (1986).

[102] S. L. Rumyantsev, *et al.*, *Appl. Phys. Lett.* **103**, 173114 (2013).

[103] V. Panchal, *et al.*, *J. Appl. Phys.* **111**, 07E509 (2012).

[104] K. Vervaeke, E. Simoen, G. Borghs, V. V. Moshchalkov, *Rev. Sci. Instrum.* **80**, 074701 (2009).

[105] B. Chenaud, *et al.*, *J. Appl. Phys* **119**, 024501 (2016).

[106] M. Bando, *et al.*, *J. Appl. Phys.* **105**, 07E909 (2009).

[107] A. H. Castro Neto, F. Guinea, N. M. R. Peres, K. S. Novoselov, A. K. Geim, *Rev. Mod. Phys.* **81**, 109 (2009).

[108] D. Xiao, M.-C. Chang, Q. Niu, *Rev. Mod. Phys.* **82**, 1959 (2010).

[109] D. Xiao, W. Yao, Q. Niu, *Phys. Rev. Lett.* **99**, 236809 (2007).

[110] E. C. Ahn, *npj 2D Mater. Appl.* **4**, 17 (2020).

[111] K. F. Mak, D. Xiao, J. Shan, *Nat. Photonics* **12**, 451 (2018).

[112] Y. Zhang, *et al.*, *Nature* **459**, 820 (2009).

[113] Y. Shimazaki, *et al.*, *Nat. Phys.* **11**, 1032 (2015).

[114] M. Sui, *et al.*, *Nat. Phys.* **11**, 1027 (2015).

[115] B. T. Zhou, K. Taguchi, Y. Kawaguchi, Y. Tanaka, K. T. Law, *Commun. Phys.* **2**, 26 (2019).

[116] E. McCann, *Phys. Rev. B* **74**, 161403 (2006).

[117] C. Moulsdale, A. Knothe, V. Fal'ko, *Phys. Rev. B* **101**, 85118 (2019).

[118] R. Battilomo, N. Scopigno, C. Ortix, *Phys. Rev. Lett.* **123**, 196403 (2019).

[119] K. F. Mak, K. L. McGill, J. Park, P. L. McEuen, *Science* **344**, 1489 (2014).

[120] J. Lee, K. F. Mak, J. Shan, *Nat. Nanotechnol.* **11**, 421 (2016).

[121] L. Li, *et al.*, *Phys. Rev. Mater.* **4**, 104005 (2020).

[122] J. Lee, Z. Wang, H. Xie, K. F. Mak, J. Shan, *Nat. Mater.* **16**, 887 (2017).

[123] J. Son, K.-H. Kim, Y. H. Ahn, H.-W. Lee, J. Lee, *Phys. Rev. Lett.* **123**, 036806 (2019).

[124] I. Polyzos, *et al.*, *Nanoscale* **7**, 13033 (2015).

[125] O. Frank, *et al.*, *ACS Nano* **4**, 3131 (2010).

[126] S.-Y. Xu, *et al.*, *Nat. Phys.* **14**, 900 (2018).

[127] Q. Ma, *et al.*, *Nature* **565**, 337 (2019).

[128] K. Kang, T. Li, E. Sohn, J. Shan, K. F. Mak, *Nat. Mater.* **18**, 324 (2019).

[129] I. Sodemann, L. Fu, *Phys. Rev. Lett.* **115**, 216806 (2015).

[130] A. L. Sharpe, *et al.*, *Science* **365**, 605 (2019).

[131] A. L. Sharpe, *et al.*, *arXiv:2102.04039* .

[132] X. Lu, *et al.*, *Nature* **574**, 653 (2019).

[133] W.-Y. He, D. Goldhaber-Gordon, K. T. Law, *Nat. Commun.* **11**, 1650 (2020).

[134] W.-Y. He, K. T. Law, *arXiv:2012.09896* .

[135] C.-P. Zhang, *et al.*, *arXiv:2010.08333* .

[136] S.-Y. Li, *et al.*, *Phys. Rev. B* **102**, 121406 (2020).

[137] C. Huang, N. Wei, A. H. MacDonald, *Phys. Rev. Lett.* **126**, 056801 (2021).

[138] Y. Su, S. Z. Lin, *Phys. Rev. Lett.* **125**, 226401 (2020).

[139] A. B. Kuzmenko, I. Crassee, D. van der Marel, P. Blake, K. S. Novoselov, *Phys. Rev. B* **80**, 165406 (2009).

[140] N. M. R. Peres, F. Guinea, A. H. Castro Neto, *Phys. Rev. B* **73**, 125411 (2006).

[141] J. Jung, A. H. MacDonald, *Phys. Rev. B* **89**, 035405 (2014).

[142] F. Joucken, *et al.*, *Phys. Rev. B* **101**, 161103 (2020).

[143] T. M. G. Mohiuddin, *et al.*, *Phys. Rev. B* **79**, 205433 (2009).

[144] E. Mariani, A. J. Pearce, F. von Oppen, *Phys. Rev. B* **86**, 165448 (2012).

[145] M. Mucha-Kruczyński, E. McCann, V. I. Fal'ko, *Semicond. Sci. Technol.* **25**, 033001 (2010).

[146] J. C. Slonczewski, P. R. Weiss, *Phys. Rev.* **109**, 272 (1958).

[147] J. W. McClure, *Phys. Rev.* **108**, 612 (1957).

[148] V. M. Pereira, A. H. Castro Neto, N. M. R. Peres, *Phys. Rev. B* **80**, 045401 (2009).

[149] G. G. Naumis, S. Barraza-Lopez, M. Oliva-Leyva, H. Terrones, *Rep. Prog. Phys.* **80**, 096501 (2017).

[150] M. Ramezani Masir, D. Moldovan, F. Peeters, *Solid State Commun.* **175-176**, 76 (2013).

[151] D. Xiao, J. Shi, Q. Niu, *Phys. Rev. Lett.* **95**, 137204 (2005).

[152] T. Thonhauser, D. Ceresoli, D. Vanderbilt, R. Resta, *Phys. Rev. Lett.* **95**, 137205 (2005).

[153] J. Shi, G. Vignale, D. Xiao, Q. Niu, *Phys. Rev. Lett.* **99**, 197202 (2007).

[154] N. Ashcroft, D. Mermin, *Solid State Physics* (Saunders College Publishing, Fort Worth, 1976).

[155] Y. Nam, D.-K. Ki, D. Soler-Delgado, A. F. Morpurgo, *Nat. Phys.* **13**, 1207 (2017).

[156] S. A. Hartnoll, *Nat. Phys.* **11**, 54 (2015).

[157] A. Varlet, *et al.*, *Phys. Rev. Lett.* **113**, 116602 (2014).

[158] K. S. Novoselov, *et al.*, *Science* **306**, 666 (2004).

[159] E. Pop, V. Varshney, A. K. Roy, *MRS Bull.* **37**, 1273 (2012).

[160] S. Bhowal, S. Satpathy, *Phys. Rev. B* **102**, 201403 (2020).

[161] L. Wang, *et al.*, *Nano Lett.* **19**, 4097 (2019).

[162] L. Wang, *et al.*, *Phys. Rev. Lett.* **124**, 157701 (2020).

[163] L. Wang, *et al.*, *arXiv:2009.03035* .

[164] E. M. Spanton, *et al.*, *arXiv:1512.03373* .

[165] V. Sunko, *et al.*, *npj Quantum Mater.* **4**, 46 (2019).

[166] D. M. Basko, S. Piscanec, A. C. Ferrari, *Phys. Rev. B* **80**, 165413 (2009).

[167] M. Huang, *et al.*, *Proc. Natl. Acad. Sci.* **106**, 7304 (2009).

[168] Y. Cho, *et al.*, *Carbon N. Y.* **103**, 473 (2016).

[169] C. Androulidakis, *et al.*, *Phys. Rev. B* **97**, 241414 (2018).

[170] D. Yoon, Y.-W. Son, H. Cheong, *Phys. Rev. Lett.* **106**, 155502 (2011).

[171] M. Huang, H. Yan, T. F. Heinz, J. Hone, *Nano Lett.* **10**, 4074 (2010).

[172] Y. You, Z. Ni, T. Yu, Z. Shen, *Appl. Phys. Lett.* **93**, 163112 (2008).

[173] M. Goldsche, *et al.*, *Nano Lett.* **18**, 1707 (2018).

[174] G. Tsoukleri, J. Parthenios, C. Galiotis, K. Papagelis, *2D Mater.* **2**, 024009 (2015).

[175] R. Ribeiro-Palau, *et al.*, *Science* **361**, 690 (2018).

[176] Y. Yang, *et al.*, *Sci. Adv.* **6**, eabd3655 (2020).

[177] C. Lee, *et al.*, *Science* **328**, 76 (2010).

[178] D. L. Olynick, B. Cord, A. Schipotinin, D. F. Ogletree, P. J. Schuck, *J. Vac. Sci. Technol. B* **28**, 581 (2010).

[179] P. Li, D. Collomb, S. Bending, *Mater. Lett.* **257**, 126765 (2019).

[180] B. Özyilmaz, P. Jarillo-Herrero, D. Efetov, P. Kim, *Appl. Phys. Lett.* **91**, 192107 (2007).

[181] A. L. Kitt, *et al.*, *Nano Lett.* **13**, 2605 (2013).

[182] Z. Peng, X. Chen, Y. Fan, D. J. Srolovitz, D. Lei, *Light Sci. Appl.* **9**, 190 (2020).

[183] J. Son, *et al.*, *Nat. Commun.* **9**, 3988 (2018).

[184] J. Son, *et al.*, *Nano Lett.* **21**, 891 (2021).

[185] A. van der Zande, personal communication (2020).

[186] I. Zailer, J. E. Frost, V. Chabasseur-Molyneux, C. J. Ford, M. Pepper, *Semicond. Sci. Technol.* **11**, 1235 (1996).

[187] J. D. Sanchez-Yamagishi, *et al.*, *Nat. Nanotechnol.* **12**, 118 (2017).

[188] G. L. Yu, *et al.*, *Proc. Natl. Acad. Sci.* **110**, 3282 (2013).

[189] J. Xia, F. Chen, J. Li, N. Tao, *Nat. Nanotechnol.* **4**, 505 (2009).

[190] B. Terrés, *et al.*, *Nat. Commun.* **7**, 11528 (2016).

[191] V. E. Dorgan, M.-H. H. Bae, E. Pop, *Appl. Phys. Lett.* **97**, 8 (2010).

[192] D. C. Ralph, Berry curvature, semiclassical electron dynamics, and topological materials: Lecture notes for Introduction to Solid State Physics (2020).

[193] Farhan Rana, Dynamics of Electrons in Energy Bands from Gauge Invariance Berry's Phase and Berry's Curvature, Lecture notes (2009).

[194] A. Knothe, V. Fal'ko, *Phys. Rev. B* **98**, 155435 (2018).

[195] C.-S. Park, *Phys. Lett. A* **382**, 121 (2018).

[196] Y. Zhang, *et al.*, *Phys. Rev. B* **102**, 081403 (2020).